POLITECNICO DI TORINO

DEPARTMENT OF ELECTRONICS AND TELECOMMUNICATIONS (DET)

Master's Degree in Electronic Engineering

Master's Degree Thesis

Hybrid laser design for a silicon photonics platform

Supervisor
Prof.ssa Mariangela Gioannini

Candidate
Antonino Bologna

December, 2019

To my mother and father, thank you for believing in me.

Summary

Silicon photonics is a new technology that allows to create photonic devices that use silicon as an optical medium, with the final goal of integrating photonic and electronic devices on the same silicon chip. Although various passive optical devices have been successfully demonstrated in the context of silicon photonics, the most important building block of an optical system, an efficient laser source, monolithically integrated on Si, is still missing. This is due to the fact that silicon is an indirect band-gap material and thus spontaneous and stimulated emission of light is extraordinarily difficult to obtain. Nowadays, several technological solutions are available to overcome this problem.

An overview of the state-of-the-art of the available techniques for laser integration on silicon is presented. Approaches such as hybrid integration, heterogeneous integration through wafer bonding and direct hetero-epitaxial growth on silicon are investigated, highlighting advantages and disadvantages for all of these techniques. Also, the most important features of two matures platforms for photonic integration, i.e. silicon-on-insulator (SOI) and SiN-on-silica, are discussed and compared.

Subsequently, after a brief theoretical review of microring resonators and of the Vernier effect, two hybrid laser architectures, *Laser 1* and *Laser 2*, are introduced. They are based on edge-coupling between a III-V Reflective Semiconductor Optical Amplifier (RSOA) and an external photonic integrated circuit (PIC), designed as the front mirror of the laser cavity. Furthermore, the design method and the main figures of merits of these devices, are discussed.

Results related to the comparison between the two hybrid laser architectures, implemented on a SiN platform, for the designs that 1) maximize the wall-plug-efficiency WPE and 2) minimize the linewidth $\Delta\nu$, reveal that *Laser 2* performs better than *Laser 1*.

Much of this work is devoted to the modelling of nonlinear effects (TPA and FCA) in silicon rings and to understanding the impact of these nonlinearities on the performances of the devices. First of all, nonlinearities are introduced in microring resonators, then in straight waveguides and finally an overall model of the entire PIC is built in such a way that it is possible to compute the optical field effective reflectivity at the SOA AR facet.

Results related to the designs that 1) maximize the WPE and 2) minimize the linewidth $\Delta\nu$, for the hybrid laser architecture *Laser 2*, implemented on a Si platform with two different types of SOA, low gain and high gain SOA, both in the linear and nonlinear case, show that the impact of nonlinear effects on the performances is more evident for the design that minimizes the linewidth.

Finally, a performance comparison between the lasers implemented on both platforms is presented. Results show that the hybrid laser architecture *Laser 2*, implemented using high gain SOA on a Si platform, performs better in terms of maximum WPE, while *Laser 2* implemented on a SiN platform performs better in terms of minimum linewidth.

Acknowledgements

First of all, I would like to express my deep and sincere gratitude to my supervisor, Prof.ssa Mariangela Gioannini, for her assistance, guidance and patience throughout the entire process of writing this thesis. She has taught me the methodology and discipline to carry out a project and her motivation and dynamism have deeply inspired me. Thank you so much, I will never forget it!

I am extremely grateful to my family, whose love, support and guidance are with me in whatever I pursue. Thanks to my parents, Salvatore and Pasqua, for giving me the opportunities and experiences that have made me who I am. Thanks to my brother Vincenzo for always encouraging me and thanks to my brother Daniel: most of the drawings in Chapter 4 are his work.

A big thanks goes also to my aunt Maria Rita, to my uncle Orazio and to my cousins Nino, Aurora and Francesco: my second family is what you are to me! A heartfelt thanks to my grandmother Serafina, for always believing in me, always encouraging me and always loving me.

A special thanks goes to my dear friend Gianni, a.k.a. Trouble-Man, for his humor and sarcasm that have made this experience considerably more joinable.

I would also like to thank my two unbiological brothers, Andrea and Alessio, for being the friends I have always wanted to have: Cepboys forever!

I am grateful to my dear friend Marco for welcoming me in Turin and for being a great roommate: I will never forget your ice cream problems.

True friendship is not being inseparable, it is being separated and nothing changes:

thanks to Riccardo for his sincere friendship, you are like a brother to me!
Thanks to Vincenzo for our senseless 20 €bets and to Luigi and Francesco for showing me the art of the good life.
Thanks to the group "Politecnicamente scarichi", in particular to Alessandro and Edoardo and thanks to my two strange rommmates Alessio and Simone.
Finally, I thank myself for never giving up and for always aiming high.

Contents

List of Tables

List of Figures

Chapter 1

Silicon Photonics and the state-of-the-art of laser integration on silicon

1.1 An introduction to Silicon Photonics

For decades, copper has been the most used material in the electronics industry for the realization of electrical interconnects. However, nowadays, it is reaching its peak performance. Even if transistor scaling improves the performance of Integrated Circuits (ICs), the same can not be said for the downsizing of interconnects. In fact, when the dimensions of a wire are scaled, its resistance and capacitance grow, decreasing the bandwidth and increasing its resistance-capacitance (RC) delay and power consumption. For example, Figure 1.1 shows that, in modern microprocessors, over half of the dissipated power is dissipated by the interconnects [**1**].

This is in sharp contrast with the ever-increasing global demand for bandwidth, high data rate transmission and low power consumption in many field of application, such as optical communication systems, data center networks and microprocessor optical interconnects. It becomes clear that a new interconnect technology is needed and optics is believed the right solution to address the aforementioned problems.

The pioneering work carried out by Soref and Bennet [**2**], in mid-1980s, signaled

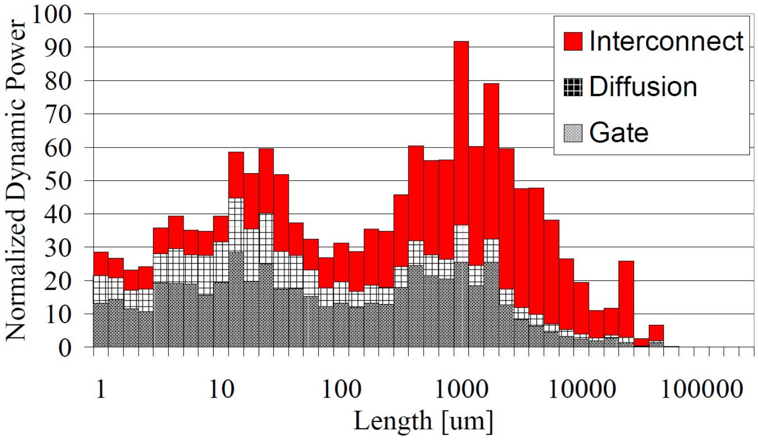

Figure 1.1: Dynamic Power vs. Net Length (image reproduced from [**1**]).

the dawn of silicon photonics. This new technology allows creating photonic devices that use silicon as an optical medium, with the final goal of integrating photonic and electronic devices on the same silicon chip. Several reasons make silicon the material of choice in this context, for example:(1) its transparency at wavelengths greater than 1.1μm makes it suitable for optical communications; (2) mature CMOS fabrication technology can be used to make low cost and mass production optical devices; (3) the large contrast index in silicon-on-insulator (SOI) waveguides, approximately 2.06, gives rise to very strong light confinement and thus enables a reduction in footprint of waveguides that can have bend radii down to 5μm.

To have a clear understanding of what silicon photonics is, Figure 1.2(a) shows a silicon photonic platform in which a dual-core RISC-V processor, a 1 MB SRAM based cache memory and WDM transceiver banks are integrated on the same die. Figure 1.2(b) shows a zoom-in of the optical transceivers while Figure1.2(c) presents the key photonic devices of an optical link implemented in this platform, such as waveguides, microring modulators, photodetectors etc. It is worth noticing that this silicon photonics platform has been called "zero-change" since the native CMOS fabrication steps are not modified. In fact, as shown in Figure 1.3, optical devices are implemented in the region normally used as the transistor body [**3**].

Although various passive optical devices have been successfully demonstrated in the context of silicon photonics , the most important building block of an optical system, i.e. an efficient laser source, monolithically integrated on Si, is still missing. This is due to the fact that silicon is an indirect bandgap material and thus spontaneous and stimulated emission of light is extraoridinarily difficult to obtain. Figure 1.4 [**4**] shows the energy band diagrams of Si (right) and InP (left), that is a direct bandgap material. When an electron makes a transition from the conduction band to the valence band or vice versa, momentum and energy must be conserved, irrespective of the type of the band structure. This condition is easily fulfilled in direct bandgap semiconductors since the minimum energy level of the conduction band and the maximum energy level of the valence band are perfectly aligned with respect to momentum. In indirect bandgap materials this alignment is not present and a third particle, i.e. a phonon, is required to conserve momentum of the whole process. Since three different types of particles are required in this indirect process, i.e. an electron, a photon and a phonon, it proceeds at a much slower rate with respect to the direct process. This simply explains why direct bandgap materials are always preferred for efficient on-chip laser source realization. Figure 1.4(right) also presents two important non-radiative processes: the Auger recombination and free-carrier absorption (FCA).

Nowadays, several technological solutions are available for efficient light source integration on a silicon photonic platform, such as hybrid integration, heterogeneous bonding or epitaxial growth on silicon. Irrespective of the previous technological approaches, the most relevant challenge is the integration of the III-V gain material with the rest of the silicon photonics integrated circuit.

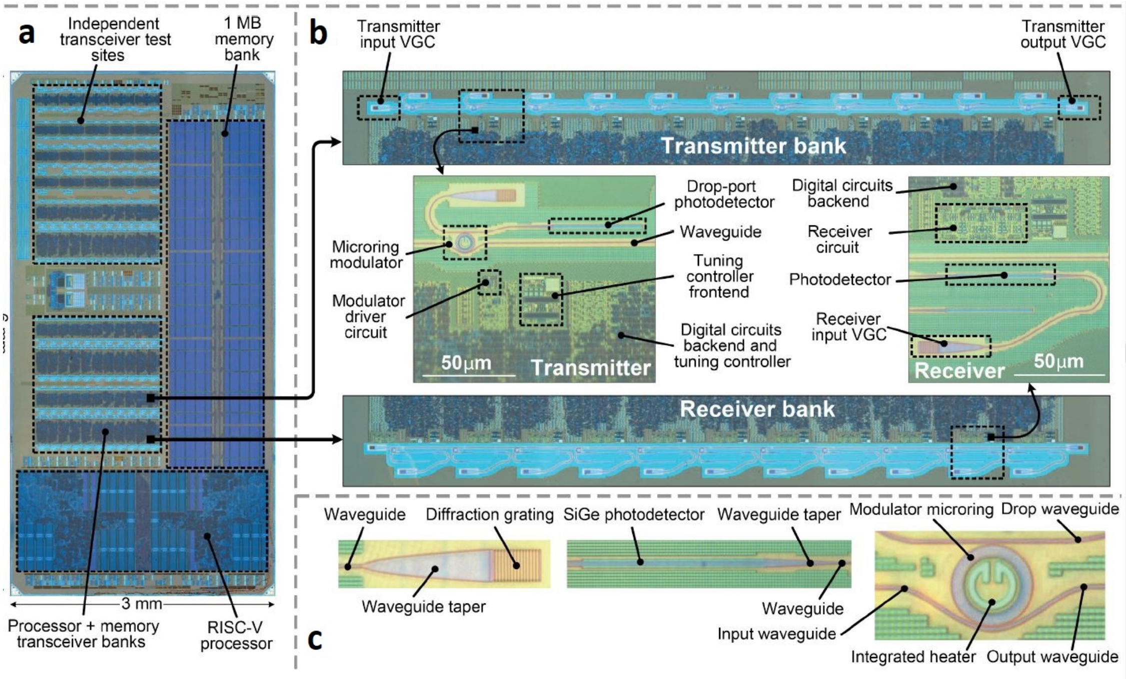

Figure 1.2: (*a*) Die photo, (*b*) WDM transceivers,(*c*) key photonic devices (image reproduced from [**3**]).

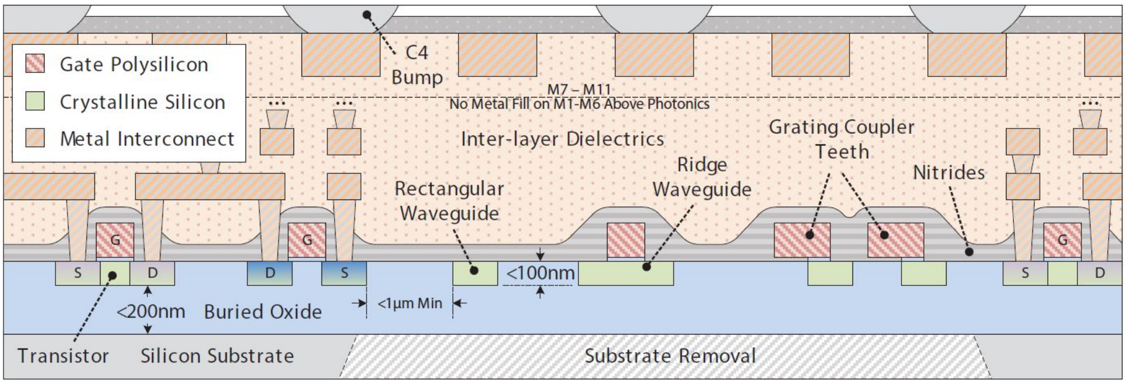

Figure 1.3: SOI CMOS process cross-section with key devices (image reproduced from [**3**]).

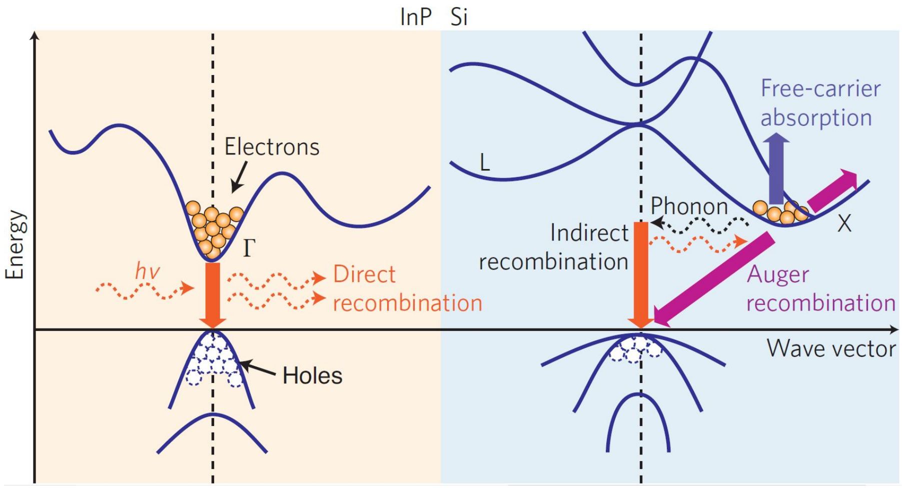

Figure 1.4: Energy band diagrams of a direct bandgap semiconductor (InP, left) and indirect bandgap semiconductor (Si, right); (image reproduced from [**4**]).

1.2 Laser integration on silicon: state-of-the-art

1.2.1 Heterogeneous integration through wafer bonding

The idea behind heterogeneous integration [**5**], [**6**], [**7**] is the bonding, molecular [**8**] or adhesive [**9**], of unpatterned III-V dies or wafers, epitaxial layers facing down, to a pre-processed silicon on insulator wafer, i.e. with optical waveguide circuits (see Figure 1.5 [**10**]). After bonding, the substrate of III-V wafers is removed and III-V material is processed with planar technologies to realize a laser such that light is evanescently coupled to the silicon photonics waveguides. Photolithography guarantees high precision alignment between all the structures, a key advantage compared to hybrid integration. The cavity of the laser can be formed in many different ways, for example by using a ring in the III-V material, as reported in [**11**], or by using a distributed feedback resonator [**12**]. An example of this type of laser, realized through adhesive bonding, is presented in [**13**]: the device shows a threshold current of 30 mA and an output power of more than 4 mW at room temperature. A 3D and cross-sectional views of this device are shown in Figure 1.6. Since III-V dies

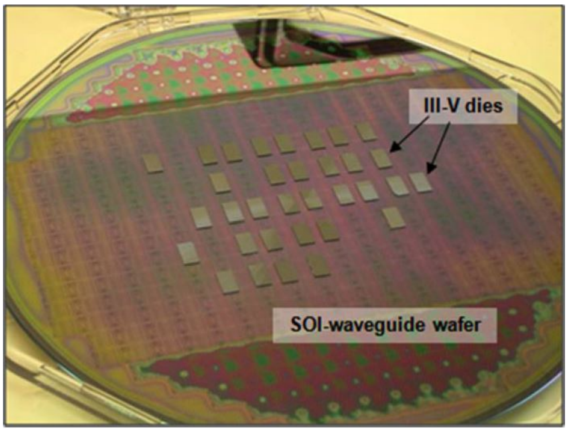

Figure 1.5: III-V dies bonded on a 200 mm SOI-wafer (image reproduced from [**10**]).

are attached only where they are needed, III-V material consumption is very limited. Moreover, the time required to complete the integration process is also limited, since high-precision positioning of III-V dies is not necessary. This approach is particularly well suited for large-scale fabrication of III-V lasers on silicon photonics circuits. However, there are some drawbacks to this technological approach: 1) when adhesive bonding is used, the gain medium is thermally isolated from the substrate; thus, lasers realized with this approach suffer from self-heating that may limits their efficiency for high-temperature operations; 2) reliability problems may arise due to the different values of thermal expansion coefficients of silicon and III-V materials; 3) a proper surface cleaning and smoothing is generally required when molecular bonding is used, to obtain an high-quality III-V on Si interface. This complicates the fabrication process.

1.2.2 Hybrid integration

Hybrid integration is an approach that involves the optical coupling of a discrete, fully-processed laser chip, to external waveguide circuit realized with various passive materials, such as Si, Si_3N_4, SiON, etc., that contains a reflective device. The III-V laser can either be mounted on top of the passive chip [**14**] or next to it [**15**]. For

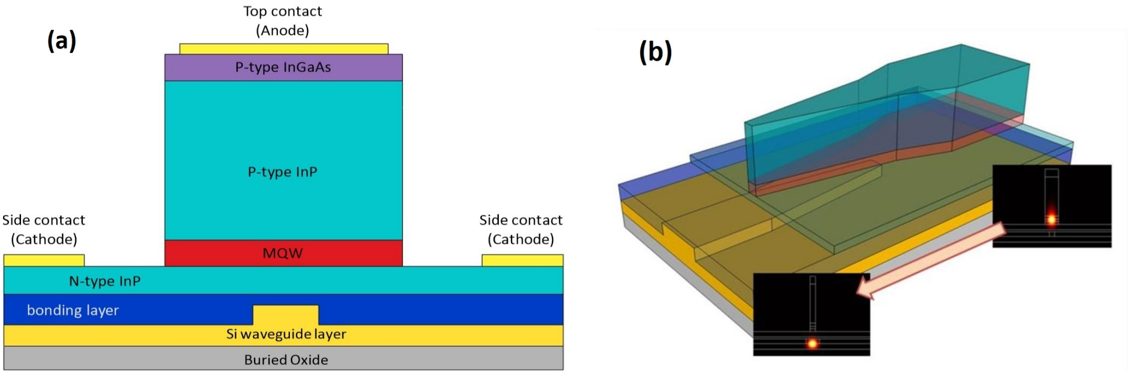

Figure 1.6: Cross-sectional (a) and 3D (b) views of the heterogeneous laser presented in [**13**]

example, Figure 1.7 [**15**] shows a III-V reflective semiconductor optical amplifier (RSOA) edge-coupled to a Si_3N_4 chip to form an external cavity laser between the high-reflection (HR) coated back-facet of the RSOA and the Si_3N_4 based reflector. A clever design of the passive chip is required in order to improve the key metrics of the hybrid laser such as wall plug efficiency (WPE), output power, threshold current, linewidth, side mode suppression ratio (SMSR) etc. For example, as depicted in Figure 1.7, cascaded microring resonators with different radii can be used to realize widely tunable and narrow linewidth hybrid lasers, by exploiting the Vernier effect and the long effective cavity length obtained by the multiple roundtrips in the rings. Due to the large mode mismatch between the waveguides of the active and passive chips, such an approach requires micron-scale alignment to improve the coupling efficiency. Spot size converters (SSC) are often used between the output of the RSOA and the passive chip to relax alignment tolerances. However, since the gain medium and the passive chip are independent, they can be fabricated, optimized and tested independently leading to high performance devices and ensuring high yield: Guan et al. demonstrated in [**16**], a C-band hybrid laser with an optical linewidth of 37 kHz, an output power of 11 mW and a WPE of 4.2%. In [**17**], the authors present an hybrid laser with an output power and a WPE of 20 mW

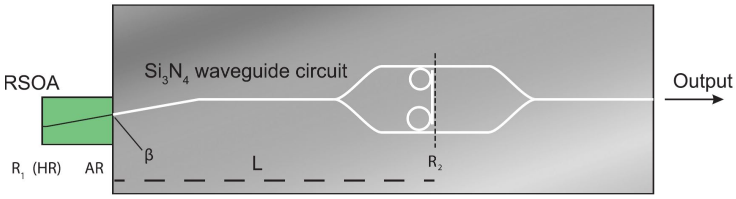

Figure 1.7: Schematic drawing (not to scale) of the hybrid laser reported in [**15**].

and 7.8% respectively; however, the linewidth is 27 MHz. A laser with a linewidth narrower of 15 kHz can be found in the work of Kobayashi et al. [**18**].

1.2.3 Direct hetero-epitaxial growth on silicon

Another approach for fabricating lasers on silicon is based on the direct-epitaxial growth of germanium (Ge) or III-V materials on silicon. Germanium is CMOS compatible and it is considered to be one of the most promising materials for monolithic integration of a light source on silicon. Although Ge is an indirect band-gap material, its band structure can be adequately engineered to achieve efficient light emission. This is demonstrated in [**19**], where a combination of tensile strain and n-type doping is used to turn Ge into a direct band-gap material. In addition to n-type doping and tensile strain, germanium-tin (GeSn) alloys can also be used to modify the band structure of Ge [**20**]. Lasers realized using this technique require 1) low surface roughness of Ge layers to ease the integration process of Ge devices with Si electronics and 2) low threading dislocation density in Ge epitaxial layers to prevent performance degradation eventually caused by the recombination centres introduced along these dislocations [**21**]; moreover, in order to avoid detrimental indirect band-gap behaviour, Si-Ge interdiffusion must be minimized. An electrically pumped Ge-on-Si laser, obtained by employing heavy doping and small biaxial tensile strain ($\sim 0.2\%$), is demonstrated in the work of Camacho-Aguilera et al. in [**22**]. However, the extremely high value of the lasing threshold ($\sim 280kA/cm^2$) renders this device not practical. In order to reduce the threshold, large (>1%)

tensile strain can be employed, as suggested in [**23**].

Aside from germanium, direct band-gap III-V quantum well materials can be heteroepitaxially grown on silicon. Although light emission is much more easy to achieve with these materials, their CMOS compatibility is quite limited. The main problem for this approach is the generation of crystalline defects, including threading and misfit dislocations, caused by the significant lattice constant mismatch, the large difference in thermal and expansion coefficients and the different polarity of the materials. Numerous methods have been proposed to effectively reduce structural defects. These include: 1) the use of a buffer layer between silicon and III-V semiconductors, with an appropriate lattice constant and thermal expansion coefficient [**6**]. Examples of compounds that can be employed as a buffer layer are SiGe, GaAs and GaSb; 2) the epitaxial lateral overgrowth (ELOG) technique [**6**], [**24**]; 3) the use of quantum dots in place of quantum wells [**6**], [**25**], [**26**].

Although epitaxial growth on silicon is regarded as a promising solution for efficient laser source realization, it is still in the research stage and practical applications are far off.

1.3 Platforms for photonic integration

Nowadays, there is a multitude of platforms, realized with different materials (e.g. Si-on-insulator, SiN-on-silica, InP etc.), available for photonic integration, each with their own advantages, disadvantages and trade offs. In this section, the most important features of two mature platforms, i.e. SOI and SiN-on-silica, are presented. Figure 1.8 [**27**] shows a cross-sectional view of both platforms.

1.3.1 Silicon-on-insulator

Silicon-on-insulator refers to a technology where an insulating layer, the so-called buried oxide (BOX), is placed between the silicon substrate and an upper crystalline

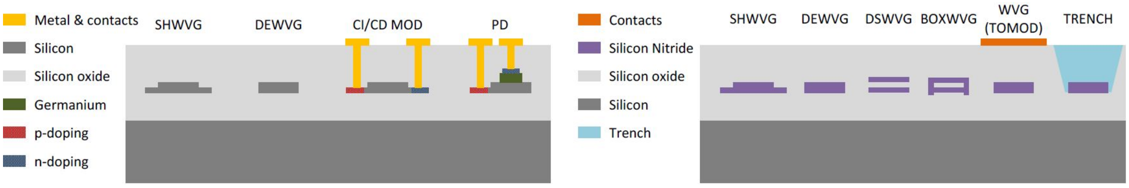

Figure 1.8: Cross-sectrional views of SOI (left) and SiN platforms (right). List of abbreviations: SHWVG Shallow waveguide, DEWVG Deeply etched waveguide, PD Photo-Detector, DSWVG Double-stripe waveguide, BOXWVG Box waveguide, TOMOD Thermo-optic Modulator (image reproduced from [**27**]).

silicon layer, in silicon wafers. Waveguide-based devices are patterned in this silicon top layer using standard CMOS fabrication processes.

The main advantage of SOI platforms is the natural compatibility with CMOS fabrication processes. Silicon waveguides, cladded with silica, have a very high index contrast, approximately equal to 2.06. This leads to strong light confinement, thus enabling a drastic reduction in the footprint of devices: waveguides can have bend radii below 5μm [**28**] . However, the high value of the index contrast also give rise to more scattering losses, due to the unavoidable nm-scale roughness on the vertical sidewalls of the waveguides. Typical propagation losses in silicon waveguides completely sorrounded by silicon dioxide, range from 0.5 dB/cm to 2 dB/cm, largely due to the aforementioned scattering losses [**29**], [**18**]. The strong light confinement in silicon waveguides also results in high power densities, thus enabling nonlinear effects such as two-photon-absorption (TPA) and free-carrier-absorption (FCA). When these effects manifest themselves, extra losses are introduced since the total waveguide loss coefficient is no longer constant but is a function of the light power circulating in the silicon waveguide. It is worth noticing that the BOX should be kept thick enough to optically isolate silicon waveguides from the substrate. This assures the reduction of losses due to the substrate leakage. If this is not possible, then a portion of the substrate can be removed, as depicted in Figure 1.3.

The Pockels effect is normally negligible in silicon and electro-optic modulation is therefore not possible. SOI-based waveguides are typically used for applications requiring wavelenghts in the range from 1.1μm to about 3.7μm. The lower and upper limits are determined by the band edge of silicon, below which silicon is strongly absorbing, and the onset of mid-IR absorption of SiO_2, respectively. Finally, another big advantage of silicon is the value of its thermo-optic coefficient, i.e. the change in refractive index with temperature dn/dT, whose value is $1.87 \cdot 10^{-4} K^{-1}$ at 1550nm, as reported in [**30**]. This value is reasonably large and it allows for efficient thermal tuning of photonic devices like microring resonators.

1.3.2 Silicon nitride

Optical waveguides on SiN-on-silica platforms (hereinafter referred to as SiN platforms) are realized employing a core layer of SiN, typically cladded by SiO_2. Silicon nitride is CMOS-compatible, and in fact it is typically deposited by Low Pressure Chemical Vapour Deposition (LPCVD) or by Plasma Enhanced Chemical Vapour Deposition (PECVD). The index contrast between the core and the cladding is relatively low, approximately equal to 0.55. On one hand, this leads to the reduction of scattering losses, but on the other, the footprint of devices is larger than that on SOI platforms: this represents the most noticeable weakness of SiN platforms.

The main advantage of SiN platforms is that they exhibit very low propagation losses, down to 0.0005 dB/cm, as reported in [**31**]. Since silicon nitride has a wide band gap, SiN-waveguides do not suffer from TPA and FCA. As in the case of silicon, the Pockels effect is normally negligible and thus electro-optic modulation is not possible. SiN has a wider range of transparency than silicon, from 500 nm to 3.7 μm, thus covering most of the visible range.

Finally, the thermo-optic coefficient of SiN, which is found to be $2.51 \cdot 10^{-5} K^{-1}$ [**32**], is significantly lower than that of silicon.

Table 1.1 summarizes the most important differences between the SiN ans SOI platforms.

Table 1.1: Comparison between SiN and SOI platforms.

	Platforms	
	SiN	SOI
Range of transparency	$500nm - 3.7\mu m$	$1.1\mu m - 3.7\mu m$
Refractive index contrast	≈ 0.55	≈ 2.06
CMOS compatibility	Yes	Yes
Typical propagation losses	down to $0.0005dB/cm$	$0.5dB/cm - 2dB/cm$
Nonlinear effects (TPA, FCA,...)	No	Yes
Thermo-optic coefficient (dn/dt)	$2.51 \cdot 10^{-5}K^{-1}$	$1.87 \cdot 10^{-4}K^{-1}$
Minimum bend radius	$95\mu m$	$5\mu m$

1.4 Thesis organization

This thesis is organized as follows. The first part of Chapter 2 presents a theoretical review of ring resonators and of the Vernier effect. The remaining part of the chapter introduces the two hybrid laser architectures, *Laser 1* and *Laser 2*, used in this work, and the design method. Chapter 3 provides the results related to the comparison between the two hybrid laser architectures, implemented on a SiN platform, for the designs that 1) maximize the wall-plug-efficiency WPE and 2) minimize the linewidth $\Delta\nu$. Chapter 4 is devoted to the inclusion of nonlinear effects (TPA and FCA) in silicon waveguides and to the calculation of the optical electric field effective reflectivity of the external mirror at the SOA AR facet. Chapter 5 presents the results related to the designs that 1) maximize the WPE and 2) minimize the linewidth $\Delta\nu$, for the hybrid laser architecture *Laser 2*, implemented on a Si platform, both in the linear and nonlinear case. The results have been obtained using two different types of SOA, SOA 1 and SOA 2. Finally, Chapter 6 gives an overview of the thesis and presents a performance comparison between the lasers implemented on both platforms.

Chapter 2

Linear model for the hybrid laser

2.1 Ring resonators

A ring resonator consists of a looped waveguide where light can circulate either clockwise or counterclockwise. Even if the term ring resonator is used to indicate a looped resonator of any shape, it refers strictly to circular rings. When the shape is not circular, the term racetrack resonator is used. Ring resonators are typically evanescently coupled to one or two straight waveguides, also called bus waveguides, and in fact the two most common configurations are the so-called all-pass filter and add-drop filter, shown in Figure 2.1, where r and k are the self and cross-coupling coefficients, respectively. The cross-coupling coefficient determines the fraction of light that is transferred from the bus waveguide to the ring or vice versa, while the self-coupling coefficient specifies the amount of light inside the bus waveguide or the ring. The all-pass and add-drop configurations can be seen as two-port and four-port structures, respectively, with the name of each port depicted in Figure 2.1. If losses in the coupling section can be neglected, the following relation is satisfied

$$|k|^2 + |r|^2 = 1 \tag{2.1}$$

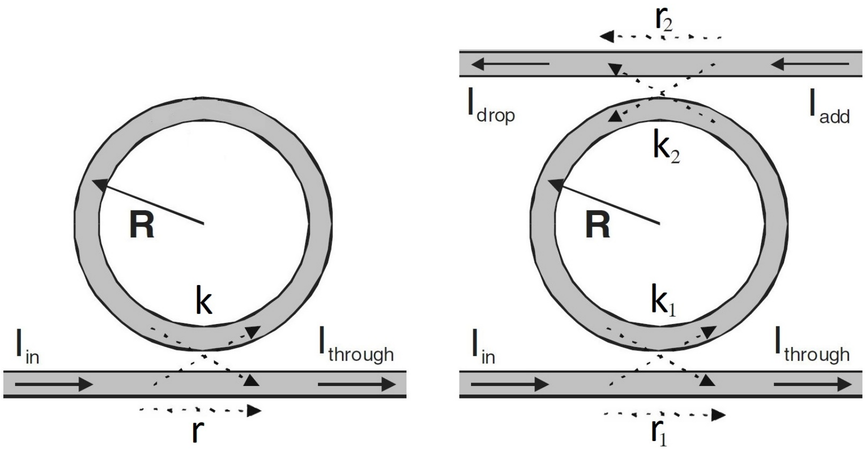

Figure 2.1: All-pass (left) and add-drop (right) configurations (image reproduced from [**33**]).

where $|k|^2$ and $|r|^2$ are the power splitting ratios of the coupler. Irrespective of the configuration, when the round-trip phase shift is an integer multiple of 2π, the ring is said to be on resonance and constructive interference occurs inside the ring, while destructive interference occurs at the through port. As a consequence of that, ring resonators support multiple resonances and the spectral response shows periodic peaks and dips at the drop and the through ports, respectively, as depicted in Figure 2.2. These peaks and dips are located at the resonance wavelengths and the distance between two adjacent peaks is called the free-spectral-range or FSR. The resonance wavelengths are provided by Equation (2.2), where n_{eff} is the effective refractive index, L is the circumference of the ring, defined as L = 2πR, where R is the radius of the ring, and m is an integer number.

$$\lambda_{\text{res}} = \frac{n_{\text{eff}} L}{m}, \qquad m = 1,2,3... \tag{2.2}$$

Therefore, the resonance wavelengths depend on the geometrical characteristics of the ring. Notice that all the formulas reported in this section and in section 2.1.1 come from [**28**] and [**34**]. As regards the all-pass configuration, the ratio between the field at the through port and the input field is given by Equation (2.3)

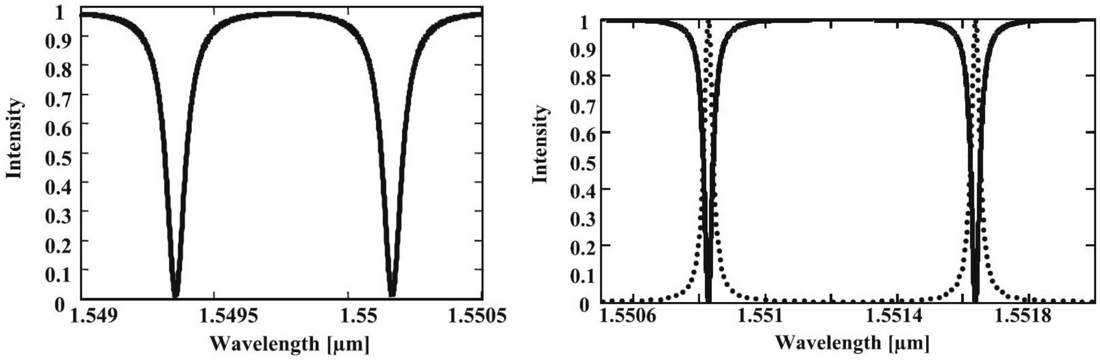

Figure 2.2: Spectral response of the all-pass (left) and add-drop (right) configurations.

$$\frac{E_{\text{through}}}{E_{\text{input}}} = e^{i(\pi+\phi)}\frac{a - re^{-i\phi}}{1 - rae^{i\phi}} \tag{2.3}$$

where ϕ is the phase shift that the field experiences after one round trip and it is defined as the product between the lenght of the ring L and the propagation constant β of the mode circulating in the ring, i.e. $\phi = \beta L$. Moreover, the parameter a is given by Equation (2.4), where α is the linear loss coefficient, whose unit of measurement is cm^{-1}.

$$a^2 = e^{-\alpha L} \tag{2.4}$$

By simply squaring Equation (2.3), one can obtain the intensity transmission, given by the following relation:

$$T_n = \frac{I_{through}}{I_{input}} = \frac{a^2 - 2ra\cos\phi + r^2}{1 - 2ar\cos\phi + (ra)^2} \tag{2.5}$$

Instead, in the case of the add-drop configuration, the intensity transmission to the through and drop ports can be expressed as:

$$T_t = \frac{I_{through}}{I_{input}} = \frac{r_2^2a^2 - 2r_1r_2a\cos\phi + r_1^2}{1 - 2r_1r_2a\cos\phi + (r_1r_2a)^2} \tag{2.6}$$

$$T_d = \frac{I_{drop}}{I_{input}} = \frac{(1 - r_1^2)(1 - r_2^2)a}{1 - 2r_1r_2a\cos\phi + (r_1r_2a)^2} \tag{2.7}$$

Notice that, in previous equations, the frequency dependence is due to the term ϕ, which contains the propagation constant. Equation (2.7) will be extensively used in this thesis, especially during the inclusion of nonlinear effects in silicon ring resonators.

2.1.1 Spectral characteristics

This section contains the definition of the most important spectral parameters of the all-pass and add-drop configurations. They are graphically shown in Figure 2.3. The full width at half maximum (FWHM) of the resonance spectrum for the all-pass configuration is provided by the following equation

$$FWHM = \frac{(1-ra)\lambda_{res}^2}{\pi n_g L\sqrt{ra}} \tag{2.8}$$

while for the add-drop configuration it is defined as

$$FWHM = \frac{(1-r_1r_2a)\lambda_{res}^2}{\pi n_g L\sqrt{r_1r_2a}} \tag{2.9}$$

This parameter indicates the distance between frequencies at which the transmission spectrum reaches half its maximum value. The FSR, written as a function of the wavelength, for both configurations, is defined by the following relation:

$$FSR = \frac{\lambda^2}{n_g L} \tag{2.10}$$

where n_g is the group index, defined as

$$n_g = n_{eff} - \lambda_0 \frac{dn_{eff}}{d\lambda} \tag{2.11}$$

In view of what has been said in Section 1.3.1, the use of silicon ring resonators allows for larger values of FSR with respect to other conventional materials.
Finally, the quality factors Q of the all-pass and add-drop configurations, are provided by Equations (2.12) and (2.13), respectively.

$$Q = \frac{\lambda_{res}}{FWHM} = \frac{\pi n_g L\sqrt{ra}}{\lambda_{res}(1-ra)} \tag{2.12}$$

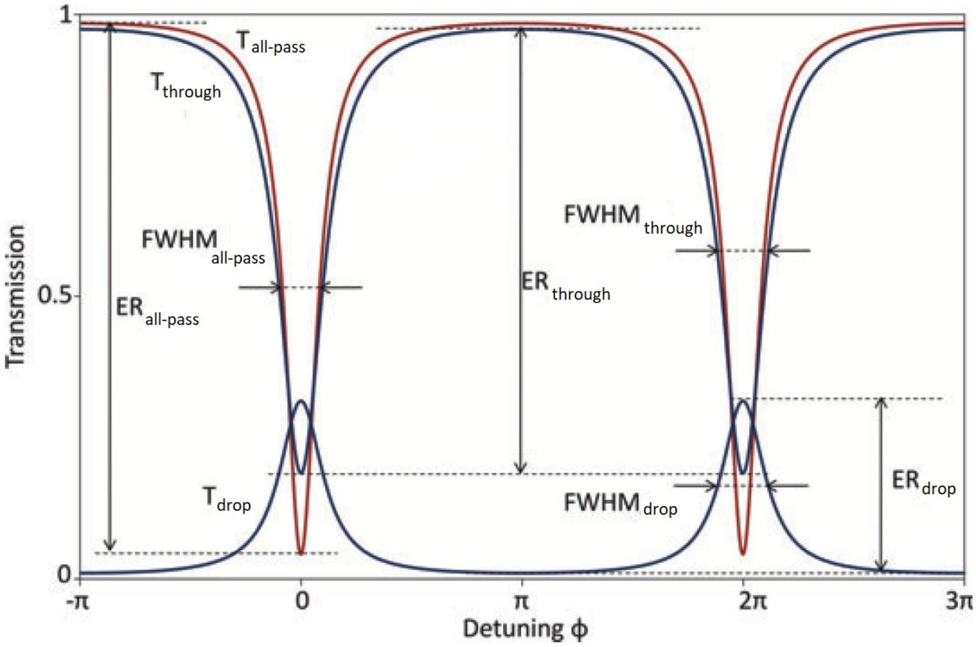

Figure 2.3: Spectral parameters of the all-pass and add-drop configurations (adapted from [**28**]).

$$Q = \frac{\lambda_{res}}{FWHM} = \frac{\pi n_g L \sqrt{r_1 r_2 a}}{\lambda_{res}(1 - r_1 r_2 a)} \tag{2.13}$$

The physical meaning of the Q-factor is related to the ability of a ring resonator to store light energy as long as possible before losing it due to internal losses of the ring waveguide or due to the coupling to the bus waveguides.

2.2 The Vernier effect

Wide-tunability and large values of FSR are commonly obtained by using the Vernier effect. This effect can be efficiently exploited in microring-resonator based lasers, where rings have slightly different circumferences. Figure 2.2 (right) shows the typical transmission curve of a ring resonator in the add-drop configuration. It is clear that, when two or more rings with slightly different radii are used, their

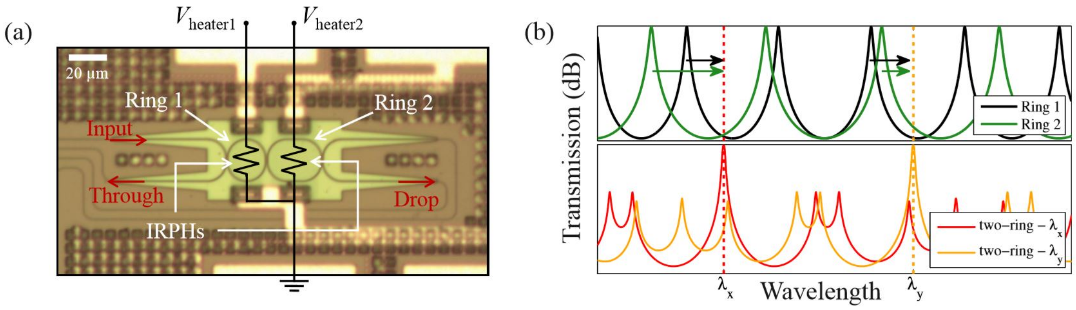

Figure 2.4: (a) A microsope picture representing the two heaters used to perform the thermal tuning; (b) graphical representation of the thermal tuning (image reproduced from [**35**]).

resonances are mostly not aligned, due to the obvious geometrical differences. In fact, as Equation (2.2) suggests, the resonance wavelengths are directly proportional to the radius of a ring resonator. The idea behind the Vernier effect is to align these resonances by using some efficient mechanism. By looking at Equation (2.2), one can easily understand that it is possible to induce a resonance shift by simply varying the effective refractive index. In the context of silicon photonics, two tuning methods are normally used to achieve this goal: carrier based and thermal based. Since carrier injection increases losses due to FCA and carrier depletion has much lower efficiency, thermal tuning is usually the preferred approach, also because this method does not influence optical losses [**36**]. Resonance thermal tuning is usually obtained by using thermal heaters, realized by depositing metal on an insulating layer, like S_iO_2, to avoid proximity of metal and optical mode. It is clear that silicon ring resonators can be thermally tuned in a more efficient way with respect to other materials due to the large value of the thermo-optic coefficient of silicon. Figure 2.4 (a) shows two thermal heaters, here represented as resistors in the circuit, connected to two voltage sources used to perform the thermal tuning. Figure 2.4 (b) shows the alignment of the resonances at either λ_x or λ_y.

The impact of the Vernier effect on the value of the FSR is observable, for example, in Figure 2.5. Here, the FSR of the single ring resonator in (a), FSR_1 is equal to

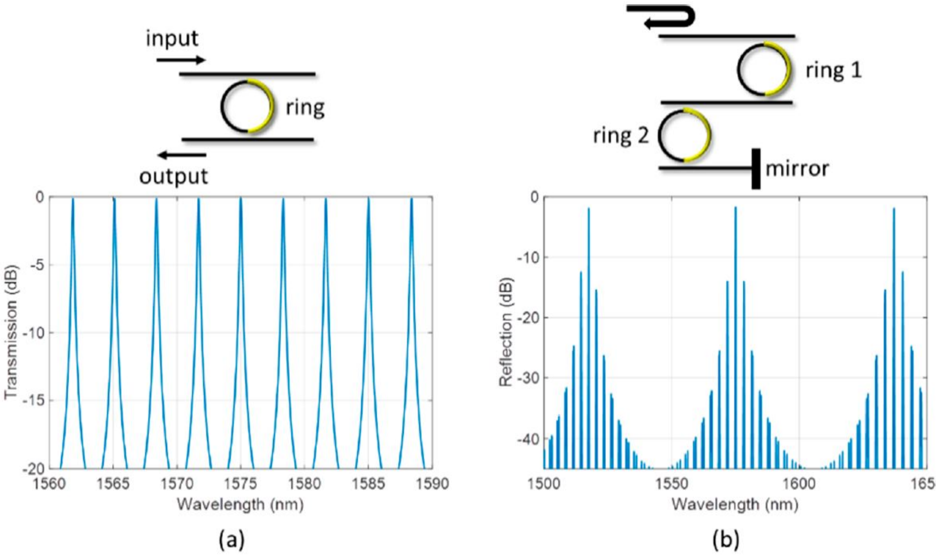

Figure 2.5: (a) add-drop transmission curve of a single resonator with $L_1 = 200\mu m$ and $FSR_1 = 3.31nm$; (b) impact of the Vernier effect that increases the FSR up to $60nm$ ($L_1 = 200\mu m$, $L_2 = 211\mu m$, $M = 18.1$)(image reproduced from [**36**]).

3.31nm. By exploiting the Vernier effect in the scheme with two rings in (b), the new FSR is:

$$FSR_{Vernier} = FSR_1 \cdot M \tag{2.14}$$

where M is the so-called tuning enhancement parameter, defined as

$$M = \frac{L_1}{L_2 - L_1} \tag{2.15}$$

where L_1 and L_2 are the circumferences of the two rings. Since in [**36**] $L_1 = 200\mu m$ and $L_2 = 211\mu m$, the value of $FSR_{Vernier}$ is 60nm, much larger than FSR_1.

2.3 Hybrid laser design method

The work developed in this thesis is based on the hybrid laser designs presented in [**37**]. In particular, the presented hybrid lasers are based on edge-coupling between a commercial Multi Quantum Well (MQW) HR/AR reflective SOA, that provides

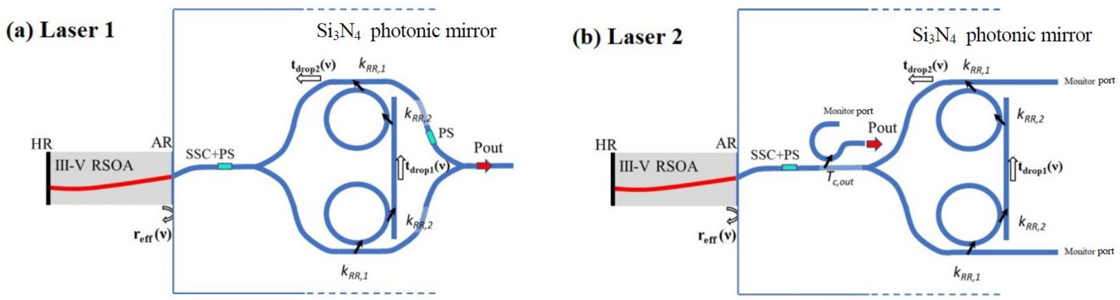

Figure 2.6: Sketch of the two hybrid laser architectures considered in this thesis: *Laser 1* (a) is the configuration in which the output power is collected at the MZI output while *Laser 2* (b) is the architecture where the output power is collected at the output of the coupler (image reproduced from [**37**]).

the III-V gain material, and a passive SiN circuit, designed as the front mirror of the laser cavity. A clever design of the passive chip is required in order to improve the key metrics of the hybrid laser (WPE, $\Delta\nu$, I_{th} etc.). Furthermore, the choice of materials suitable for the realization of the passive chip, for high-performance hybid lasers, is crucial. At this purpose, SiN is particularly promising thanks to its very low linear losses and low nonlinear effects. The two hybrid laser architectures considered in this thesis are shown in Figure 2.6, both implemented on a SiN platform. As one can see, the external mirror is based on a Mach-Zehnder Interferometric (MZI) mirror with two ring resonators, designed to exploit the Vernier effect. In Figure 2.6 (a), the output power is collected at the MZI output, while in (b) it is collected at the output of the coupler added before the MZI splitter. The architecure shown in Figure 2.6 (a) will hereinafter be referred to as *Laser 1*, while the architecture in (b) will be *Laser 2*. As regard *Laser 1*, the parameters used for design optimization are the coupling coefficients of the two rings, $k_{RR,1}$ and $k_{RR,2}$, that must satisfy the relation $k_{RR,1} < k_{RR,2}$ (under-coupled regime) to provide a non null output port transmission coefficient at the resonance frequency. For *Laser 2* the parameters are $k_{RR,1}$ and $k_{RR,2}$ that must satisfy the equation $k_{RR,1} = k_{RR,2}$ (critical coupling regime) in order to have maximum mirror reflection and zero transmission. The other parameter is

Table 2.1: Hybrid laser parameters

SOA parameters	
Facet high reflection (HR) coefficient	$R_{HR} = 0.9$
Internal quantum efficiency	$\eta_i = 0.76$
Length	$L_{SOA} = 1mm$
Active medium volume	$V = 1.5 \cdot 10^{-16} m^3$
Group refractive index	$n_{SOA} = 3.8$
Internal loss	$\alpha_i = 7.6 cm^{-1}$
Carrier lifetime	$\tau_e = 1ns$
Differential gain	$G \cdot \frac{n_{SOA}}{c} = 8.5 \cdot 10^{-17} cm^2$
Spontaneous emission factor	$\beta_{sp} = 10^{-4}$
Radiative efficiency	$\eta_r = 0.8$
Optical confinement factor	$\Gamma_c = 0.032$
SiN mirror parameters	
SSC insertion loss	$2dB$
Waveguide group refractive index	$n_{SiN} = 1.76$
Waveguide loss	$(0 - 1.15)\ cm^{-1}$
Bent waveguide loss	$(0 - 2.30)\ cm^{-1}$
Ring radii	$R_1 = 97\mu m, R_2 = 127\mu m$

the output coupler coefficient $T_{c,out}$. Table 2.1 lists the values of the parameters of the RSOA and the SiN external mirror, used in this thesis. Differently from the work in [**37**], here, the performances of the devices are analyzed as the linear losses of SiN waveguides change. Notice that the transmission drop coefficients of the two rings are tuned in order to have aligned resonances at wavelength $\lambda_0 = 1.31\mu m$. The idea behind the design method is the following: for a fixed value of the output power, $P_{out,target}(= 20mW)$, and linear losses, it is possible to define a 2D design space 1) as $k_{RR,1}$ and $k_{RR,2}$ change, for the case of *Laser 1*, and 2) as $k_{RR,1}$, $k_{RR,2}$ and $T_{c,out}$ change, for the case of *Laser 2*. For each combination of these parameters, it is possible to compute the value of the optical electric field effective reflectivity of the external mirror, $r_{eff}(\nu)$, at the SOA AR facet (see Figure 2.6). Based on the value of $r_{eff}(\nu)$, the most important parameters of the hybrid laser, such as the threshold current I_{th}, the bias current $I_{bias,SOA}$, the effective length $L_{eff,SiN}$, the WPE, the linewidth $\Delta\nu$ and so on, are computed. This process is repeated until all combinations of design parameters are explored. At that point, the idea is simply to select the best design able to 1) maximize the value of WPE or 2) minimize the value of the linewidth $\Delta\nu$. This procedure is repeated for different values of linear losses in such a way that it is possible to plot the behavior of the most important figures of merits of the hybrid laser as a function of linear losses.

2.3.1 Main figures of merits of the hybrid laser

The RSOA bias current, $I_{bias,SOA}$, required to get the target output power, $P_{out,target}$, can be derived by using the standard laser diode rate-equations approach presented in [**38**]. In particular, this current is given by:

$$I_{bias,SOA} = \left[\frac{P_{out,target}}{\eta_i I_{th}} \frac{e}{\hbar\omega_0} \frac{\alpha_i + \alpha_m}{\alpha_m} \frac{(1 - |r_{eff}(\nu_0)|^2) + \sqrt{\frac{|r_{eff}(\nu_0)|^2}{R_{HR}}}(1 - R_{HR})}{|t_{eff,out}(\nu_0)|^2} + 1 \right] I_{th} \tag{2.16}$$

where α_i is the SOA internal modal loss, R_{HR} is the SOA HR facet power reflection coefficient, η_i is the internal quantum efficiency of the SOA, I_{th} is the threshold current, $\hbar\omega_0$ is the recombination energy, e is the charge of an electron, $t_{eff,out}$ is the field transmission coefficient from the AR facet of the SOA and the output port and α_m is the mirror loss, defined as

$$\alpha_m = \frac{1}{L_{SOA}} \log\left(\frac{1}{\sqrt{R_{HR}|r_{eff}(\nu_0)|^2}} \right) \tag{2.17}$$

The threshold current I_{th} is defined as the current when the SOA modal gain equals all the cavity losses, i.e. $\alpha_i + \alpha_m$. Notice that, in this work, the modal gain function is provided by measured gain curves of the SOA under analysis.

The WPE, defined as the ratio between the total optical output power and the input electrical power, is

$$WPE = \frac{P_{out,target}}{I_{bias,SOA} \cdot V_{bias}} \tag{2.18}$$

where V_{bias} is the bias voltage, obtained from measured V-I characteristics of the considered RSOA. The optical linewidth of the hybrid laser is defined as:

$$\Delta\nu = \beta_{sp} v_{SOA} (\alpha_m + \alpha_i) \frac{\eta_r I_{th}}{(I_{bias,SOA} - I_{th})} \frac{1+\alpha_H^2}{4\pi} \left(\frac{n_{SOA} L_{SOA}}{n_{SOA} L_{SOA} + n_{SiN} L_{eff,SiN}} \right)^2 \tag{2.19}$$

where η_r is the radiative efficiency, α_H is the linewidth enhancement factor, β_{sp} is the spontaneous emission factor, n_{SOA} is the group refractive index of the SOA, n_{SiN} is the group refractive index of SiN, v_{SOA} is the SOA group velocity, defined as $v_{SOA} = c/n_{SOA}$, where c is the speed of light, and $L_{eff,SiN}$ is the external mirror effective length, calculated as

$$L_{eff,SiN} = -\frac{v_{g,SiN}}{4\pi} \cdot \frac{\partial \phi_{eff}(\nu_0)}{\partial \nu} \tag{2.20}$$

where $\phi_{eff}(\nu)$ is the phase of $r_{eff}(\nu)$ and $v_{g,SiN}$ is the group velocity in SiN waveguides, defined as $v_{g,SiN} = c/n_{SiN}$.

Chapter 3

Results of the linear model

This chapter presents the results related to the comparison between the two hybrid laser architectures, i.e. *Laser 1* and *Laser 2*, implemented on a SiN platform, for the designs that 1) maximize the wall-plug-efficiency WPE and 2) minimize the linewidth $\Delta\nu$. In particular, Section 3.1 contains the results related to the design for the WPE maximization while Section 3.2 presents the results related to the design for the $\Delta\nu$ minimization. The following results have been obtained using SOA and SiN mirror parameters listed in Table 2.1 when $P_{out,target} = 20mW$. Remember that the design parameters for *Laser 1* are κ_1 and κ_2 while the design parameters for *Laser 2* are $\kappa_1 = \kappa_2$ and $T_{c,out}$.

3.1 Results for WPE maximization

Figure 3.1 shows the behavior of the wall-plug-efficiency, as a function of linear losses, for the two hybrid laser architectures. As one can easily see, the values of WPE of *Laser 2* are higher than those of *Laser 1*, in the entire range of linear losses tested in this work. Figure 3.2 shows instead the behavior of the linewidth $\Delta\nu$, as a function of linear losses, for different values of the linewidth enhancement factor α_H. As can be seen, the values of linewidth obtained using *Laser 2* are lower than those obtained using *Laser 1*, over the entire range of linear losses and for

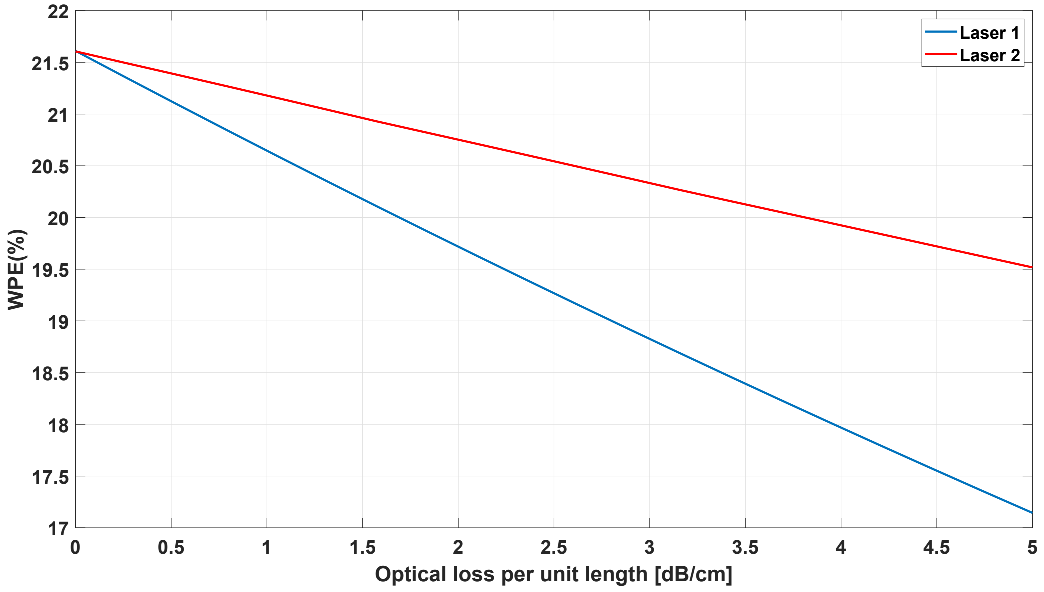

Figure 3.1: Calculated values of WPE for the two hybrid laser architectures, *Laser 1* and *Laser 2*, for the design that maximizes the WPE.

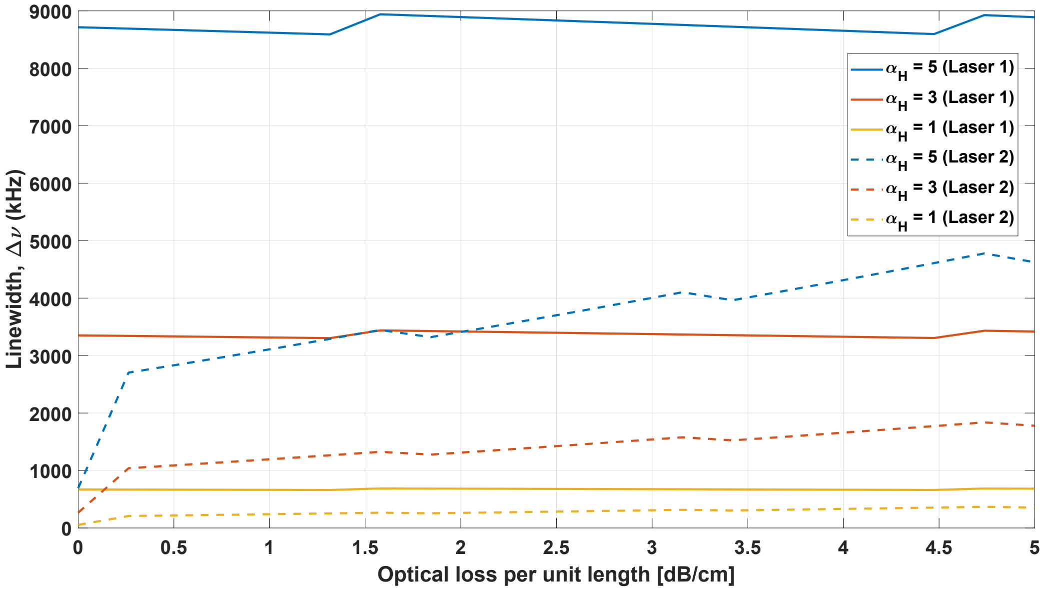

Figure 3.2: Calculated values of $\Delta\nu$ for the two hybrid laser architectures, *Laser 1* and *Laser 2*, for the design that maximizes the WPE.

each value of α_H. Notice that the values of the design parameters for *Laser 1* are $\kappa_1 = 0.05$ and $\kappa_2 \approx 0.938$ while for *Laser 2* we have $\kappa_1 = \kappa_2 \approx 0.19$ and $T_{c,out} \approx 0.9$. Since the range of variation of these parameters was very limited over the entire range of linear losses, we simply extracted a mean value: this explains the use of the approximation symbol. Ultimately, although the values of WPE in Figure 3.1 are quite high, linewidths in Figure 3.2 are not so narrow, irrespective of the type of hybrid laser architecture considered.

3.2 Results for $\Delta\nu$ minimization

Figure 3.3 shows the behavior of the linewidth $\Delta\nu$, as a function of linear losses, for different values of α_H, for the two laser architectures. The values of $\Delta\nu$ obtained using *Laser 2* are lower than those obtained using *Laser 1*, at least for low and intermediate values of linear losses. However, the corresponding values of WPE have been found to be around 3%, for both two architectures. Notice that the values of the design parameters for *Laser 1* are $\kappa_1 \approx 0.08$ and $\kappa_2 \approx 0.12$ while for *Laser 2* we have $\kappa_1 = \kappa_2 \approx 0.038$ and $T_{c,out} \approx 0.13$. Since the range of variation of these parameters was very limited over the entire range of linear losses, we simply extracted a mean value: this explains the use of the approximation symbol. Therefore, even if optical linewidths in Figure 3.3 are much narrower than those in Figure 3.2, the resulting values of WPE are dramatically low.

3.3 Conclusions

In view of the above, it is clear that *Laser 2* performs better than *Laser 1* for each of the two types of design and this is the reason why, hereinafter, the attention will be mainly focused on *Laser 2* for the inclusion of nonlinear effects in silicon waveguides, as will be shown in the next chapter. It is worth noticing that, if the goal is to maximize the WPE, one should keep the value of $T_{c,out}$ as high as possible

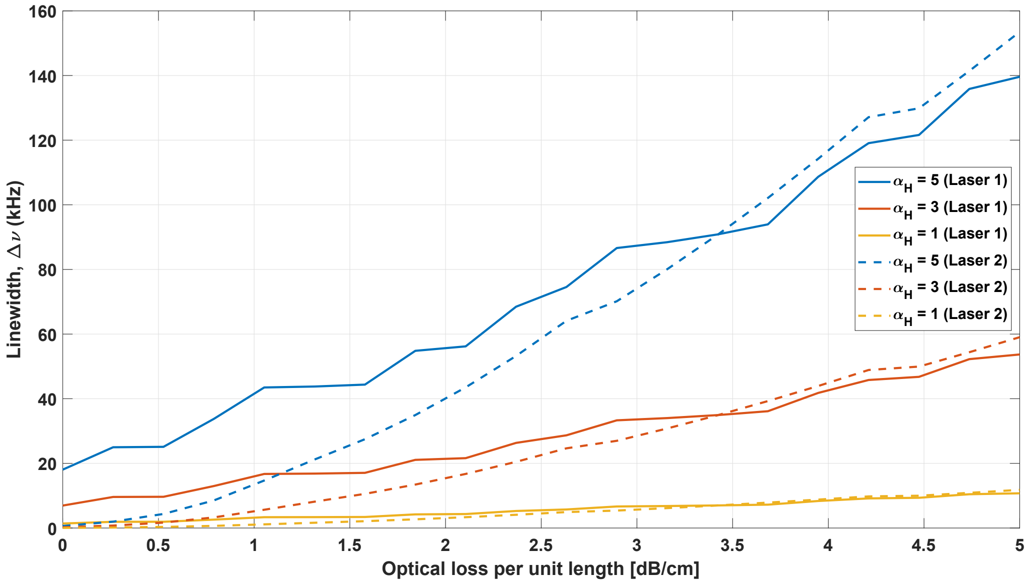

Figure 3.3: Calculated values of $\Delta\nu$ for the two hybrid laser architectures, *Laser 1* and *Laser 2*, for the design that minimizes the linewidth $\Delta\nu$.

in such a way that the output power will be high and, according to Equation (2.18), the corresponding WPE will be high. If the goal is instead to minimize the linewidth $\Delta\nu$, the values of κ_1, κ_2 and $T_{c,out}$ should be kept as low as possible in such a way that the effective length L_{eff} will be high and, as a consequence of that, according to Equation (2.19), the corresponding value of $\Delta\nu$ will be low.

Chapter 4

Nonlinear model of the hybrid laser

4.1 Optical nonlinearities in silicon

Two-photon absorption (TPA) is a nonlinear loss mechanism that occurs when two photons of the same frequency or different frequencies, from an incident field, are absorbed simultaneously, thus leading to the transition of an electron from the valence band to the conduction band. The energy difference between the two states involved in the transition is equal to the sum of the individual photon energies. TPA is typically negligible with respect to linear absorption (α_0), under low light intensities. But when the power propagating inside a waveguide is high enough, TPA becomes predominant over the linear absorption, thus leading to a significant reduction of the number of photons along the waveguide. Notice that these effects are particularly evident in the case of ring resonators due to the high power density inside the rings at the resonance frequency. This is what typically happens in silicon waveguides, due to their high index contrast that gives rise to high power densities. Silicon is strongly affected by TPA at telecommunication wavelengths, i.e. those wavelengths ranging from about 1.2μm to 1.7μm, corresponding to the photon energy range 0.7 eV - 1 eV. Since Si has an indirect band-gap of 1.12 eV, the sum of the energies of two photons is sufficient to promote an electron from the valence

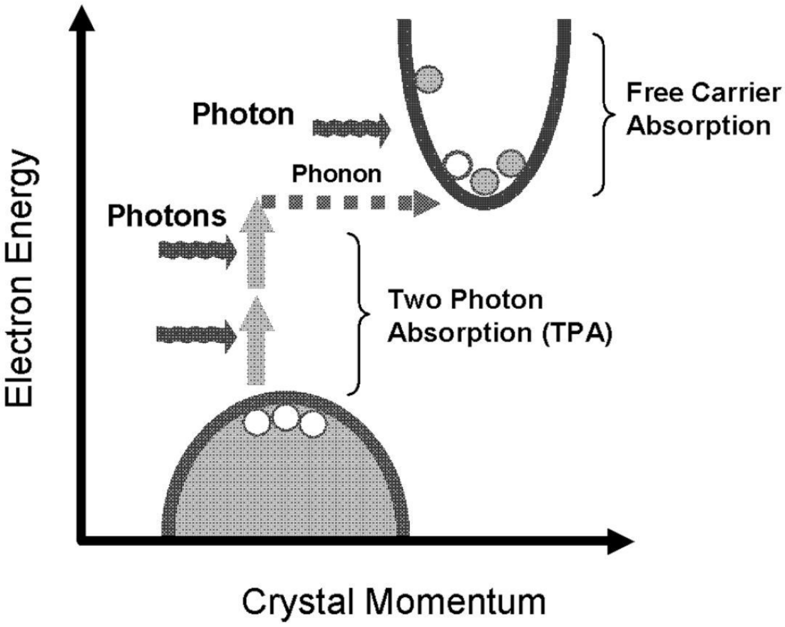

Figure 4.1: Illustration of the phonon-assisted TPA and the consequent FCA in silicon(image reproduced from [**39**]).

band to the conduction band through a phonon assisted transition, as depicted in Figure 4.1. TPA generates free carriers in the conduction band. These carriers can absorb another incident photon, thus making a transition to an higher-energy state in the same band. This intraband phenomenon is called free-carrier absorption, or FCA, and, as one can understand, it increases nonlinear losses even more.

The overall model that takes into account both TPA and FCA, used in this thesis, is defined by the following equations [**40**]:

$$\frac{dP}{dz} = -\alpha_{eff} P \tag{4.1}$$

$$\alpha_{eff} = \alpha_0 + \frac{\beta P}{A_{eff}} + \frac{\tau \beta \sigma P^2}{2h\nu A_{eff}^2} \tag{4.2}$$

Equation (4.1) describes the propagation of the light power P along the silicon waveguide. Here, α_{eff} is the effective loss coefficient defined as in (4.2), where α_0 is the linear loss coefficient, β is the TPA coefficient, A_{eff} is the effective area of the waveguide, σ is the FCA cross section, τ is the free carrier recombination lifetime, h is the Planck constant and ν is the light frequency. Equation (4.2) simply says that, when the power is high enough, the transmission of light through a silicon waveguide becomes dependent on power in a quadratic way. The chosen values of the previous parameters are: $\beta = 6.7 \cdot 10^{-12}\mathrm{m/W}$, $A_{eff} = 0.062 \cdot 10^{-12} m^2$, $\sigma = 1.97 \cdot 10^{-21} m^2$ and $\tau = 10 ns$.

4.2 Inclusion of nonlinearities in ring resonators

In order to include nonlinear effects in ring resonators, the simple structure shown in Figure 4.2 , composed of a ring coupled to two straight waveguides, will be analyzed and the results will be adapted to a more complex structure. In Figure 4.2, a_{cw} and a_{ccw} are the amplitudes of the clockwise and counterclockwise modes circulating in the ring at the resonance frequency ω_0. Notice that the quantities $|a_{cw}|^2$ and $|a_{ccw}|^2$ correspond to the energies of the two modes. Parameters denoted by the letter S are the amplitudes of the modes propagating in the two straight waveguides. Notice that the quantity $|S|^2$ corresponds to the power of that particular mode. The equations that describe the structure in Figure 4.2, taken from [**41**], are:

$$\frac{da_{cw}}{dt} = \left(j\omega_0 - \frac{1}{\tau_0} - \frac{1}{\tau_{ca}} - \frac{1}{\tau_{cb}} \right) a_{cw} + j\mu a_{ccw} + \kappa_b S_{b1}^{+} + \kappa_a S_{a2}^{+} \tag{4.3}$$

$$\frac{da_{ccw}}{dt} = \left(j\omega_0 - \frac{1}{\tau_0} - \frac{1}{\tau_{ca}} - \frac{1}{\tau_{cb}} \right) a_{ccw} + j\mu^* a_{cw} + \kappa_a S_{a1}^{+} + \kappa_b S_{b2}^{+} \tag{4.4}$$

$$S_{a1}^{-} = S_{a2}^{+} - \kappa_a^* a_{cw} \tag{4.5}$$

$$S_{a2}^{-} = S_{a1}^{+} - \kappa_a^* a_{ccw} \tag{4.6}$$

$$S_{b1}^{-} = S_{b2}^{+} - \kappa_b^* a_{ccw} \tag{4.7}$$

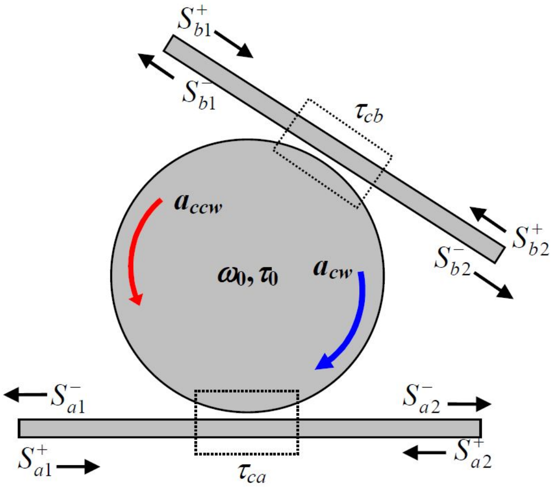

Figure 4.2: Schematic of the ring resonator coupled to two straight waveguides; rectangles with dashed boarders indicate the two coupling regions with coupling time constants τ_{ca} and τ_{cb} (image reproduced from [**41**]).

$$S_{b2}^{-} = S_{b1}^{+} - \kappa_b^* a_{cw} \tag{4.8}$$

$$|\kappa_a| = \sqrt{\frac{2}{\tau_{ca}}} \tag{4.9}$$

$$|\kappa_b| = \sqrt{\frac{2}{\tau_{cb}}} \tag{4.10}$$

where κ_a and κ_b are the coupling coefficients between the two straight waveguides and the ring, while τ_{ca} and τ_{cb} are the coupling time constants. The symbol '*' in previous equations indicates the complex conjugate. In what follows, S_{a2}^{+} and S_{b2}^{+} are set to zero since they are not needed in the situation of interest; moreover, the coupling between the clockwise and counterclockwise modes is considered to be negligible. This latter assumption assures that the quantities $j\mu a_{ccw}$ and $j\mu^* a_{cw}$ can be neglected. The Fourier transforms of (4.3) and (4.4) are given by Equations (4.11) and (4.12)

$$j\omega a_{cw} = \left(j\omega_0 - \frac{1}{\tau_0} - \frac{1}{\tau_{ca}} - \frac{1}{\tau_{cb}}\right) a_{cw} + \kappa_b S_{b1}^{+} \tag{4.11}$$

$$j\omega a_{ccw} = \left(j\omega_0 - \frac{1}{\tau_0} - \frac{1}{\tau_{ca}} - \frac{1}{\tau_{cb}}\right) a_{ccw} + \kappa_a S_{a1}^{+} \tag{4.12}$$

from which it is possible to find the values of a_{cw} and a_{ccw}, as shown in Equations (4.13) and (4.14).

$$a_{cw} = \frac{\kappa_b S_{b1}^{+}}{j(\omega - \omega_0) + \dfrac{1}{\tau_0} + \dfrac{1}{\tau_{ca}} + \dfrac{1}{\tau_{cb}}} \tag{4.13}$$

$$a_{ccw} = \frac{\kappa_a S_{a1}^{+}}{j(\omega - \omega_0) + \dfrac{1}{\tau_0} + \dfrac{1}{\tau_{ca}} + \dfrac{1}{\tau_{cb}}} \tag{4.14}$$

At the resonance frequency, i.e. when ω=ω_0, (4.13) and (4.14) can be rewritten as

$$a_{cw} = \frac{\kappa_b S_{b1}^{+}}{\dfrac{1}{\tau_0} + \dfrac{1}{\tau_{ca}} + \dfrac{1}{\tau_{cb}}} \tag{4.15}$$

$$a_{ccw} = \frac{\kappa_a S_{a1}^{+}}{\dfrac{1}{\tau_0} + \dfrac{1}{\tau_{ca}} + \dfrac{1}{\tau_{cb}}} \tag{4.16}$$

By inverting (4.9) and (4.10), it is possible to write the following relations:

$$\frac{1}{\tau_{ca}} = \frac{|\kappa_a|^2}{2} = \frac{\kappa_a \kappa_a^*}{2} \tag{4.17}$$

$$\frac{1}{\tau_{cb}} = \frac{|\kappa_b|^2}{2} = \frac{\kappa_b \kappa_b^*}{2} \tag{4.18}$$

Moreover, τ_0 and the intrinsic quality factor of the resonator Q_0 are related through Equation (4.19).

$$\frac{1}{\tau_0} = \frac{\omega_0}{2Q_0} \tag{4.19}$$

By substituting (4.17), (4.18) and (4.19) in (4.15) and (4.16), a_{cw} and a_{ccw} can now be expressed as

$$a_{cw} = \frac{2\kappa_b S_{b1}^{+}}{\dfrac{\omega_0}{Q_0} + \kappa_a \kappa_a^* + \kappa_b \kappa_b^*} \tag{4.20}$$

$$a_{ccw} = \frac{2\kappa_a S_{a1}^+}{\dfrac{\omega_0}{Q_0} + \kappa_a\kappa_a^* + \kappa_b\kappa_b^*} \tag{4.21}$$

The power circulating in the resonator is related to the total resonator energy by the following formula:

$$P_c = \frac{v_g(|a_{cw}|^2 + |a_{ccw}|^2)}{L} \tag{4.22}$$

where v_g is the group velocity of the traveling modes inside the ring, and L is the cirumference of the ring. The energies $|a_{cw}|^2$ and $|a_{ccw}|^2$ can be written as follows

$$\begin{aligned} |a_{cw}|^2 = a_{cw}a_{cw}^* &= \frac{2\kappa_b S_{b1}^+}{\left(\dfrac{\omega_0}{Q_0} + \kappa_a\kappa_a^* + \kappa_b\kappa_b^*\right)} \cdot \frac{2\kappa_b^* S_{b1}^{+*}}{\left(\dfrac{\omega_0}{Q_0} + \kappa_a^*\kappa_a + \kappa_b^*\kappa_b\right)} = \\ &= \frac{4|\kappa_b|^2 P_b}{\left(\dfrac{\omega_0}{Q_0} + |\kappa_a|^2 + |\kappa_b|^2\right)^2} \end{aligned} \tag{4.23}$$

$$\begin{aligned} |a_{ccw}|^2 = a_{ccw}a_{ccw}^* &= \frac{2\kappa_a S_{a1}^+}{\left(\dfrac{\omega_0}{Q_0} + \kappa_a\kappa_a^* + \kappa_b\kappa_b^*\right)} \frac{2\kappa_a^* S_{a1}^{+*}}{\left(\dfrac{\omega_0}{Q_0} + \kappa_a^*\kappa_a + \kappa_b^*\kappa_b\right)} = \\ &= \frac{4|\kappa_a|^2 P_a}{\left(\dfrac{\omega_0}{Q_0} + |\kappa_a|^2 + |\kappa_b|^2\right)^2} \end{aligned} \tag{4.24}$$

where $P_a = S_{a1}^+ S_{a1}^{+*}$ and $P_b = S_{b1}^+ S_{b1}^{+*}$. So,

$$P_c = \frac{v_g\,(4|\kappa_a|^2 P_a + 4|\kappa_b|^2 P_b)}{L\left(\dfrac{\omega_0}{Q_0} + |\kappa_a|^2 + |\kappa_b|^2\right)^2} \tag{4.25}$$

This result can be extended to the structure depicted in Figure 4.3, where each ring resonator is coupled to two bus waveguides. Notice that the radii of the two rings, R1 and R2, are slightly different. By using Equation (4.25), it is possible to write

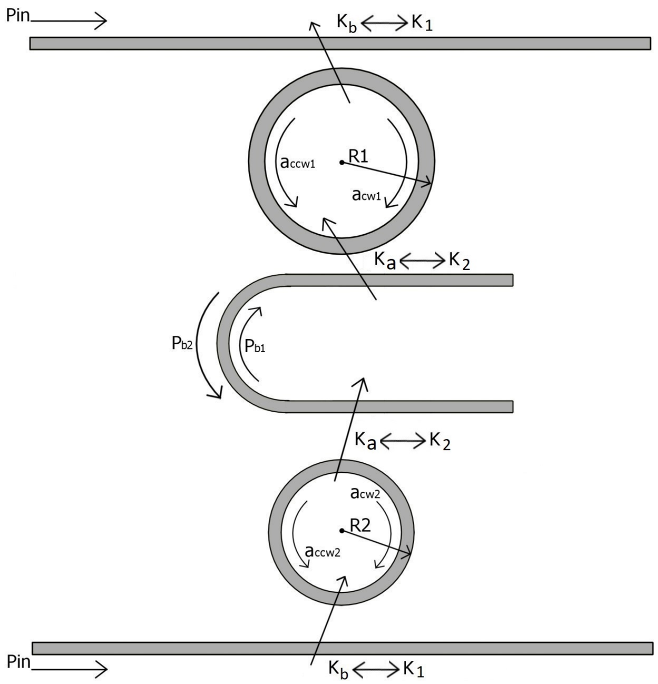

Figure 4.3: Schematic of the two ring resonators with radii R1 and R2; P_{b1} is the power going into ring 1 coming from ring 2 while P_{b2} is the power going into ring 2 coming from ring 1.

the power circulating inside the resonator 1 as follows

$$P_{c1} = \frac{v_g\left(4|\kappa_a|^2 P_{b1} + 4|\kappa_b|^2 P_{in}\right)}{L_1\left(\dfrac{\omega_0}{Q_0} + |\kappa_a|^2 + |\kappa_b|^2\right)^2} \tag{4.26}$$

Coupling coefficients κ_a and κ_b have their own measurement unit, as can be seen from Equations (4.9) and (4.10). However, coupling coefficients κ_1 and κ_2 in our model are dimensionless number because they are the field coupling coefficients from the bus waveguide to the ring and vicevera. So, it is necessary to rewrite κ_a and κ_b as follows

$$|\kappa_a|^2 = \frac{|\kappa_2|^2 v_g}{L} \tag{4.27}$$

$$|\kappa_b|^2 = \frac{|\kappa_1|^2 v_g}{L} \tag{4.28}$$

By substituting Equations (4.27) and (4.28) in (4.26), the circulating power is now given by the following equation:

$$P_{c1} = \frac{v_g^2\left(4|\kappa_2|^2 P_{b1} + 4|\kappa_1|^2 P_{in}\right)}{L_1^2\left(\frac{\omega_0}{Q_0} + \frac{|\kappa_2|^2 v_g}{L_1} + \frac{|\kappa_1|^2 v_g}{L_1}\right)^2} \tag{4.29}$$

The ratio $\frac{\omega_0}{Q_0}$ can be rewritten by using the following formula:

$$Q_0 = \frac{\omega_0}{\alpha_{eff,1} v_g} \tag{4.30}$$

where $\alpha_{eff,1}$ is the waveguide effective loss coefficient of ring 1, defined as

$$\alpha_{eff,1} = \alpha_0 + \frac{\beta P_{c1}}{A_{eff}} + \frac{\tau\sigma\beta P_{c1}^2}{2h\nu A_{eff}^2} \tag{4.31}$$

In Equation (4.31), α_0 is the linear loss coefficient, β is the TPA coefficient, A_{eff} is the effective area of the waveguide, σ is the FCA cross section, τ is the free carrier recombination lifetime, h is the Planck constant and ν is the light frequency. So,

$$P_{c1} = \frac{v_g^2\left(4|\kappa_2|^2 P_{in} T_{d,2} + 4|\kappa_1|^2 P_{in}\right)}{L_1^2\left(\alpha_{eff,1} v_g + \frac{|\kappa_2|^2 v_g}{L_1} + \frac{|\kappa_1|^2 v_g}{L_1}\right)^2} \tag{4.32}$$

Notice that in Equation (4.32), the power P_{b1} has been rewritten using the drop coefficient at the resonance frequency of the ring 2, as

$$P_{b1} = P_{in} T_{d,2} \tag{4.33}$$

where

$$T_{d,2} = \frac{|\kappa_1|^2|\kappa_2|^2 a_2}{1 - 2\sqrt{(1-|\kappa_1|^2)(1-|\kappa_2|^2)}a_2 + (\sqrt{(1-|\kappa_1|^2)(1-|\kappa_2|^2)}a_2)^2} \tag{4.34}$$

with

$$a_2 = e^{-\frac{\alpha_{eff,2} L_2}{2}} \tag{4.35}$$

and

$$\alpha_{eff,2} = \alpha_0 + \frac{\beta P_{c2}}{A_{eff}} + \frac{\tau\sigma\beta P_{c2}^2}{2h\nu A_{eff}^2} \tag{4.36}$$

The power circulating inside the resonator 2 is given by the following equation

$$P_{c2} = \frac{v_g\left(4|\kappa_a|^2 P_{b2} + 4|\kappa_b|^2 P_{in}\right)}{L_2\left(\dfrac{\omega_0}{Q_0} + |\kappa_a|^2 + |\kappa_b|^2\right)^2} \tag{4.37}$$

where the quantities $|\kappa_a|^2$ and $|\kappa_b|^2$ can be rewritten using (4.27) and (4.28), thus leading to Equation (4.38)

$$P_{c2} = \frac{v_g^2\left(4|\kappa_2|^2 P_{b2} + 4|\kappa_1|^2 P_{in}\right)}{L_2^2\left(\dfrac{\omega_0}{Q_0} + \dfrac{|\kappa_2|^2 v_g}{L_2} + \dfrac{|\kappa_1|^2 v_g}{L_2}\right)^2} \tag{4.38}$$

The ratio $\frac{\omega_0}{Q_0}$ and the power P_{b2} can be expressed using the following relations

$$Q_0 = \frac{\omega_0}{\alpha_{eff,2} v_g} \tag{4.39}$$

$$P_{b2} = P_{in} T_{d,1} \tag{4.40}$$

In (4.40), $T_{d,1}$ is the drop coefficient at the resonance frequency of the ring 1, i.e.,

$$T_{d,1} = \frac{|\kappa_1|^2|\kappa_2|^2 a_1}{1 - 2\sqrt{(1-|\kappa_1|^2)(1-|\kappa_2|^2)}a_1 + (\sqrt{(1-|\kappa_1|^2)(1-|\kappa_2|^2)}a_1)^2} \tag{4.41}$$

where

$$a_1 = e^{-\dfrac{\alpha_{eff,1} L_1}{2}} \tag{4.42}$$

The final equation of P_{c2} is therefore

$$P_{c2} = \frac{v_g^2\left(4|\kappa_2|^2 P_{in} T_{d,1} + 4|\kappa_1|^2 P_{in}\right)}{L_2^2\left(\alpha_{eff,2} v_g + \dfrac{|\kappa_2|^2 v_g}{L_2} + \dfrac{|\kappa_1|^2 v_g}{L_2}\right)^2} \tag{4.43}$$

The goal now is to solve the following nonlinear system, where the two unknowns are the circulating powers P_{c1} and P_{c2}, for different values of the input power P_{in}.

$$\begin{cases} P_{c1} = \dfrac{v_g^2(4|\kappa_2|^2 P_{in} T_{d,2} + 4|\kappa_1|^2 P_{in})}{L_1^2\Big(\alpha_{eff,1} v_g + \dfrac{|\kappa_2|^2 v_g}{L_1} + \dfrac{|\kappa_1|^2 v_g}{L_1}\Big)^2} \\ \\ P_{c2} = \dfrac{v_g^2(4|\kappa_2|^2 P_{in} T_{d,1} + 4|\kappa_1|^2 P_{in})}{L_2^2\Big(\alpha_{eff,2} v_g + \dfrac{|\kappa_2|^2 v_g}{L_2} + \dfrac{|\kappa_1|^2 v_g}{L_2}\Big)^2} \end{cases} \tag{4.44}$$

System (4.44) has been solved using the MATLAB function *fsolve* and Figures 4.4 - 4.6 show the results in terms of circulating powers, effective loss coefficients and drop coefficients, when $R_1 = 12\mu m$, $R_2 = 10\mu m$, $\kappa_1 = \kappa_2 = 0.04$, $\alpha_0 = 0.184 cm^{-1}$ and the input power P_{in} varies in the range of 0-200 mW.

As can be seen from Figure 4.4, the circulating power inside the ring 2 is higher than the circulating power inside the resonator 1, and that makes sense since the model in (4.44) states that the circulating power is inversely proportional to the radius of the ring. As a consequence of that, the effective loss coefficient $\alpha_{eff,2}$, associated to the ring 2, is larger than that of ring 1, as depicted in Figure 4.5. Notice that these loss coefficients dramatically increase with the increasing values of the input power. Figure 4.6 shows the drop coefficients of the two rings: when the value of the input power is very low, T_{d1} and T_{d2} are approximately equal to one, since the chosen value of the linear loss coefficient α_0 is very low. As the input power increases, they rapidly decrease.

4.3 Nonlinearities in straight waveguides

The goal of this section is to include nonlinear effects in straight waveguides. When considering a straight waveguide of length L, with a linear loss coefficient α_0, the

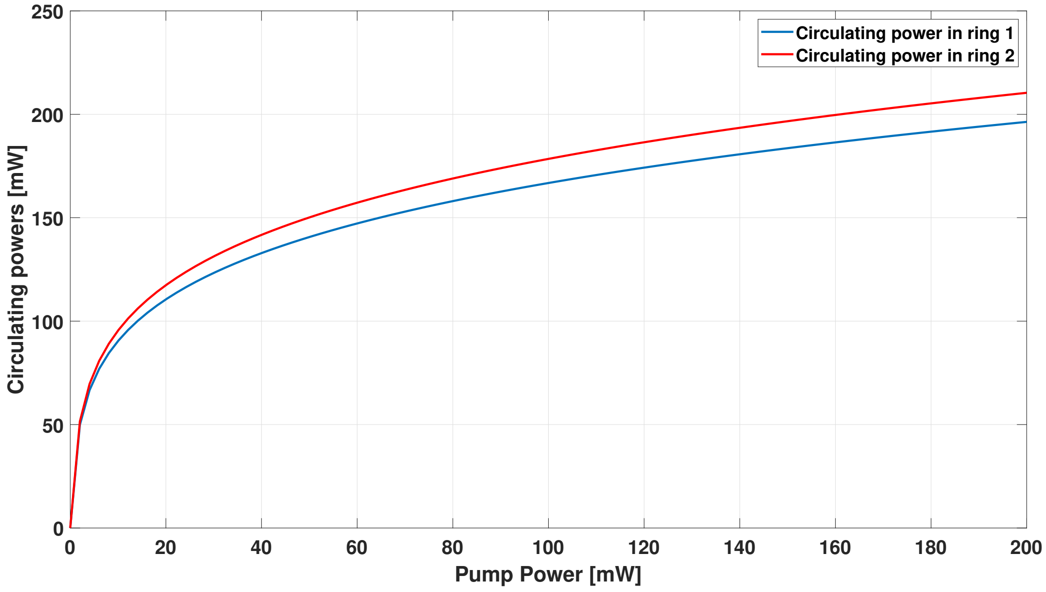

Figure 4.4: Circulating powers inside the ring 1 (blue) and ring 2 (red).

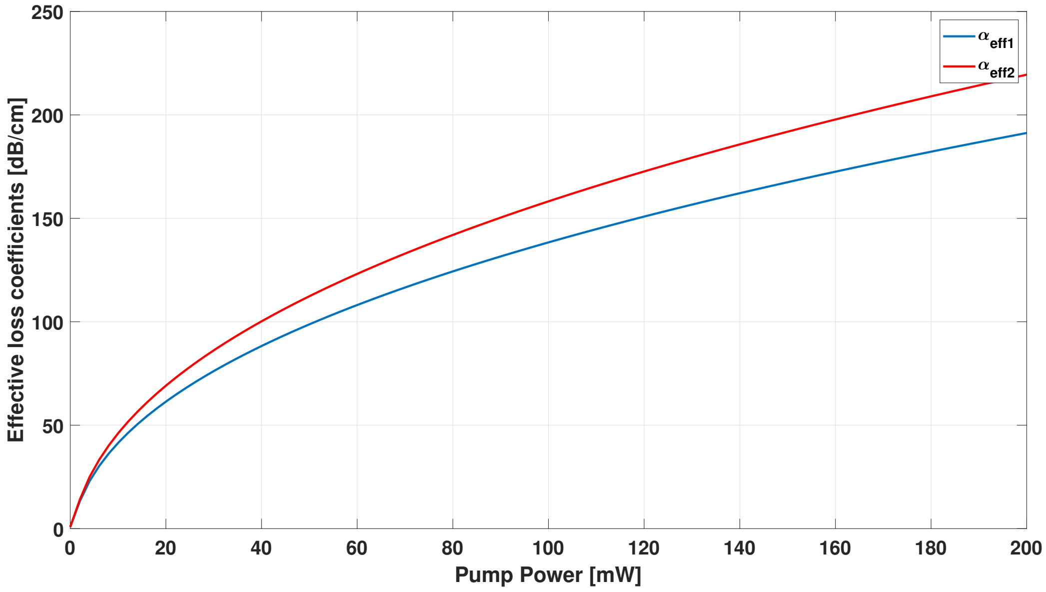

Figure 4.5: Effective loss coefficients of ring 1 (blue) and ring 2 (red).

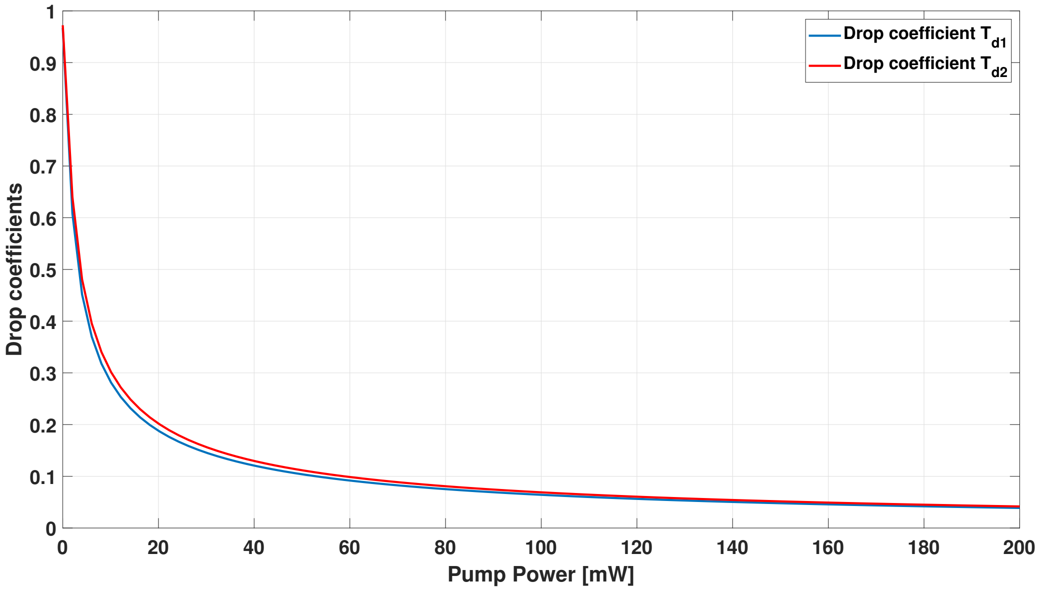

Figure 4.6: Drop coefficients of ring 1 (blue) and ring 2 (red).

equation that relates the input power P_{in} and the output power P_{out} is:

$$P_{out} = P_{in} e^{-\alpha_0 L} \tag{4.45}$$

When nonlinear effects are not negligible, α_0 must be replaced by α_{eff}, which is a function of the power propagating in the waveguide, as shown in Equations (4.31) or (4.36). The approach followed to develop the nonlinear model is shown in Figure 4.7, where a waveguide of length L is divided into sufficiently small k sections of length Δz. The idea behind this approach is to simultaneously consider forward and backward powers. In Figure 4.7, $P(section\ number)$ indicates the power propagating in that particular section; $P_+(section\ number)$ is the forward power entering that particular section while $P_-(section\ number)$ is the backward power outgoing from that section. The power propagating in each section can be written using the following equation:

$$P(i) = P_+(i) + P_-(i+1), \qquad i = 1 : k \tag{4.46}$$

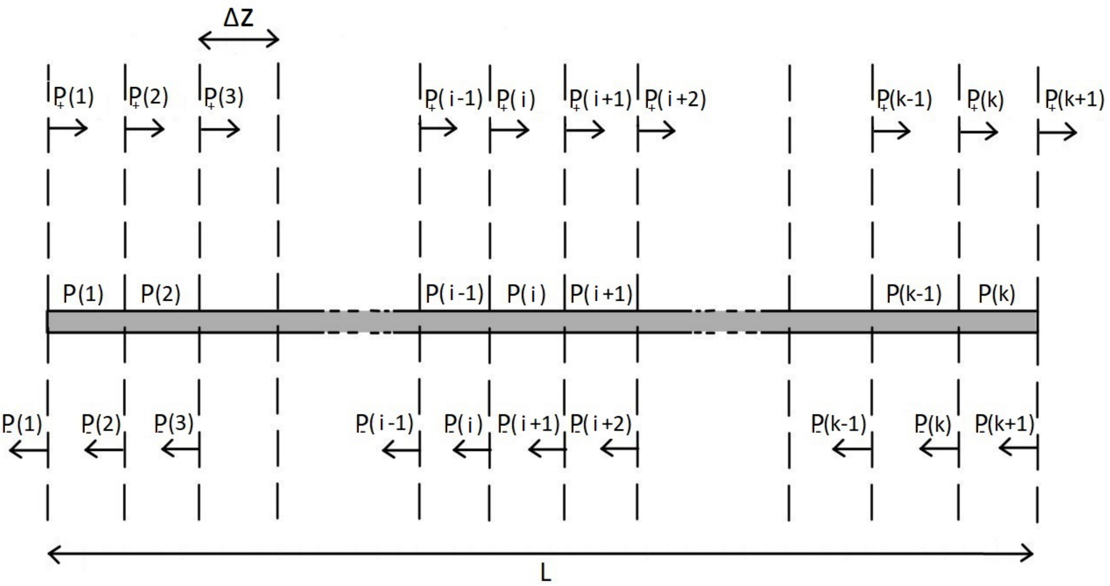

Figure 4.7: A representation of the approach used to include nonlinear effects in straight waveguides.

Previous equations are used in the following nonlinear system, to find the forward and backward powers in each section.

$$\begin{cases} P_+(i) = P_+(i-1)e^{-\alpha_{eff,i-1}\Delta z}, & i = 2 : k+1 \\ P_-(i) = P_-(i+1)e^{-\alpha_{eff,i}\Delta z}, & i = 1 : k \end{cases} \tag{4.47}$$

In fact, $\alpha_{eff,i-1}$ and $\alpha_{eff,i}$ depend on the power propagating in sections $i-1$ and i, respectively. Clearly, the number of equations in (4.47) increases with increasing number of sections. Notice that the index i in the first equation of (4.47) does not start with 1, since in our model $P_+(1)$ is assumed to be known. Analogously, the index of the second equation does not reach $k+1$ since $P_-(k+1)$ is already available. System (4.47) has been solved using the MATLAB function *fsolve*, and the following figures show the evolution of the forward and backward powers along the straight waveguide, the total power along the waveguide, obtained by simply summing the forward and backward powers at each section, and the associated effective loss coefficient, when 1) $L = 200\mu m$ and k=20, 2) $L = 800\mu m$ and k=80, and 3) $L = 2mm$ and k=200. In all three cases $P_+(1) = 20mW$, $P_-(21) = 10mW$, and $\alpha_0 = 0.184\ cm^{-1}$.

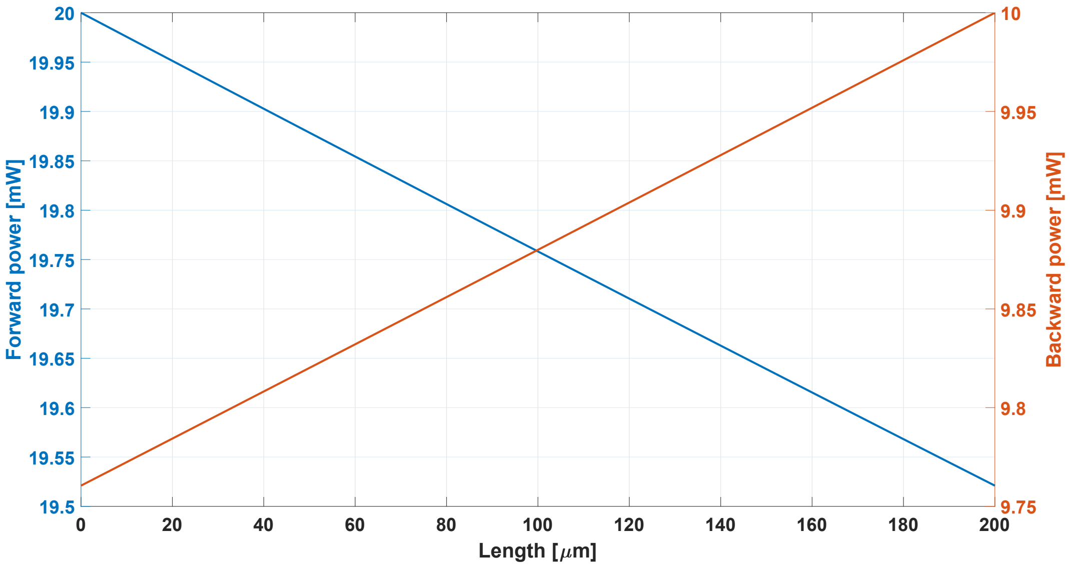

Figure 4.8: Forward and backward powers when L = 200μm.

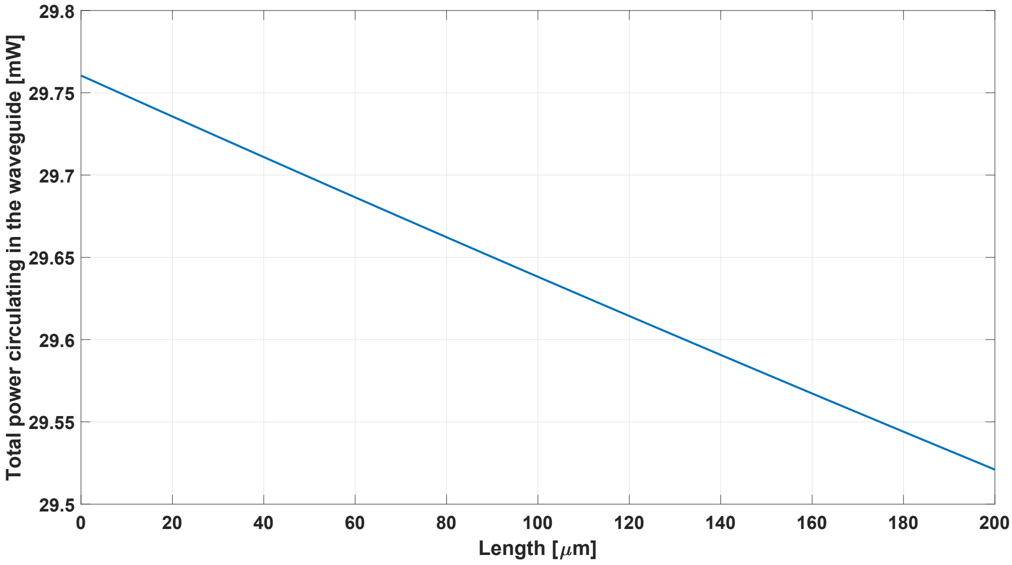

Figure 4.9: Total power when L = 200μm.

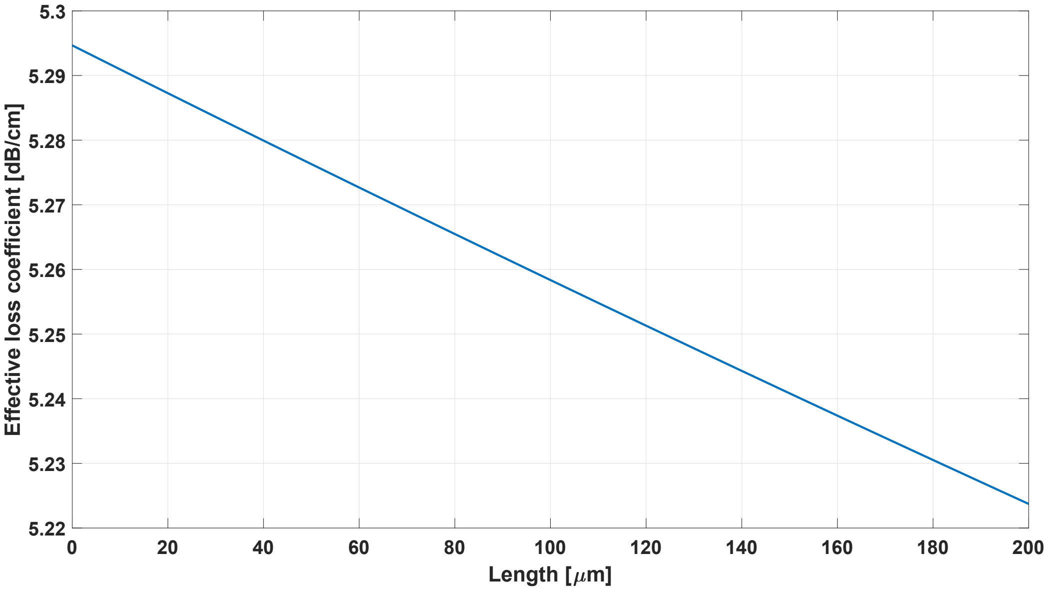

Figure 4.10: Effective loss coefficient when L = 200μm.

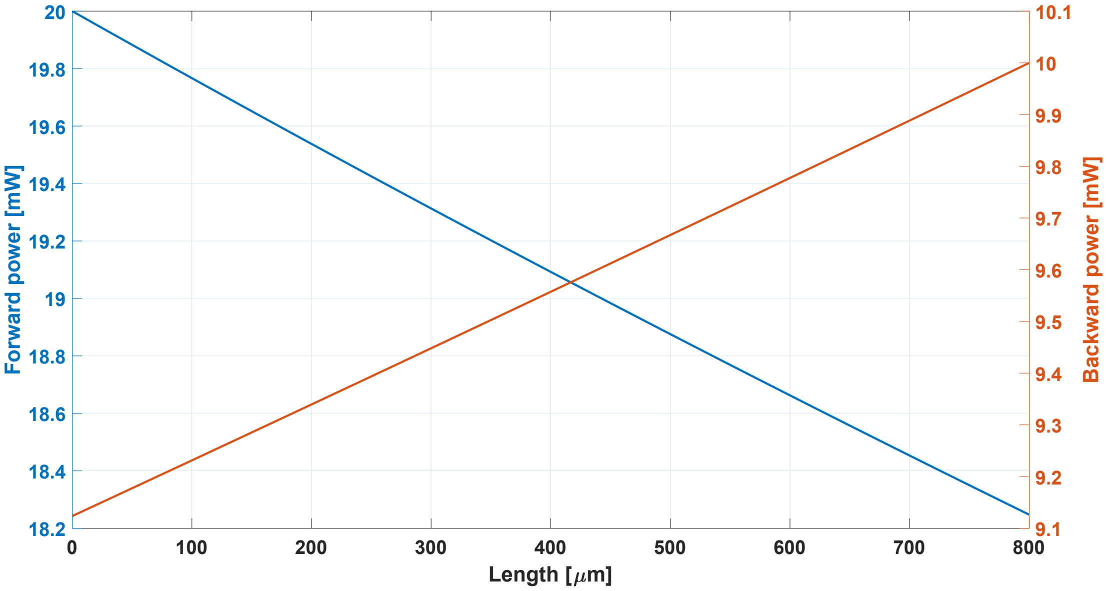

Figure 4.11: Forward and backward powers when L = 800μm.

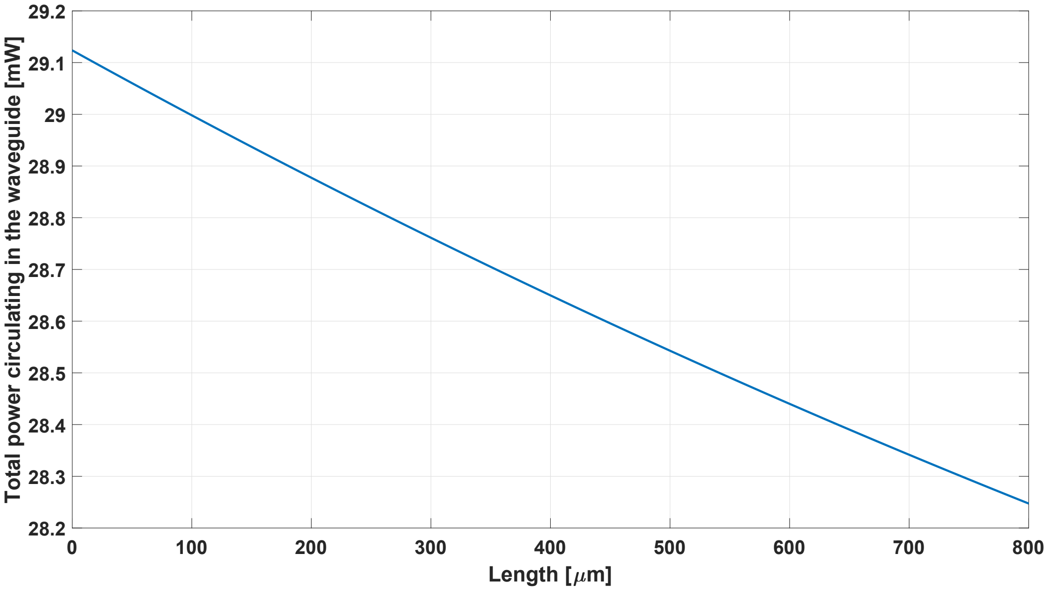

Figure 4.12: Total power when L = 800μm.

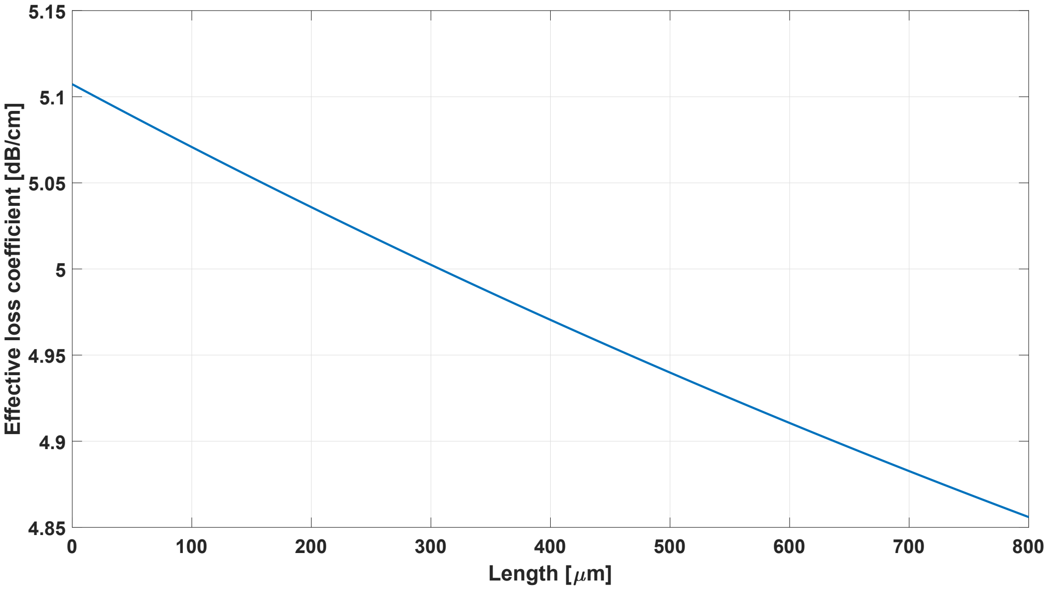

Figure 4.13: Effective loss coefficient when L = 800μm.

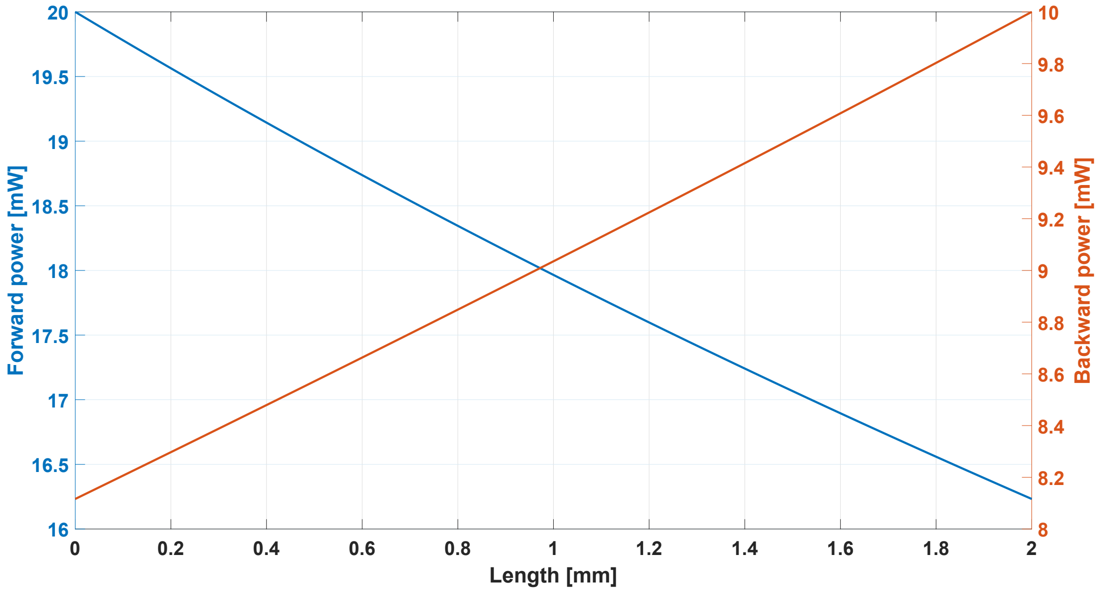

Figure 4.14: Forward and backward powers when L = 2mm

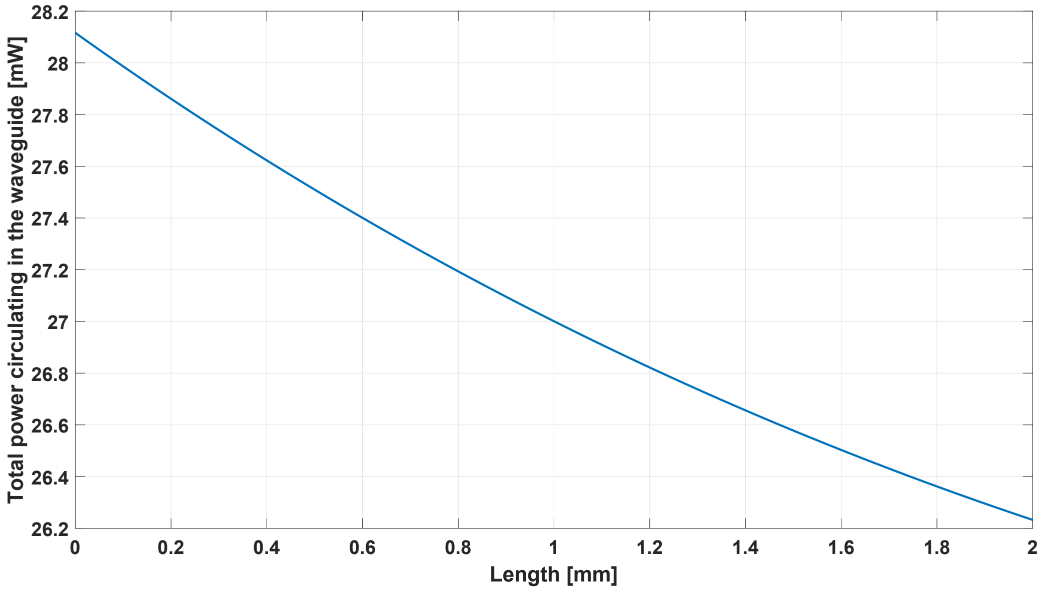

Figure 4.15: Total power when L = 2mm.

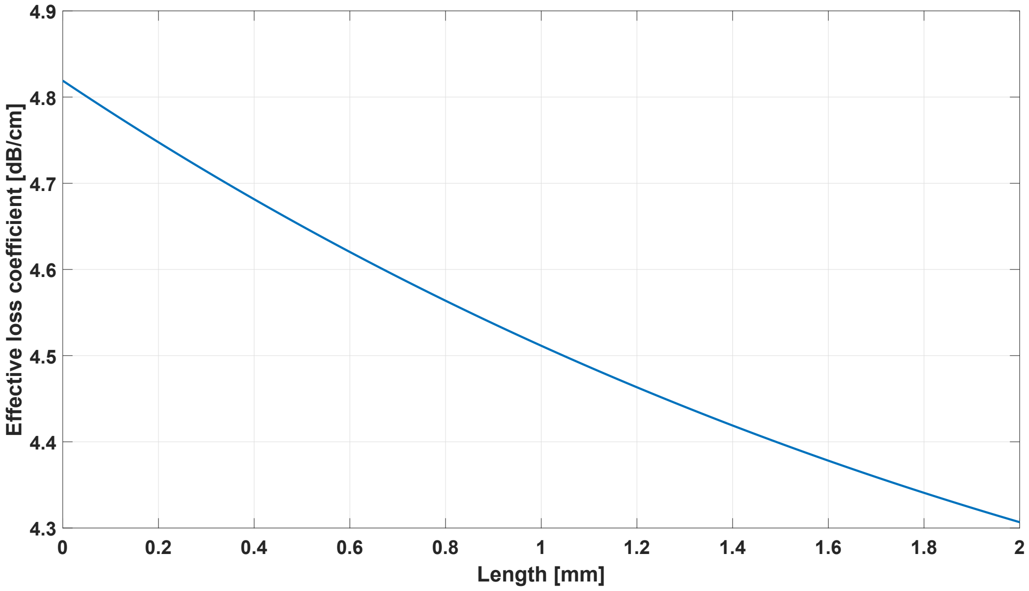

Figure 4.16: Effective loss coefficient when L = 2mm

Notice that the chosen values of k are different since the value of Δz is maintained constant at 10μm. As can be seen from the previous figures, the power that reaches the opposite side of the waveguide decreases as the length of the waveguide increases. The curves for the case in which L=200μm are more linear since the weight of the exponential function is negligible.

4.4 Global model

Once nonlinear effects have been included in ring resonators and in straight waveguides, the next step is to put these two models together. The approach followed to develop an overall model is shown in Figure 4.17. Here, the model of the straight waveguides has been used for the two arms of the Mach-Zehnder interferometer. In fact, it is assumed that the curvature of these two waveguides has negligible impact on the loss and therefore the waveguides can be modeled as straight waveguides. Furthermore, the model presented in Section 4.2 has been used for the two ring

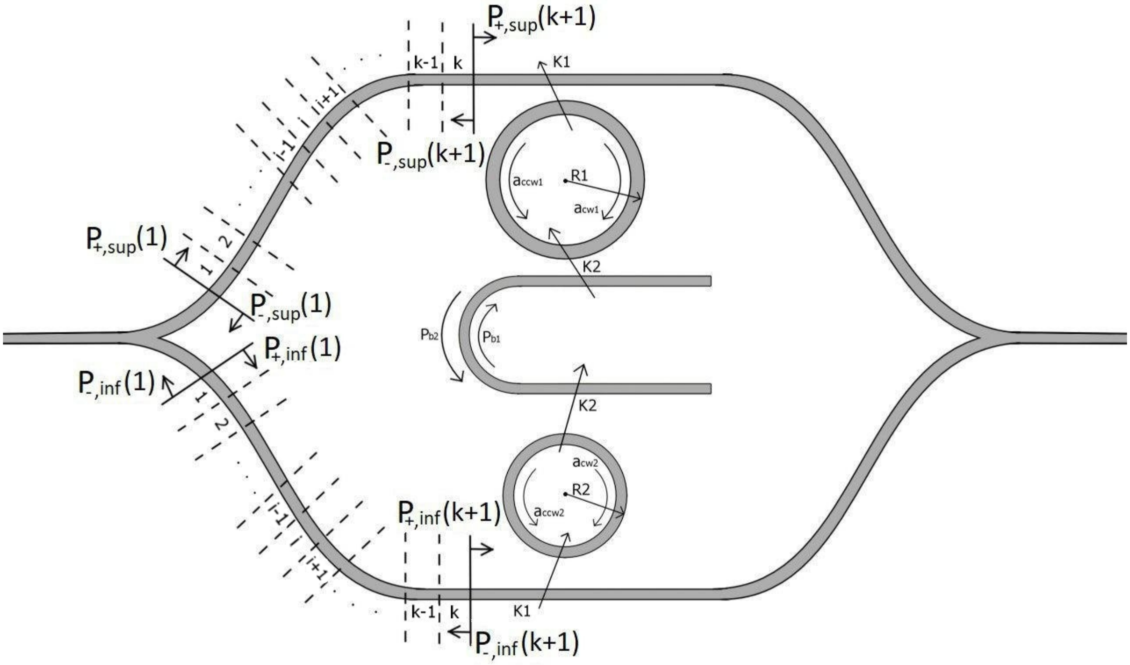

Figure 4.17: A representation of the approach used to develop the overall model.

resonators. A different notation is used in Figure 4.17: $P_{+,sup}(i)$ is the forward power entering section i, in the top arm; $P_{-,sup}(i)$ is the backward power outgoing from section i, in the top arm. $P_{+,inf}(i)$ and $P_{-,inf}(i)$ have the same meaning but they are related to the bottom arm. The idea is always to solve a nonlinear system of equations coming from the two models. In particular, system (4.48) has to be solved. Here, $T_{d,1}$ and $T_{d,2}$ are the drop coefficients, at the resonance frequency, of the two rings, defined by equations (4.41) and (4.34), respectively. Also, $\alpha_{eff,1}$ and $\alpha_{eff,2}$, in the last two equations, are the effective loss coefficients of the two rings, defined by Equations (4.31) and (4.36), respectively. Notice that third and sixth equations play a fundamental role in system (4.48), since they are written to link the two aforementioned models. Exactly the same thing can be said for the last two equations of the system. It is worth noting that index i in the first and fourth equations of (4.48) does not start with 1, since in our model $P_{+,sup}(1)$ and $P_{+,inf}(1)$ are assumed to be known. System (4.48) has been solved using the

MATLAB function *fsolve*, and Figures 4.18 and 4.19 show the evolution of the forward and backward powers along the straight waveguides of the two arms of the Mach-Zehnder interferometer.

$$\begin{cases} P_{+,sup}(i) = P_{+,sup}(i-1)e^{-\alpha_{eff,i-1}\Delta z}, & i = 2:k+1 \\ P_{-,sup}(i) = P_{-,sup}(i+1)e^{-\alpha_{eff,i}\Delta z}, & i = 1:k \\ P_{-,sup}(i) = P_{+,inf}(i)T_{d,1}T_{d,2}, & i = k+1 \\ P_{+,inf}(i) = P_{+,inf}(i-1)e^{-\alpha_{eff,i-1}\Delta z}, & i = 2:k+1 \\ P_{-,inf}(i) = P_{-,inf}(i+1)e^{-\alpha_{eff,i}\Delta z}, & i = 1:k \\ P_{-,inf}(i) = P_{+,sup}(i)T_{d,1}T_{d,2}, & i = k+1 \\ \\ P_{c1} = \dfrac{v_g^2(4|\kappa_2|^2 P_{+,inf}(i)T_{d,2} + 4|\kappa_1|^2 P_{+,sup}(i))}{L_1^2\Big(\alpha_{eff,1}v_g + \dfrac{|\kappa_2|^2 v_g}{L_1} + \dfrac{|\kappa_1|^2 v_g}{L_1}\Big)^2}, & i = k+1 \\ \\ P_{c2} = \dfrac{v_g^2(4|\kappa_2|^2 P_{+,sup}(i)T_{d,1} + 4|\kappa_1|^2 P_{+,inf}(i))}{L_2^2\Big(\alpha_{eff,2}v_g + \dfrac{|\kappa_2|^2 v_g}{L_2} + \dfrac{|\kappa_1|^2 v_g}{L_2}\Big)^2}, & i = k+1 \end{cases} \tag{4.48}$$

In this particular simulation, the values of the radii of the two rings are $R1 = 12\mu m$ and $R2 = 10\mu m$, coupling coefficients κ_1 and κ_2 are both set to 0.04 and the length of the top and bottom straight waveguides of the interferometer is $L = 1mm$. Also, $P_{+,sup}(1)$ and $P_{+,inf}(1)$ are both set to $20mW$. Figures (4.18) and (4.19) are basically identical since the overall structure is strongly symmetric. Even if the values of the coupling coefficients were different, the situation would not change.

4.4.1 Calculation of $r_{eff\_MZ}(\omega)$

The goal of this section is to compute the optical electric field effective reflectivity at the splitter of the Mach-Zehnder interferometer, $r_{eff\_MZ}(\omega)$, using the overall

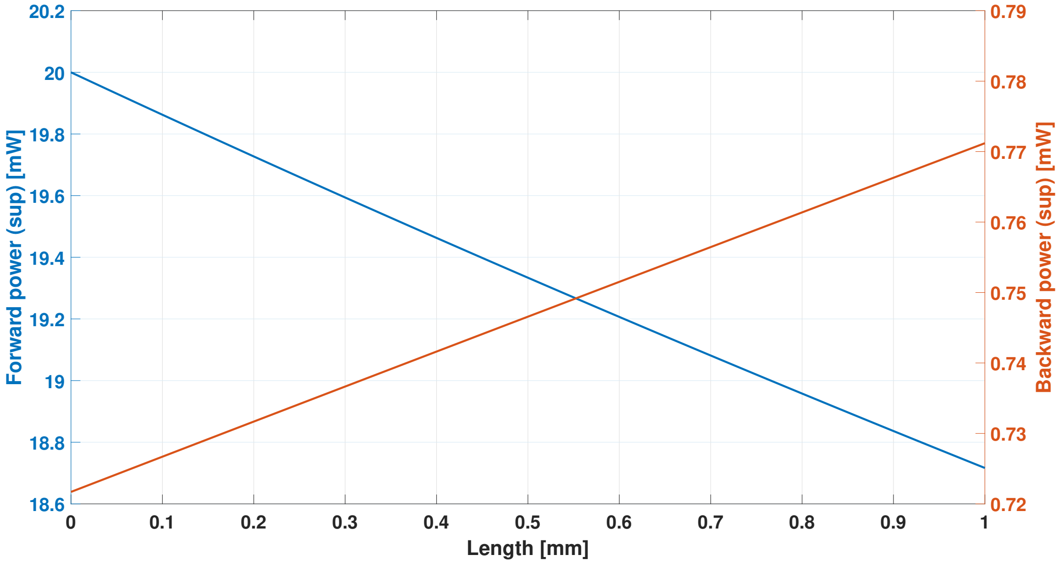

Figure 4.18: Forward and backward power evolutions along the top arm of the interferometer.

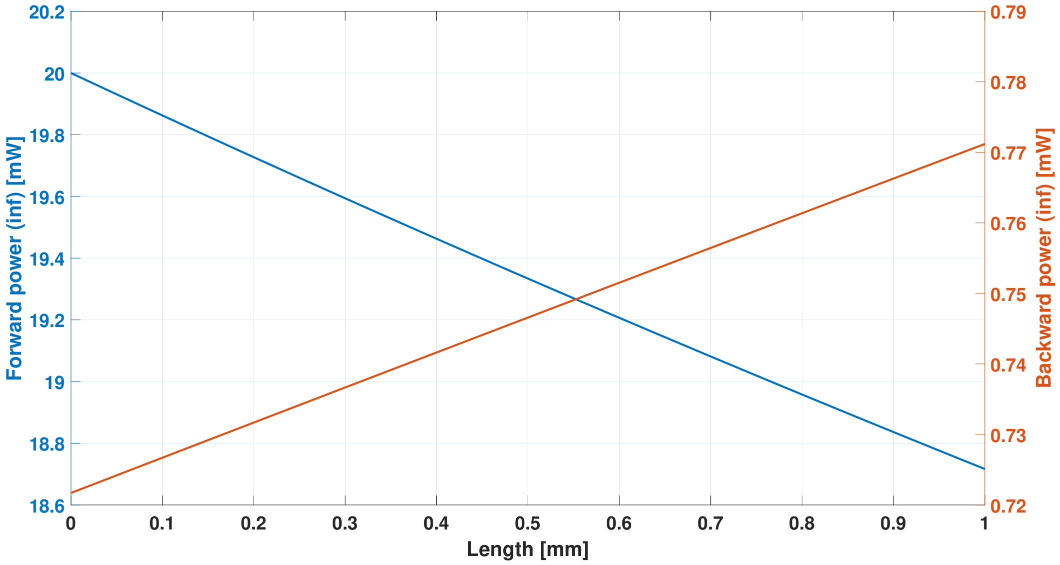

Figure 4.19: Forward and backward power evolutions along the bottom arm of the interferometer.

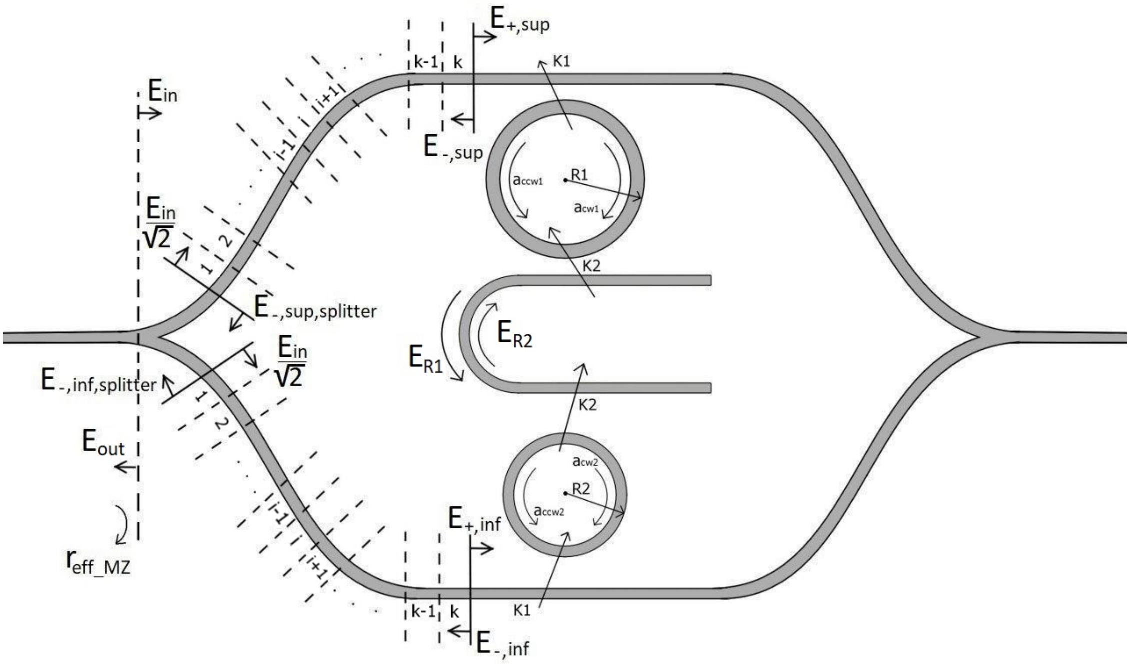

Figure 4.20: A representation of the approach used to compute $r_{eff\_MZ}(\omega)$.

model developed in Section 4.4. Differently from previous sections, in which the analysis has been carried out at the resonance frequency, here, it is necessary to derive the value of $r_{eff\_MZ}(\omega)$ as the frequency changes, in such a way that it will be possible to plot its frequency spectrum. The approach followed to obtain $r_{eff\_MZ}(\omega)$ is shown in Figure 4.20. All the quantities in Figure 4.20 are defined by the following equations:

$$E_{+,sup} = \frac{E_{in}}{\sqrt{2}}\, e^{-j\beta(\omega)L}\, t_{+,sup} \tag{4.49}$$

$$E_{R1} = E_{+,sup}\, t_{d,1} \tag{4.50}$$

$$E_{-,inf} = E_{R1}\, t_{d,2} \tag{4.51}$$

$$E_{-,inf,splitter} = E_{-,inf}\; e^{-j\beta(\omega)L}\; t_{-,inf} \tag{4.52}$$

$$E_{+,inf} = \frac{E_{in}}{\sqrt{2}}\; e^{-j\beta(\omega)L}\; t_{+,inf} \tag{4.53}$$

$$E_{R2} = E_{+,inf}\; t_{d,2} \tag{4.54}$$

$$E_{-,sup} = E_{R2}\; t_{d,1} \tag{4.55}$$

$$E_{-,sup,splitter} = E_{-,sup}\; e^{-j\beta(\omega)L}\; t_{-,sup} \tag{4.56}$$

In previous equations, E_{in} is the electric field before the splitter of the interferometer and L is the length of the top and bottom arms. The propagation constant $\beta(\omega)$ is defined as

$$\beta(\omega) = \beta_0 + \frac{\partial\beta}{\partial\omega}(\omega - \omega_0) \tag{4.57}$$

where

$$\beta_0 = \frac{\omega_0}{c} n_{eff} = \frac{2\pi}{\lambda_0} n_{eff} \tag{4.58}$$

and

$$\frac{\partial\beta}{\partial\omega} = \frac{1}{v_g} = \frac{n_g}{c} \tag{4.59}$$

In Equations (4.57) - (4.59), ω_0, c, n_{eff}, v_g and n_g are the resonance freqency, the speed of light, the effective refractive index, the group velocity and the group index, respectively. $t_{d,1}$ and $t_{d,2}$ are the electric field drop coefficients of the two rings, given by

$$t_d = \frac{-k_1^* k_2 A^{1/4} e^{j\phi/2}}{1 - \sqrt{A} t_1^* t_2^* e^{j\phi}} \tag{4.60}$$

where

$$\phi = \phi(\omega) = 2\pi R \cdot \beta(\omega) \tag{4.61}$$

$$A = e^{-\alpha_{eff} \cdot 2\pi R} \tag{4.62}$$

$$t_1 = \sqrt{1 - |k_1|^2} \tag{4.63}$$

$$t_2 = \sqrt{1 - |k_2|^2} \tag{4.64}$$

The quantities $t_{+,sup}$, $t_{+,inf}$, $t_{-,sup}$ and $t_{-,inf}$ are the forward and backward electric field transmission coefficients of the top and bottom waveguides of the interferometer, defined by the following relations (the notation used for powers is equal to that used in Figure 4.17):

$$t_{+,sup} = \sqrt{\frac{P_{+,sup}(k+1)}{P_{+,sup}(1)}} \tag{4.65}$$

$$t_{+,inf} = \sqrt{\frac{P_{+,inf}(k+1)}{P_{+,inf}(1)}} \tag{4.66}$$

$$t_{-,sup} = \sqrt{\frac{P_{-,sup}(1)}{P_{-,sup}(k+1)}} \tag{4.67}$$

$$t_{-,inf} = \sqrt{\frac{P_{-,inf}(1)}{P_{-,inf}(k+1)}} \tag{4.68}$$

Notice that the values of power in Equations (4.65) - (4.68) and the effective loss coefficients of the two rings in (4.62), are obtained from the model developed in Section 4.4. The sum of the backward electric fields along the two arms of the interferometer provides the total backward electric field E_{out}, given by

$$E_{out} = \frac{E_{-,sup,splitter} + E_{-,inf,splitter}}{\sqrt{2}} \tag{4.69}$$

Therefore, the optical electric field effective reflectivity at the splitter of the interferometer is

$$r_{eff\_MZ}(\omega) = \frac{E_{out}}{E_{in}} \tag{4.70}$$

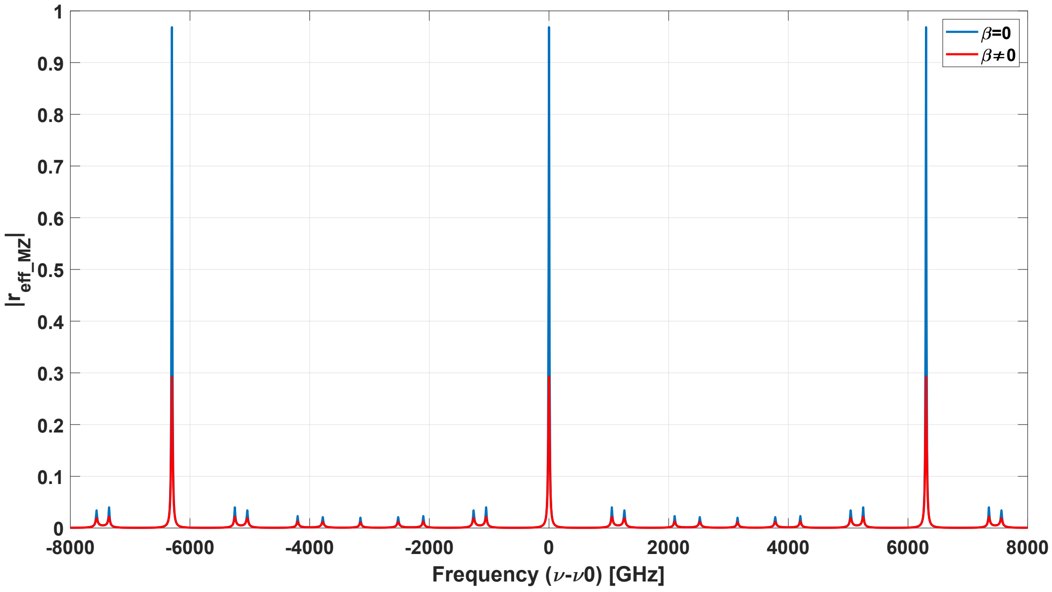

Figure 4.21: Modulus of the optical electric field effective reflectivity at the splitter of the interferometer, both in the linear and nonlinear case.

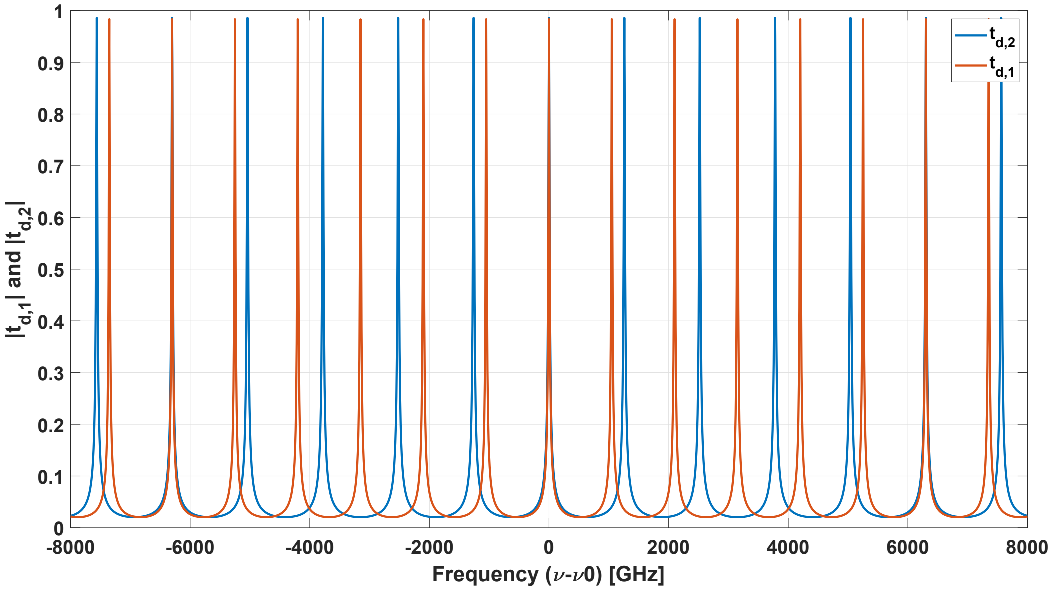

Figure 4.22: Modules of the drop coefficients of the two rings in the linear case.

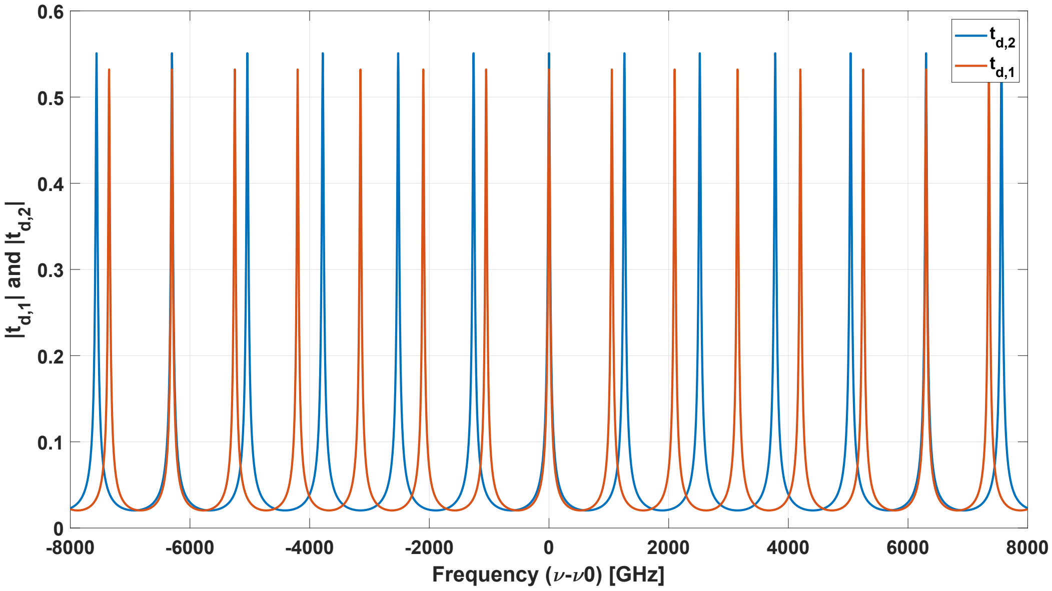

Figure 4.23: Modules of the drop coefficients of the two rings in the nonlinear case.

Notice that $r_{eff\_MZ}(\omega)$ is a complex number whose modulus and phase depend on frequency. Figure 4.21 shows the behavior of the modulus of the optical electric field effective reflectivity $r_{eff\_MZ}(\omega)$, both in the linear and nonlinear case. Clearly, at the resonance frequencies, the nonlinear values of the reflectivity are significantly lower than those of the linear case. Also, smaller peaks are observable since the drop coefficients of the two rings are not aligned at those frequencies. In this respect, Figures 4.22 and 4.23, show the drop coefficients of the two rings in the linear and nonlinear case, respectively. Due to nonlinear effects, the values of the drop coefficients in Figure 4.23 are much smaller than those in Figure 4.22. Furthermore, both figures are a clear example of application of the Vernier effect.

4.4.2 Calculation of $r_{eff\_SOA}(\omega)$

Once $r_{eff\_MZ}(\omega)$ has been found, the next step is the computation of the optical electric field effective reflectivity at the RSOA AR facet, $r_{eff\_SOA}(\omega)$. The approach

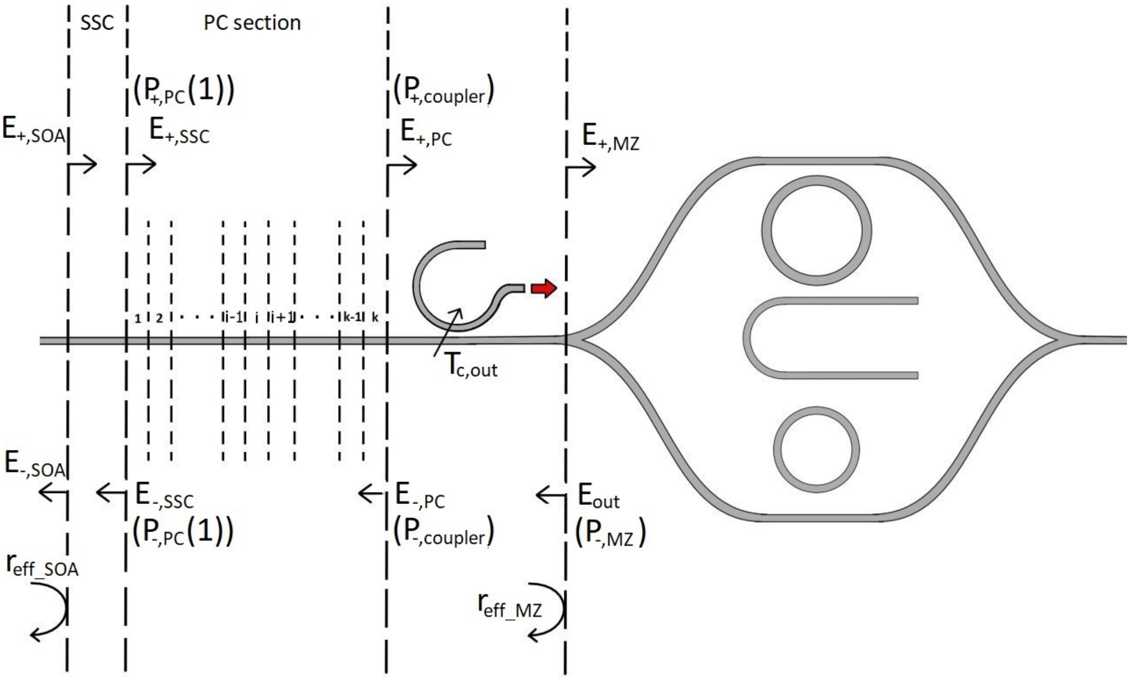

Figure 4.24: A representation of the approach used to compute $r_{eff\_SOA}(\omega)$.

followed to achieve this goal is shown in Figure 4.24. Notice that the phase control section has been studied by using the model for straight waveguides developed in Section 4.3. The only difference is that, now, the two known powers are those on the right side of the waveguide, as will be shown in a moment. Remember that the spot-size-converter (SSC) insertion loss is 2dB.

Starting with Equation (4.69), one can obtain the corresponding power at the resonance frequency as

$$P_{-,MZ} = |E_{out}|^2 \tag{4.71}$$

The transmitted power, in the backward direction, is given by

$$P_{-,coupler} = P_{-,MZ}(1 - T_{c,out}) \tag{4.72}$$

while the power at the input of the coupler, in the forward direction, is

$$P_{+,coupler} = \frac{P_{out,target}}{T_{c,out}} \tag{4.73}$$

At this point, the model of the straight waveguide is stimulated with power values given by (4.72) and (4.73), and it returns the forward and backward powers in each section of the phase control section. These powers are indicated as $P_{+,PC}$ and $P_{-,PC}$. Using the notation in Figure 4.24, one can write the following equations:

$$E_{-,PC} = E_{out}\sqrt{1 - T_{c,out}} \tag{4.74}$$

$$E_{-,SSC} = E_{-,PC}\; e^{-j\beta(\omega)L_{PC}}\sqrt{\frac{P_{-,PC}(1)}{P_{-,coupler}}} \tag{4.75}$$

$$E_{-,SOA} = E_{-,SSC}\sqrt{10^{-\frac{2dB}{10}}} \tag{4.76}$$

$$E_{+,MZ} = \frac{E_{out}}{r_{eff\_MZ}(\omega)} \tag{4.77}$$

$$E_{+,PC} = \frac{E_{+,MZ}}{\sqrt{1 - T_{c,out}}} \tag{4.78}$$

$$E_{+,SSC} = E_{+,PC}\; e^{j\beta(\omega)L_{PC}}\sqrt{\frac{P_{+,PC}(1)}{P_{+,coupler}}} \tag{4.79}$$

$$E_{+,SOA} = \frac{E_{+,SSC}}{\sqrt{10^{-\frac{2dB}{10}}}} \tag{4.80}$$

Therefore, the optical electric field effective reflectivity at the RSOA AR facet is

$$r_{eff\_SOA}(\omega) = \frac{E_{-,SOA}}{E_{+,SOA}} \tag{4.81}$$

A comparison between $|r_{eff\_SOA}(\omega)|$ and $|r_{eff\_MZ}(\omega)|$ is depicted in Figure 4.25. Clearly, $|r_{eff\_SOA}(\omega)|$ is significantly lower than $|r_{eff\_MZ}(\omega)|$ because of the structures (coupler, PC section, SSC) present between the RSOA AR facet and the splitter of the interferometer. Figure 4.25 has been obtained using $L_{PC} = 1mm$ and $P_{out,target} = 20mW$.

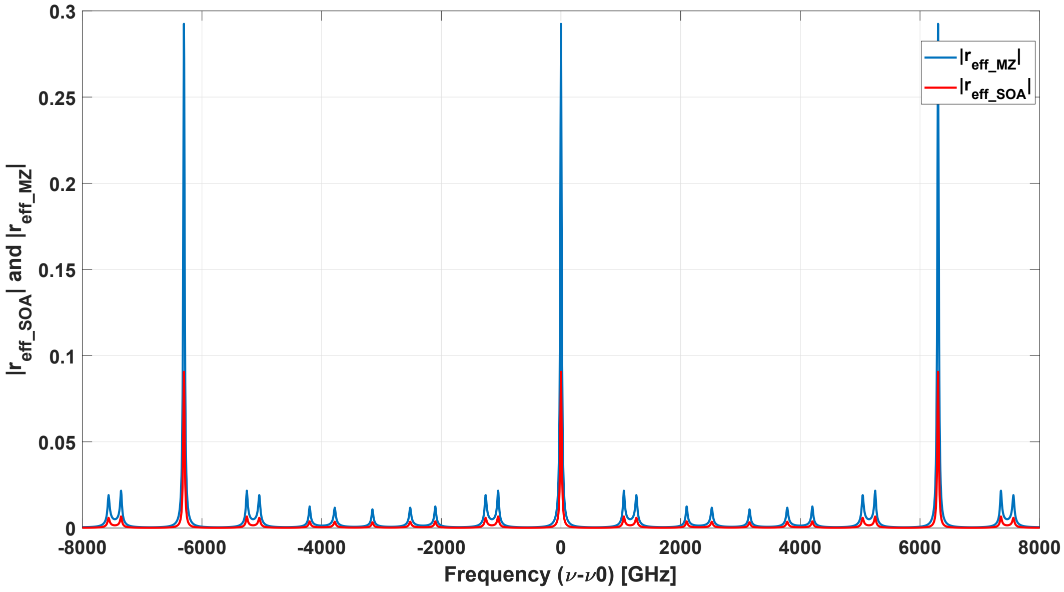

Figure 4.25: Graphical comparison between $|r_{eff\_SOA}(\omega)|$ and $|r_{eff\_MZ}(\omega)|$.

4.5 Validation of the model

The scope of this section is to show the P-I characteristic of the hybrid laser, both in the linear and nonlinear case. In what follows, the nonlinear case differs from the linear case in that the calculation of $r_{eff\_SOA}(\omega)$ involves nonlinear effects. In particular, three approaches have been used. Notice that the second and third approaches have been developed to validate the results produced by the first approach. The three methods are described below.

1. the value of the output power is fixed and the corresponding value of the bias current is generated using Equation (2.16). This has been done for several values of the output power, both in the linear and nonlinear case;

2. here, the value of the bias current, in the linear case, is fixed and the corresponding value of the output power is generated using the inverse formula of

(2.16), i.e.,

$$P_{out,target} = \frac{\hbar\omega_0\eta_i}{q}\frac{\alpha_m}{\alpha_m+\alpha_i}\frac{|t_{eff,out}(\nu_0)|^2(I_{bias,SOA}-I_{th})}{(1-|r_{eff\_SOA}(\nu_0)|^2)+\left(\sqrt{\frac{r_{eff\_SOA}(\nu_0)}{R_{HR}}}(1-R_{HR})\right)} \tag{4.82}$$

Once the value of the output power is generated using the aforementioned value of the bias current, it is used to recompute the values of $r_{eff\_SOA}(\omega)$, I_{th} etc. With these new values, the output power is recomputed always using Equation (4.82). This process is repeated a certain number of times and the last value of the output power is saved. This has been done both in the linear and nonlinear case, for several values of the linear bias current;

3. also in the third approach the value of the bias current, in the linear case, is fixed, but the corresponding value of the output power is generated using the rate equations, without the need of any iteration. In particular, the following equations have been used:

$$N_{p0}^{+} = \frac{1}{\hbar\omega_0 v_g}\frac{P_{out,target}}{|t_{eff,out}(\nu_0)|^2} \tag{4.83}$$

$$V_{SOA} = L_{SOA}W_{SOA}H_{SOA} \tag{4.84}$$

$$N_{tr} = 2.1\cdot 10^{17}cm^{-3}V_{SOA} \tag{4.85}$$

$$\Gamma g = g_0 \ln\left(\frac{N}{N_{tr}}\right) \tag{4.86}$$

$$\bar{g} = \Gamma g - \alpha_i \tag{4.87}$$

$$N_p = N_{p0}^{+}|r_{eff\_SOA}(\nu_0)|^2(R_{HR}\,e^{2\bar{g}L_{SOA}} - R_{HR}\,e^{\bar{g}L_{SOA}} - 1 + e^{\bar{g}L_{SOA}})\frac{1}{\bar{g}} \tag{4.88}$$

In previous equations, N_{p0}^{+} is the photon density propagating forward in the RSOA and incident on the AR facet, V_{SOA} is the active medium volume, N_{tr} is the transparency carrier density, Γg is the modal gain and N_p is the total photon density in the RSOA.

The rate equations under steady-state conditions are given by:

$$\begin{cases} \dfrac{\eta_i I_{bias,linear}}{e} - \dfrac{N}{\tau} - \Gamma v_g g N_p = 0 \\ \Gamma \beta_{sp} \eta_r \dfrac{N}{\tau} + \Gamma v_g g N_p - N_p v_g(\alpha_i + \alpha_m) = 0 \end{cases} \tag{4.89}$$

Here, N is the carrier density, N_p is the photon density, Γ is the confinement factor, β_{sp} is the spontaneous emission factor, η_r is the radiative efficiency and τ is the carrier lifetime. The unknows of system (4.89) are the carrier density N and the output power $P_{out,target}$. Notice that the dependency on the output power is given by the quantity $|r_{eff\_SOA}(\nu_0)|^2$, that one can find in Equation (4.88). As a consequence of that, also α_m depends on $P_{out,target}$. System (4.89) has been solved using the MATLAB function *fsolve*, both in the linear and nonlinear case, for several values of the linear bias current.

The P-I characteristics of the hybrid laser, obtained with the three approaches, are shown in Figure 4.26. As one can see, the slope of the nonlinear characteristics is higher than that of the linear characteristics. In other words, for example, if we fix the value of the bias current, the corresponding output power is higher in the nonlinear case. This is justified by the fact that the gain model (see Figure 4.27), used to obtain the values of the threshold current density, J_{th}, has a very high slope (g_0). To better understand, let's look, for example, at Equation (4.82), and, in particular, at the following two terms:

$$1)\ \frac{\alpha_m}{\alpha_m + \alpha_i} \qquad\qquad 2)\ (I_{bias,SOA} - I_{th})$$

When nonlinear effects are included, the value of the term α_m is larger than that in the linear case, simply because the effective reflectivity at the RSOA AR facet

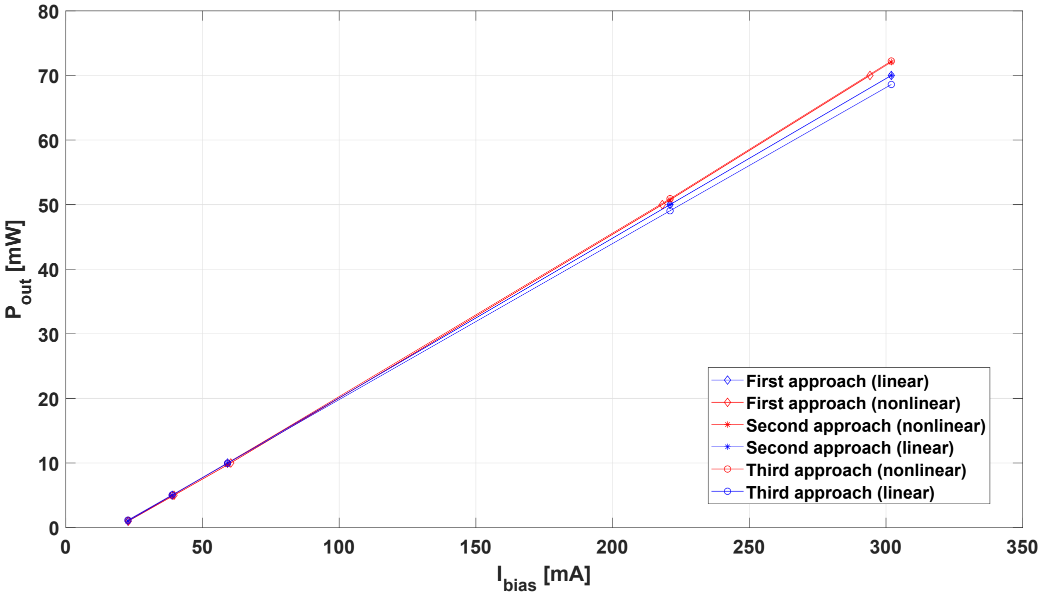

Figure 4.26: P-I characteristics obtained with the three approaches, both in the linear and nonlinear case.

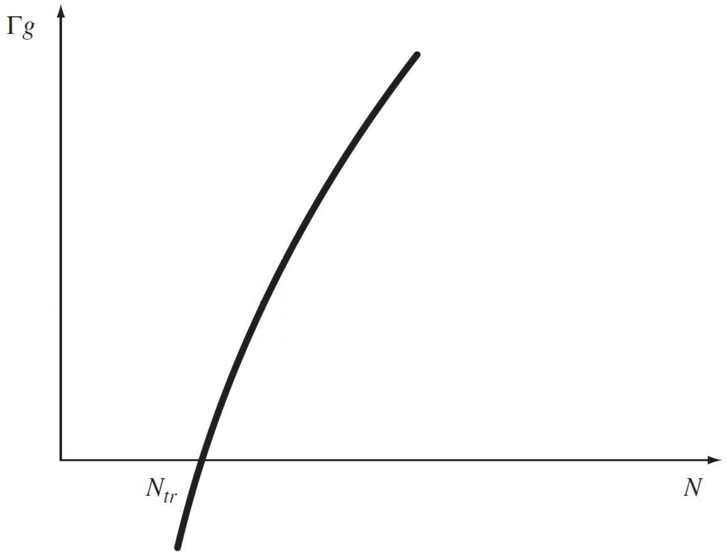

Figure 4.27: Schematic illustration of modal gain versus injected carrier density.

is lower. Furthermore, as the power sent to the mirror increases, the value of α_m increases as well. As a consequence of that, ratio 1) tends to increase. Clearly, the modal gain increases but since the slope of the model is very high, the corresponding increase in the value of the threshold current is not sufficient to compensate the increase of ratio 1). This justifies the behavior of the curves depicted in Figure 4.26. In view of the above discussion, we try to decrease the value of g_0. However, nothing can still be said since, unfortunately, the third approach do not converge. As a consequence of that, we continued to use a high value for g_0 but the value of the threshold current is increased by multiplying it by 2,3 or 4: it is just another way to obtain the reduction of the slope of the modal gain.

With this in mind, it is possible to understand the impact of nonlinear effects on some important figures of merits of the hybrid laser, such as the output power, the WPE and the linewidth $\Delta\nu$. Clearly, this impact strongly depends on the chosen values of the coupling coefficients κ_1, κ_2 and $T_{c,out}$. In the following figures $\kappa_1 = \kappa_2 = 0.01$ and $T_{c,out} = 0.75$. Figure 4.28 shows the P-I characteristics and the power at the input of the MZI splitter, P_{in_MZ}, as a function of the bias current, both in the linear and nonlinear case. P_{in_MZ} has been reported to show the amount of power that gives rise to nonlinear effects. As one can see, nonlinearities do not have much impact on the values of P_{out}. The same thing can be said for the values of WPE, shown in Figure 4.29. Figure 4.30 shows the circulating powers inside the two rings, $P_{c,1}$ and $P_{c,2}$, as a function of the output power P_{out}, both in the linear (left) and nonlinear (right) case: powers on the right are much lower than those on the left due to nonlinear effects. The corresponding values of the effective loss coefficients, $\alpha_{eff,1}$ and $\alpha_{eff,2}$, are depicted in Figure 4.31. In this particular design $\Delta\nu$ is greatly affected by the presence of nonlinear effects and in fact, as shown in Figure 4.32, the difference between the red and blue curves is almost 2MHz, around 20mW. Finally, the effective length L_{eff} and the parameter $(\alpha_m + \alpha_i)/(I_{bias,SOA} - I_{th})$ (see Equation 2.19), whose behavior is depicted in Figures 4.33 and 4.34 respectively, justify the results shown in Figure 4.32. In these simulations, the value of the threshold current is multiplied by 4 and $\alpha_0 = 0.8\text{dB/cm}$.

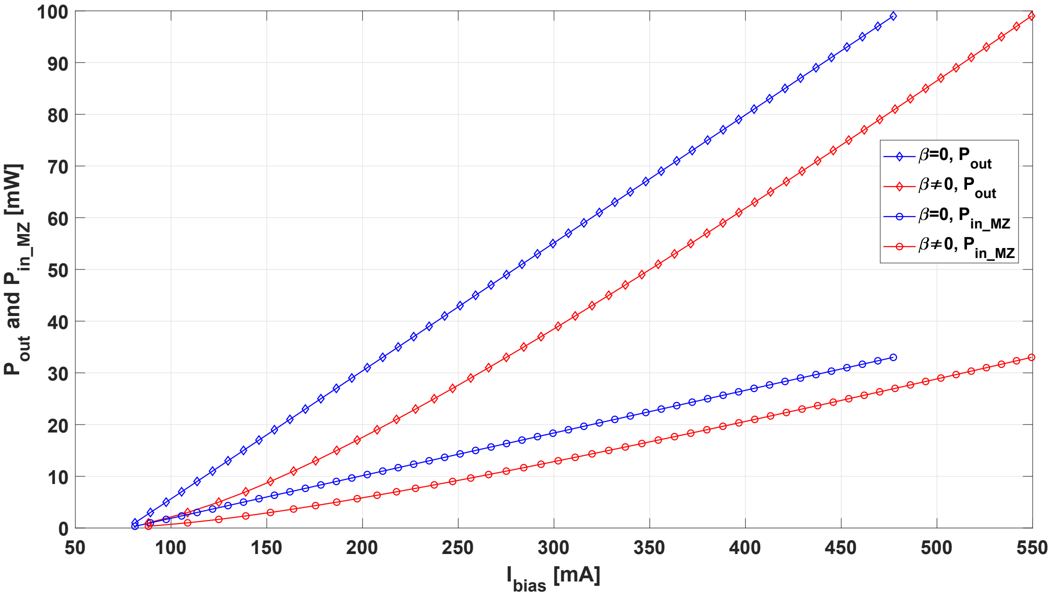

Figure 4.28: P-I characteristics and P_{in_MZ} in both linear and nonlinear case when $\kappa_1 = \kappa_2 = 0.01$ and $T_{c,out} = 0.75$.

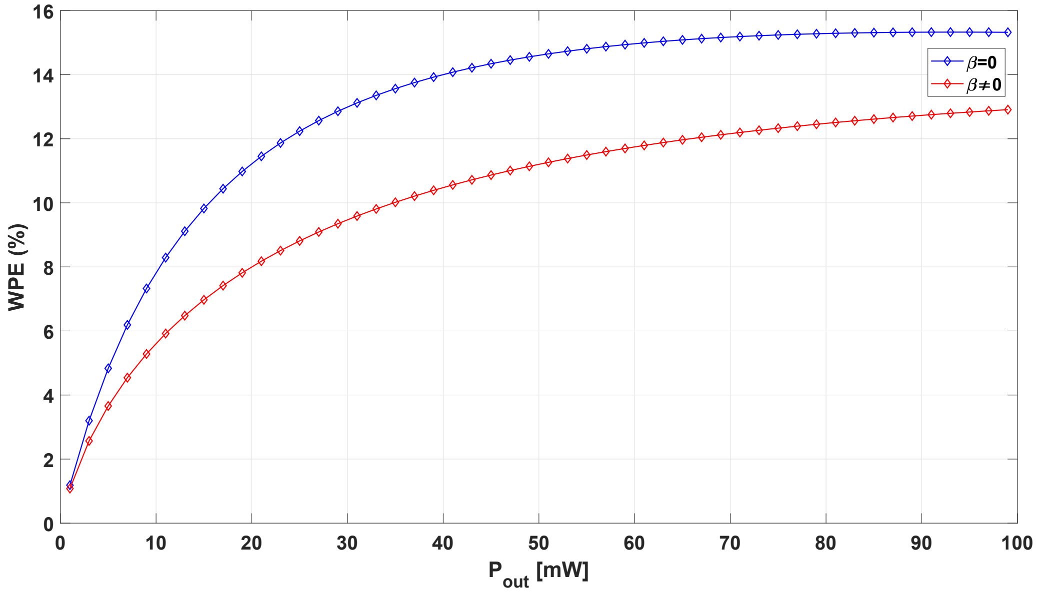

Figure 4.29: WPE in both linear and nonlinear case when $\kappa_1 = \kappa_2 = 0.01$ and $T_{c,out} = 0.75$.

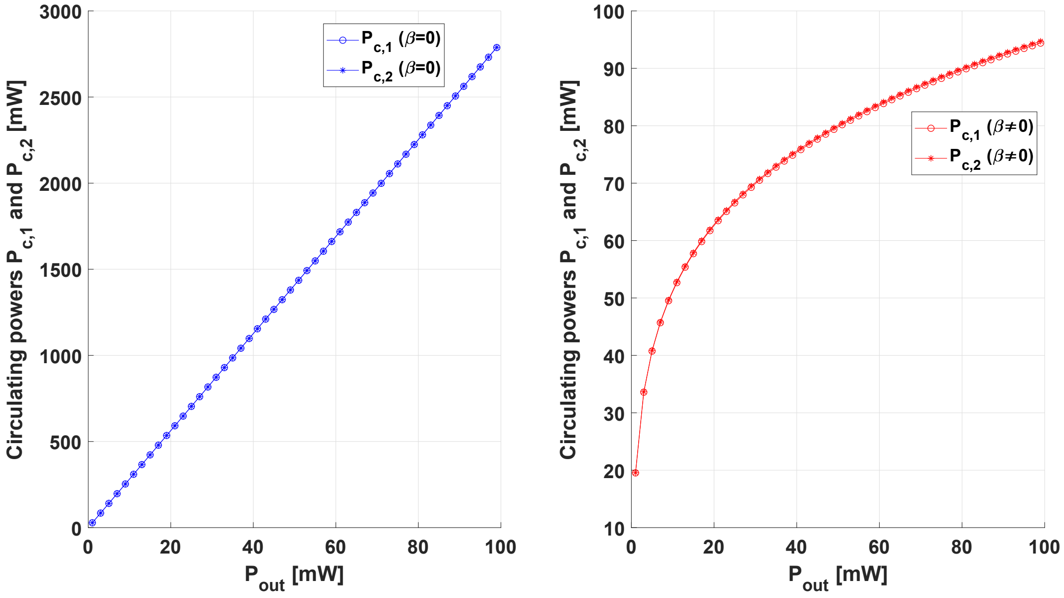

Figure 4.30: Circulating powers inside the two rings in both linear (left) and nonlinear (right) case when $\kappa_1 = \kappa_2 = 0.01$ and $T_{c,out} = 0.75$.

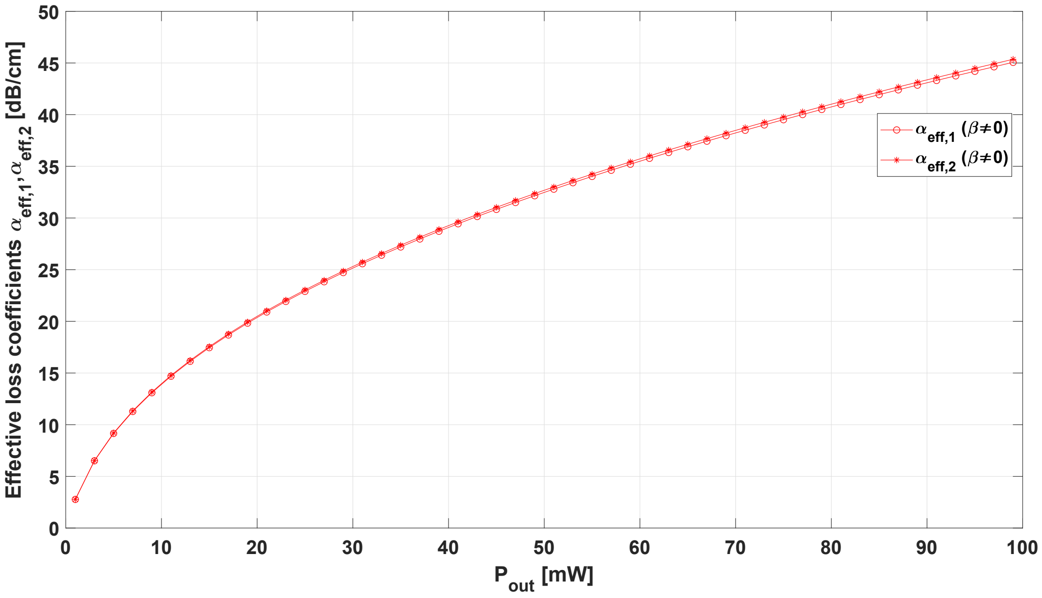

Figure 4.31: Effective loss coefficients of the two rings in the nonlinear case when $\kappa_1 = \kappa_2 = 0.01$ and $T_{c,out} = 0.75$.

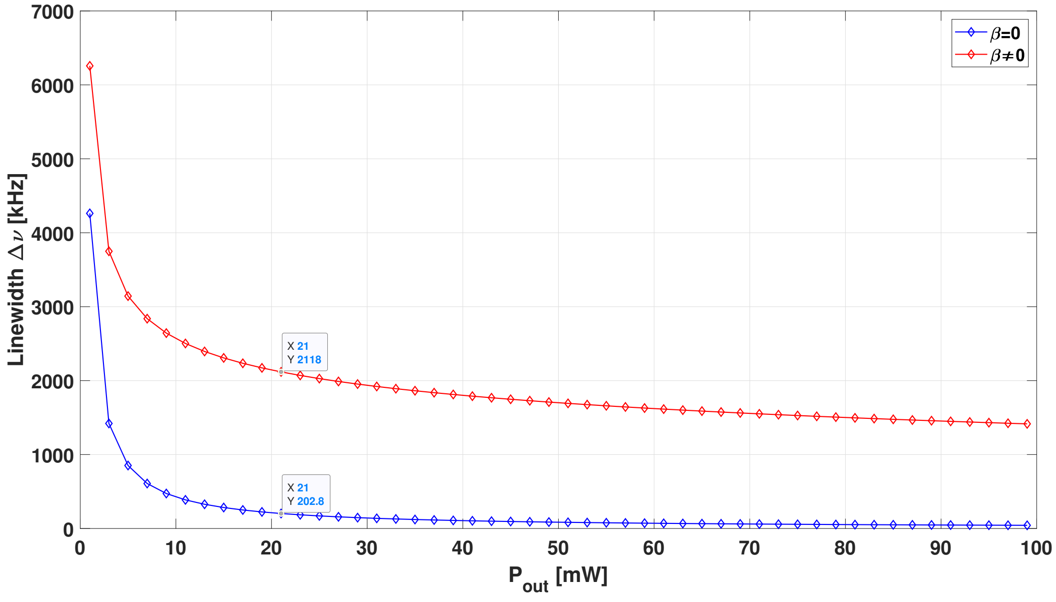

Figure 4.32: Linewidth in both linear and nonlinear case when $\kappa_1 = \kappa_2 = 0.01$ and $T_{c,out} = 0.75$.

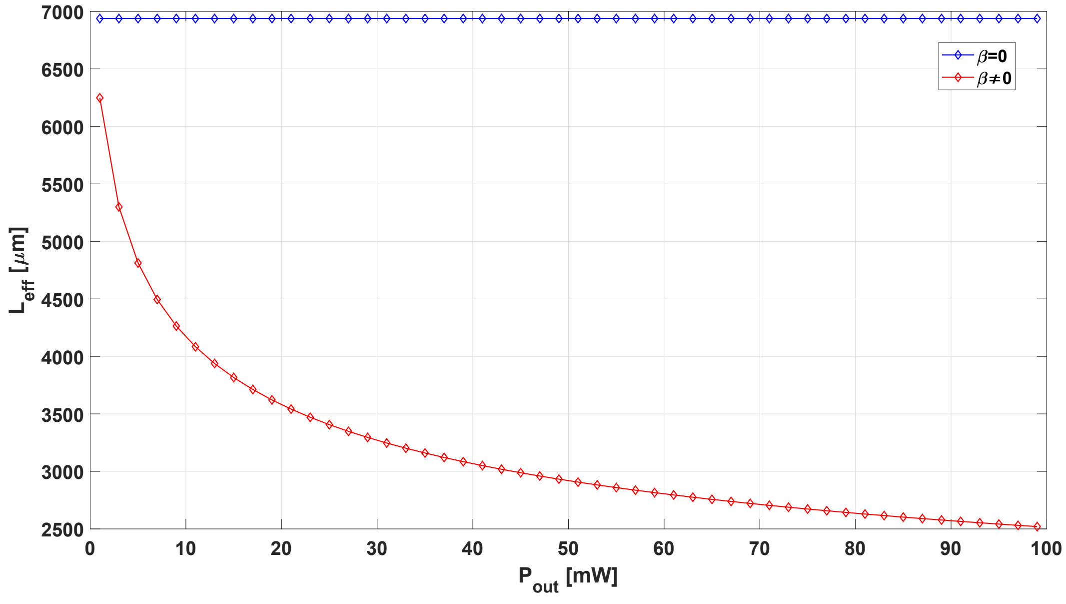

Figure 4.33: Effective length in both linear and nonlinear case when $\kappa_1 = \kappa_2 = 0.01$ and $T_{c,out} = 0.75$.

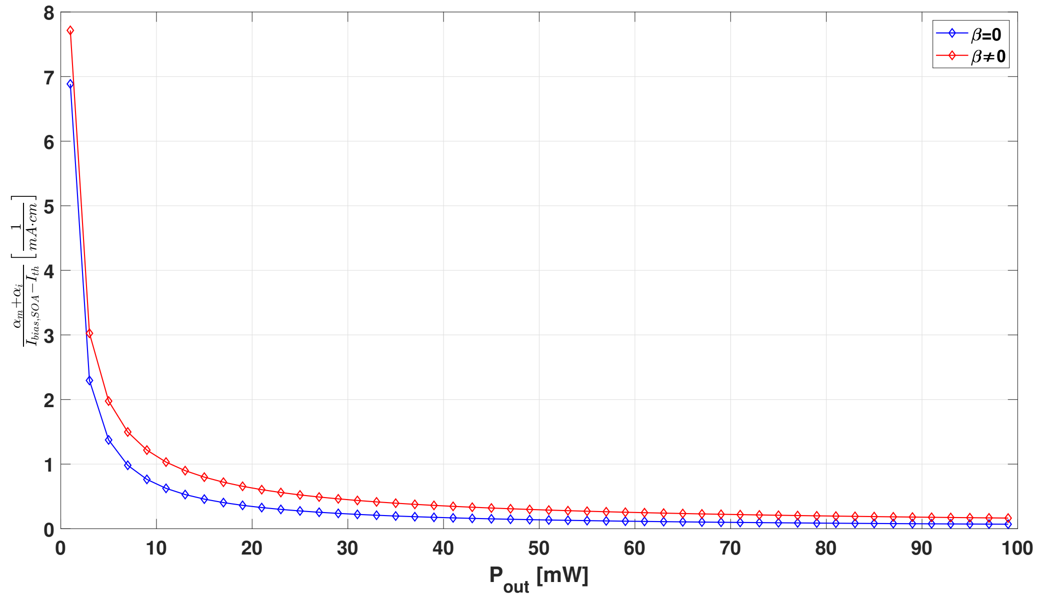

Figure 4.34: Behavior of the parameter used to justify the results in Figure 4.32.

Chapter 5

Results of the nonlinear model

This chapter presents the results related to the designs that 1) maximize the wall-plug-efficiency WPE and 2) minimize the linewidth $\Delta\nu$, for the hybrid laser architecture *Laser 2*, both in the linear and nonlinear case. The results that will be presented in the following have been obtained using two different SOA, SOA 1 and SOA 2, whose modal gains are shown in Figure 5.1. As can be seen, SOA 1 performs better than SOA 2 because the sharp increase in modal gain occurs at a lower current density, with a steeper slope; this means that lasers realized with this material will have a lower threshold current than that of lasers realized with SOA 2. The aim here is to understand the impact of nonlinear effects on the main figures of merits of the laser. In particular, Section 5.1 contains the results related to the design for the WPE maximization while Section 5.2 presents the results related to the design for the $\Delta\nu$ minimization. The following results have been obtained using Si mirror parameters listed in Table 5.1 when $P_{out,target} = 20mW$, $\beta = 6.7 \cdot 10^{-12} m/W$ and $\sigma = 1.97 \cdot 10^{-21} m^2$. Remember that the design parameters for *Laser 2* are $\kappa_1 = \kappa_2$ and $T_{c,out}$.

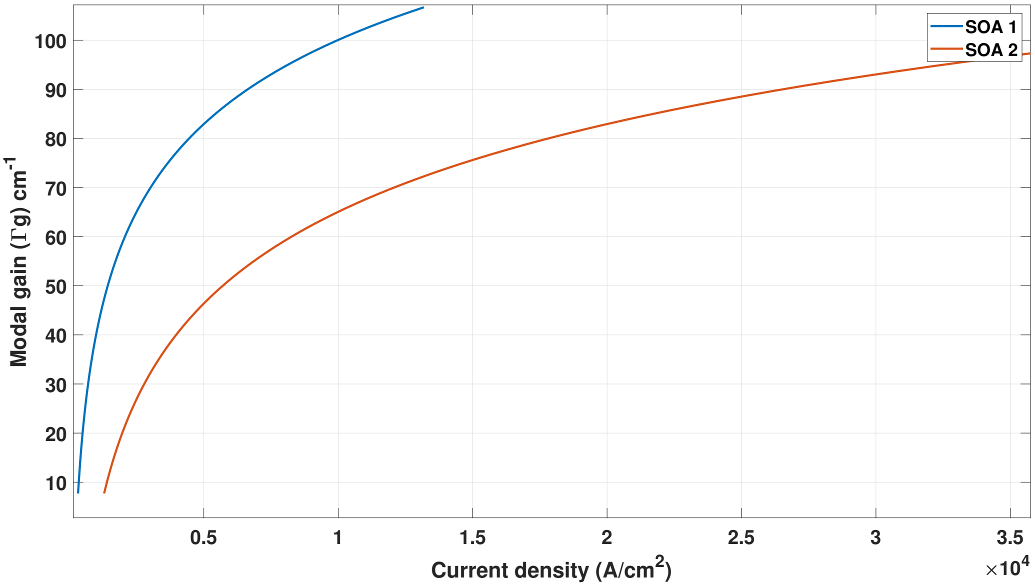

Figure 5.1: Modal gains of SOA1 and SOA2 as a function of the current density.

Table 5.1: Si mirror parameters

Si mirror parameters	
SSC insertion loss	$2dB$
Waveguide group refractive index	$n_{Si} = 3.786$
Waveguide loss	$(0 - 1.15)\ cm^{-1}$
Bent waveguide loss	$(0 - 2.30)\ cm^{-1}$
Ring radii	$R_1 = 12\mu m, R_2 = 10\mu m$

5.1 Results for WPE maximization

Figure 5.2 shows the behavior of the wall-plug-efficiency obtained using SOA 2, as a function of linear losses, both in the linear and nonlinear case. As one can easily see, the values of WPE, obtained in the nonlinear case, are slightly lower than those obtained in the linear case, in the entire range of linear losses tested in this work. Figure 5.3 shows instead the corresponding behavior of the linewidth, as a function

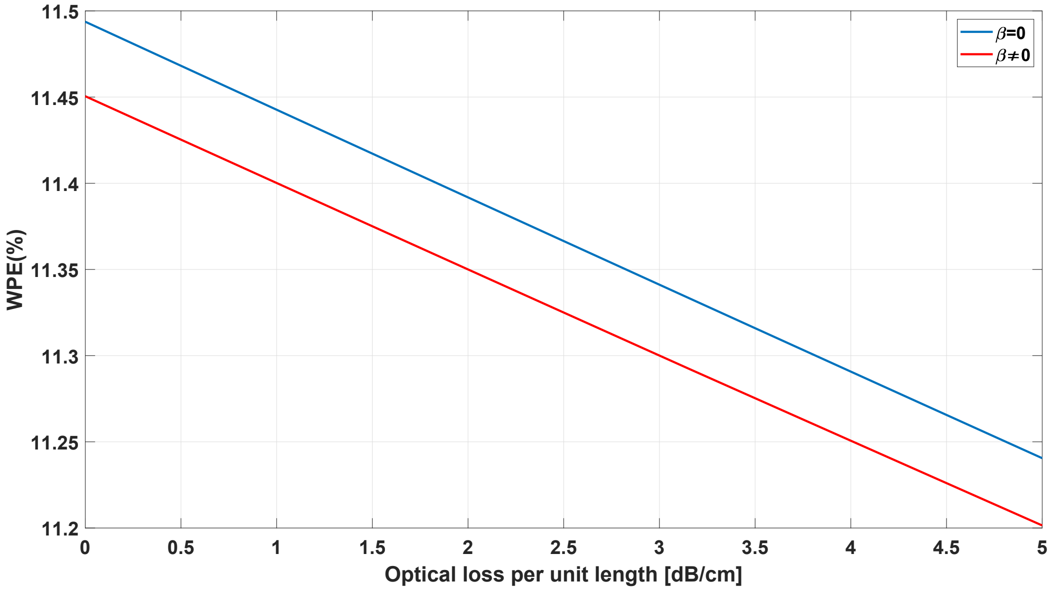

Figure 5.2: Calculated values of WPE, obtained using SOA 2, for the design that maximizes the WPE, both in the linear and nonlinear case.

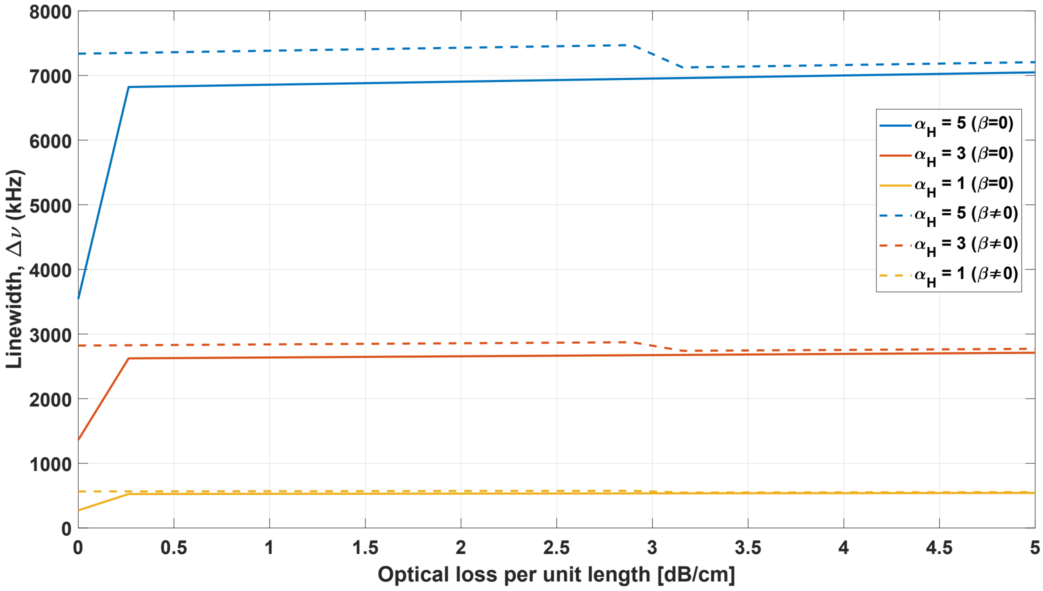

Figure 5.3: Calculated values of $\Delta\nu$, obtained using SOA 2, for the design that maximizes the WPE, both in the linear and nonlinear case.

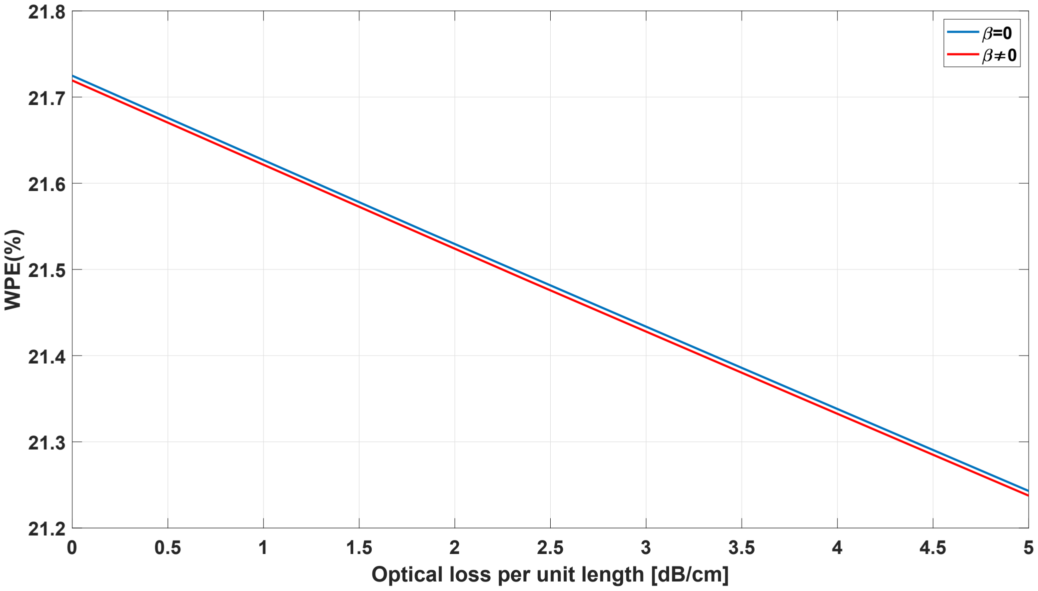

Figure 5.4: Calculated values of WPE, obtained using SOA 1, for the design that maximizes the WPE, both in the linear and nonlinear case.

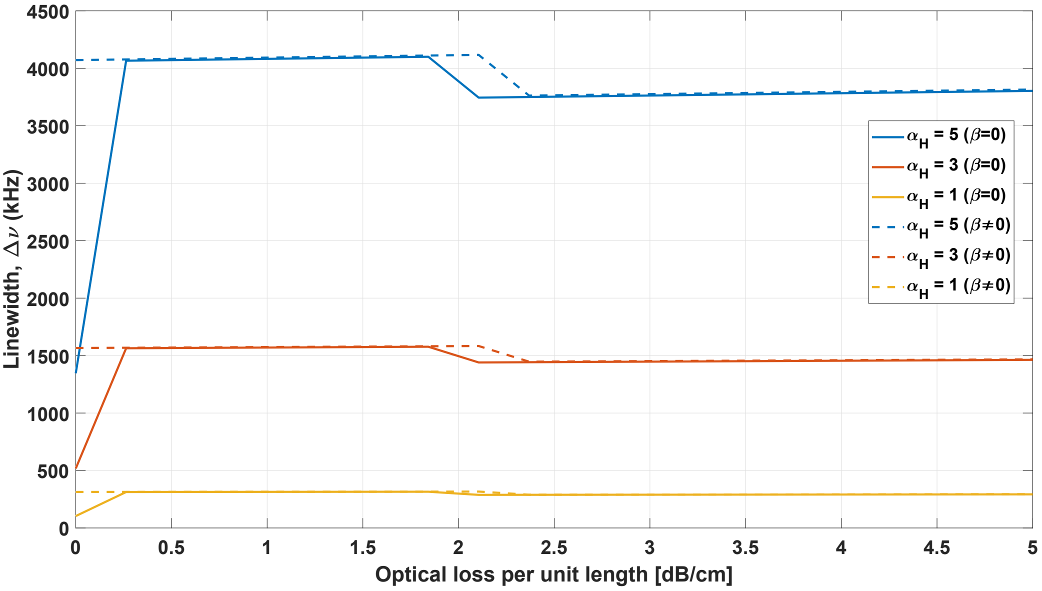

Figure 5.5: Calculated values of $\Delta\nu$, obtained using SOA 1, for the design that maximizes the WPE, both in the linear and nonlinear case.

of linear losses, for different values of the linewidth enhancement factor α_H. As can be noticed, the values of linewidth obtained in the nonlinear case are slightly higher than those obtained in the linear case, over the entire range of linear losses and for each value of α_H. Notice that the values of the design parameters in the linear case are $\kappa_1 = \kappa_2 \approx 0.183$ and $T_{c,out} = 0.79$ while for the nonlinear case we have $\kappa_1 = \kappa_2 = 0.19$ and $T_{c,out} \approx 0.796$. These similar values justify the low impact of nonlinear effects in Figures 5.2 and 5.3.

Figure 5.4 shows the wall-plug-efficiency obtained using SOA 1. Here, the values of WPE are much higher than those depicted in Figure 5.2 and the values obtained in the linear case are quite similar to those obtained in the nonlinear case. The corresponding values of $\Delta\nu$ are shown in Figure 5.5. Also here, the values obtained in the linear case are quite comparable to those obtained in the nonlinear case. Furthermore, the values of linewidth are lower than those presented in Figure 5.3. The values of the design parameters in the linear case are $\kappa_1 = \kappa_2 \approx 0.182$ and $T_{c,out} = 0.914$ while for the nonlinear case we have $\kappa_1 = \kappa_2 = 0.19$ and $T_{c,out} \approx 0.914$. Ultimately, one can conclude that, at least for this type of design, the impact of nonlinearities on the performances of the hybrid laser is not so important, irrespective of the type of SOA considered, simply because the amount of optical power sent to the MZI is quite low due to the high values of $T_{c,out}$.

5.2 Results for $\Delta\nu$ minimization

Figure 5.6 shows the behavior of the linewidth $\Delta\nu$ obtained using SOA 2, as a function of linear losses, for different values of α_H, both in the linear (top) and nonlinear (bottom) case. The impact of nonlinear effects is evident: the values of $\Delta\nu$ obtained in the nonlinear case are much higher than those obtained in the linear case. This is due to the fact that, since this design aims at minimizing the linewidth, the power inside the laser cavity is quite high, simply because we want

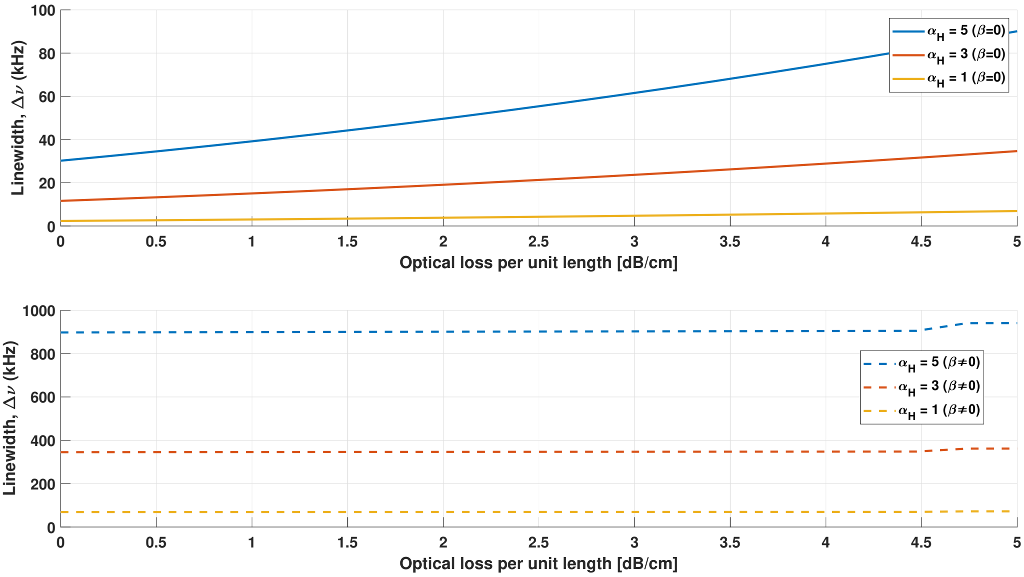

Figure 5.6: Calculated values of $\Delta\nu$, obtained using SOA 2, for the design that minimizes the linewidth, both in the linear (top) and nonlinear (bottom) case.

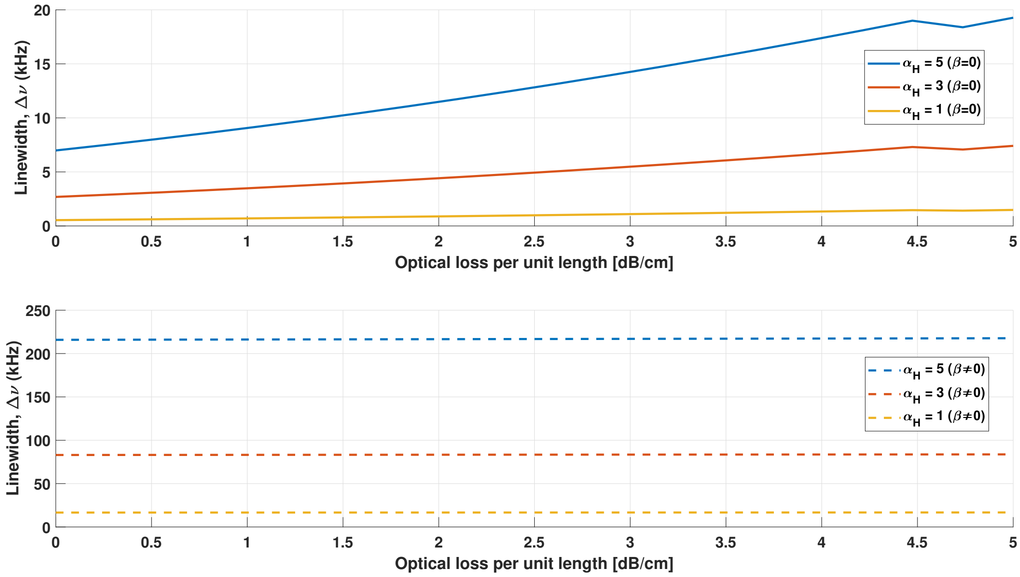

Figure 5.7: Calculated values of $\Delta\nu$, obtained using SOA 1, for the design that minimizes the linewidth, both in the linear (top) and nonlinear (bottom) case.

to increase the effective length. But if the power is high, nonlinearities are not negligible and they reduce the effective length, thus increasing the corresponding values of $\Delta\nu$. Unfortunately, the corresponding values of WPE have been found to be around 3%, in both the linear and nonlinear case. Notice that the values of the design parameters in the linear case are $\kappa_1 = \kappa_2 \approx 0.01$ and $T_{c,out} = 0.16$ while for the nonlinear case we have $\kappa_1 = \kappa_2 \approx 0.19$ and $T_{c,out} \approx 0.16$.

Figure 5.7 shows the values of $\Delta\nu$ obtained using SOA 1. Also here, the values obtained in the nonlinear case are much higher than those obtained in the linear case, for the same reason as before. Furthermore, these values of linewidth are lower than those depicted in Figure 5.6, but the corresponding values of WPE are always around 3%, in both the linear and nonlinear case. The values of the design parameters in the linear case are $\kappa_1 = \kappa_2 = 0.01$ and $T_{c,out} \approx 0.15$ while for the nonlinear case we have $\kappa_1 = \kappa_2 = 0.19$ and $T_{c,out} = 0.14$.

5.3 Conclusions

In consideration of the above, one can conclude that the impact of nonlinear effects on the performances of the laser is much more evident for the design that minimizes the linewidht $\Delta\nu$.

Chapter 6

Conclusions

The first part of this thesis presents two architectures of an hybrid laser, *Laser 1* and *Laser 2*, both implemented on a SiN platform. The performances of these devices have been investigated using two approaches. The first approach involves maximizing the wall-plug-efficiency WPE while the second approach aims at minimizing the optical linewidth $\Delta\nu$. Simulations results show two diametrically opposed situations. The values of WPE, obtained using the first approach, are quite high but the corresponding linewidths $\Delta\nu$ are not narrow. Narrower linewidths can be obtained using the second approach but the corresponding values of WPE are dramatically low (around 3%). Irrespective of the approach used, *Laser 2* performs better than *Laser 1*.

The second part of this work deals with the study of *Laser 2*, implemented on a silicon platform. In particular, the aim is the inclusion of nonlinear effects (TPA and FCA) that occur in silicon waveguides, especially for high power densities. Nonlinear models have been developed to include nonlinearities in ring resonators and in straight waveguides. Once these models are constructed, they are put together in such a way that it is possible to compute the value of the optical electric field effective reflectivity of the external mirror at the SOA AR facet. Once $r_{eff\_SOA}(\omega)$ is known, the performances of the device have been investigated using the two approaches presented above for two different types of SOA. Simulations results show

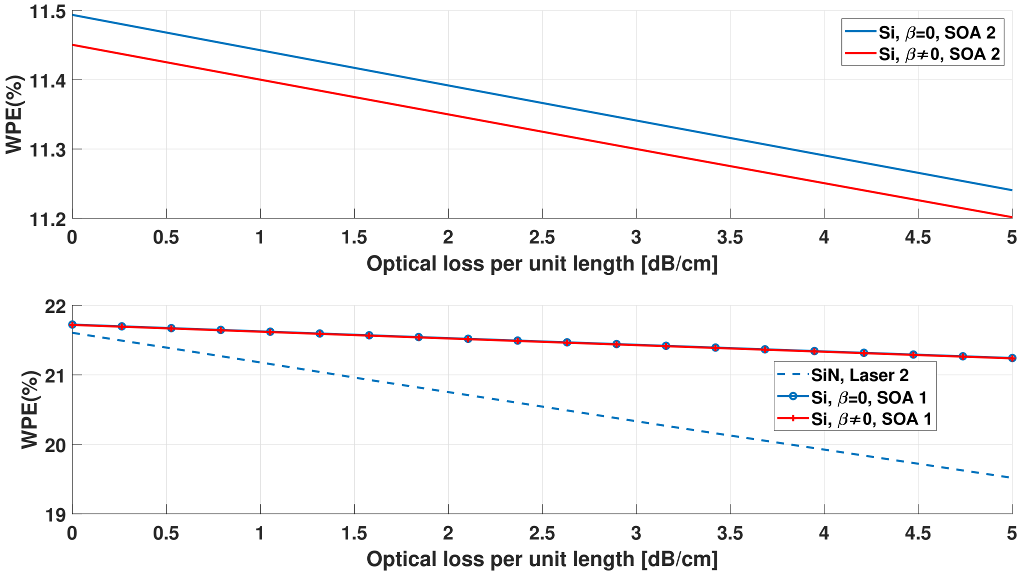

Figure 6.1: Top: values of WPE obtained using Si based lasers implemented with SOA 2; bottom: values of WPE obtained using 1) Si based lasers implemented with SOA 1 and 2) using SiN based lasers.

that the impact of nonlinear effects on the performances of the laser is much more evident for the design that minimizes the linewidth $\Delta\nu$.

Finally, a performance comparison between the lasers implemented on both platforms, is presented below. In particular, Figures 6.1-6.3 are related to the design that maximizes the WPE. As one can easily see from Figure 6.1, *Laser 2* implemented using SOA 1 on a Si platform, performs better in terms of WPE. This is due to the fact that the radii of the SiN rings are much higher than those of Si rings and, as a consequence of that, the impact of linear losses is high. Furthermore, Figures 6.2 and 6.3 show the corresponding values of linewidth obtained using SiN and Si with SOA 1 and SOA 2 when $\beta = 0$ and SiN and Si with SOA 1 and SOA 2 when $\beta \neq 0$, respectively. As can be seen, SiN based lasers provide narrower linewidths for low and intermediate values of linear losses while silicon based lasers, implemented using SOA 1, perform better for high values of linear losses. This is due to the fact that,

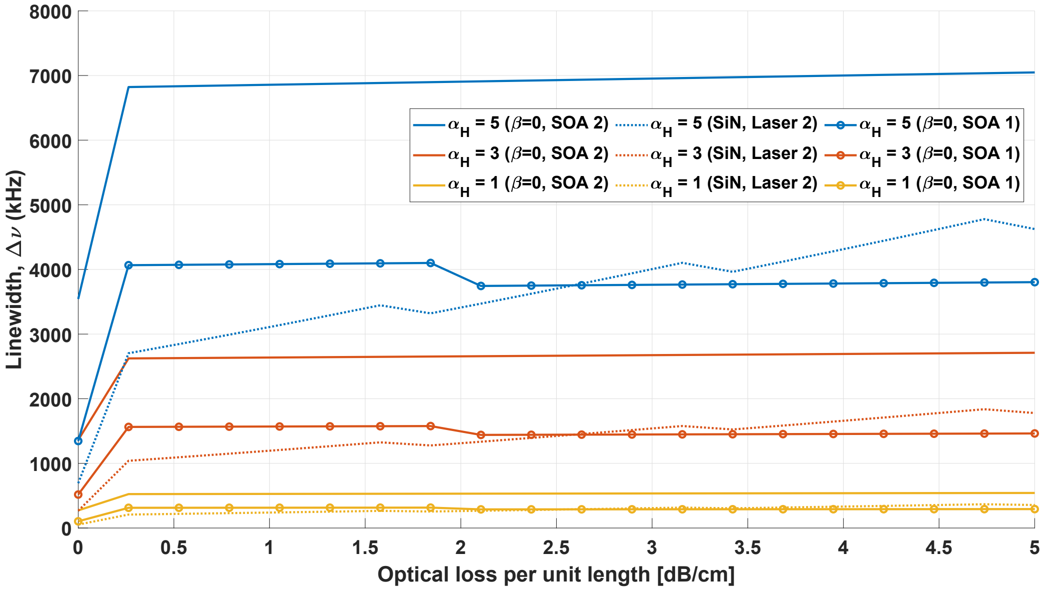

Figure 6.2: Comparison between the values of linewidth obtained using SiN and Si (SOA1 and SOA2 when $\beta = 0$), for the design that maximizes the WPE.

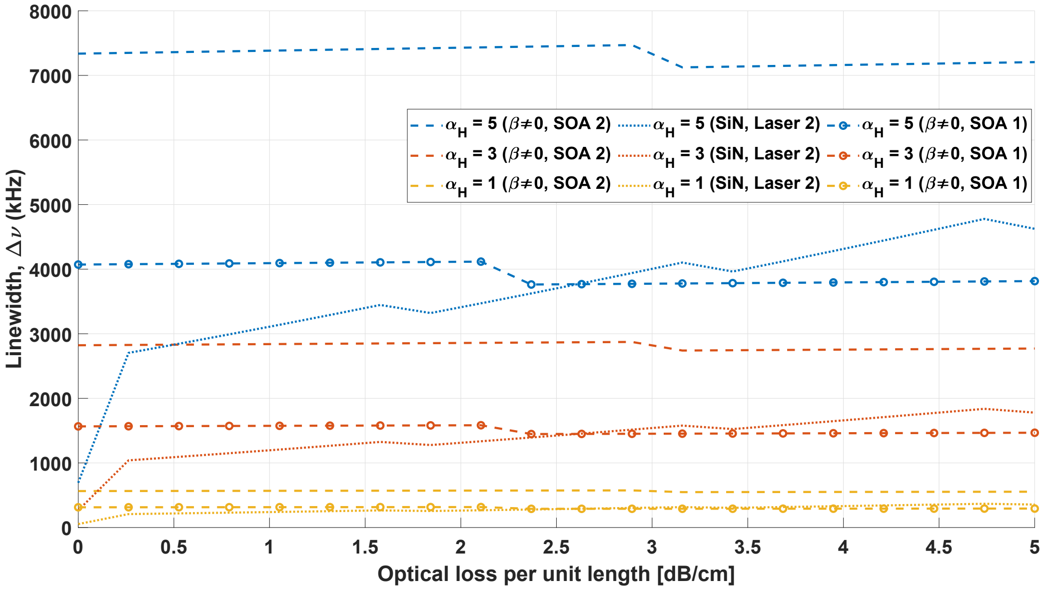

Figure 6.3: Comparison between the values of linewidth obtained using SiN and Si (SOA1 and SOA2 when $\beta \neq 0$), for the design that maximizes the WPE.

at least for low and intermediate values of linear losses, the value of the effective length that can be obtained using SiN rings is higher than that of Si rings, simply because the impact of linear losses is negligible. But when linear losses increase, the effective length of SiN rings is drastically reduced due to the high values of their radii, thus causing the increase of the corresponding values of $\Delta\nu$.

Figure 6.4 is instead related to the design that minimizes $\Delta\nu$. As can be observed, for very low values of linear losses, the values of linewidth obtained using SiN are the lowest but, as linear losses increase, Si based devices implemented using SOA 1 perform better, for the same reason explained before for Figures 6.2 and 6.3. The values of $\Delta\nu$ for Si based devices using SOA 1 are lower than those of Si based devices using SOA 2 because the threshold current is lower. Figure 6.5 shows that the values of linewidth obtained using Si based lasers with SOA 1, when $\beta \neq 0$, are higher than those obtained using SiN based devices because in this type of design the impact of nonlinear effects is much more evident. It is worth noticing that the corresponding values of WPE are dramatically low for both platforms (around 3%).

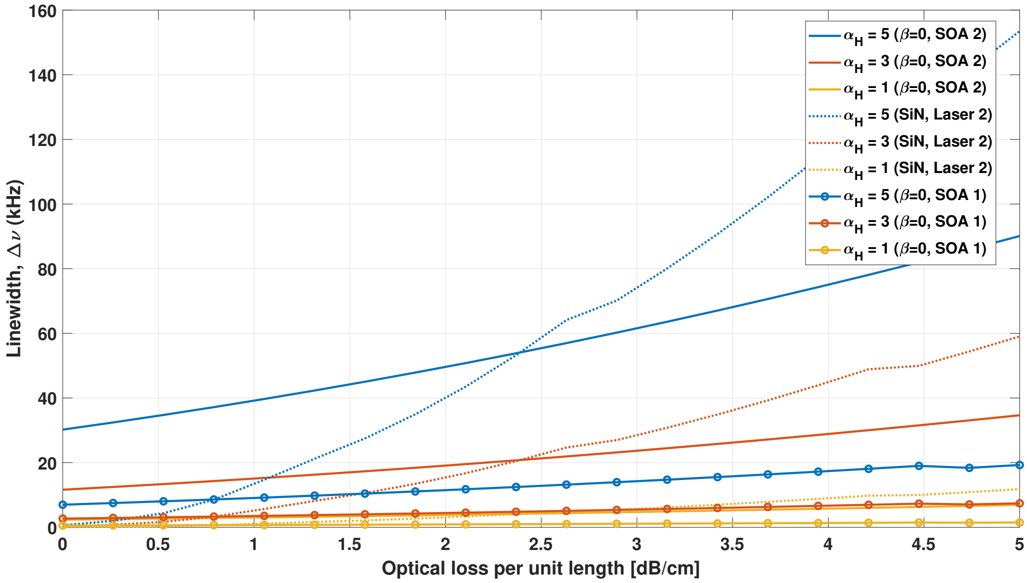

Figure 6.4: Comparison between the values of linewidth obtained using SiN and Si, for the design that minimizes the linewidth. The values of $\Delta\nu$ obtained using Si, in the nonlinear case, are not reported since they are much higher than those shown in this figure.

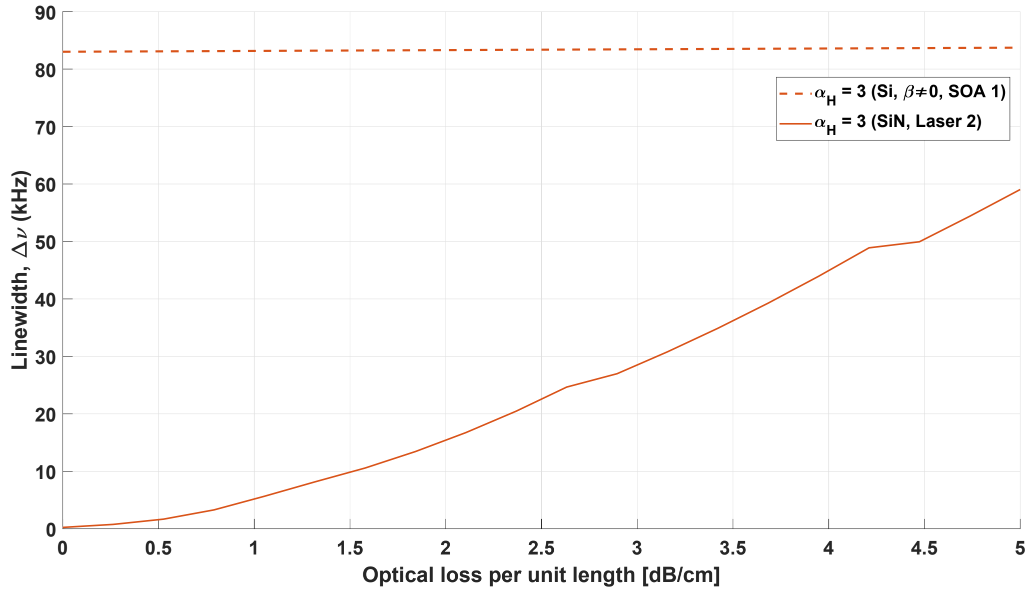

Figure 6.5: Comparison between the values of linewidth obtained using SiN and Si (SOA 1, $\beta \neq 0$), for the design that minimizes the linewidth.

Bibliography

[1] N. Magen, A. Kolodny, U. Weiser, and N. Shamir, “Interconnect-power dissipation in a microprocessor,” in Proceedings of the International Workshop on System Level Interconnect Prediction (SLIP ’04), pp. 7–13, Paris, France, February 2004.

[2] R. Soref and B. Bennett, “Electro-optical effects in silicon,” IEEE Journal of Quantum Electronics, vol.23, no.1, pp. 123–129, January 1987.

[3] V. Stojanović, R.J. Ram, M. Popović, S. Lin, S. Moazeni, M. Wade, C. Sun, L. Alloatti, A. Atabaki, F. Pavanello, N. Metha and P. Bhargava, "Monolithic silicon-photonic platforms in state-of-the-art CMOS SOI processes", Opt. Express, vol. 26, pp. 13106-13121, May 2018.

[4] D. Liang and J. E. Bowers, “Recent progress in lasers on silicon,” Nat. Photonics, vol. 4, no. 8, pp. 511–517, August. 2010.

[5] T. Komljenovic, M. Davenport, J. Hulme, A. Y. Liu, C. T. Santis, A. Spott, S. Srinivasan, E. J. Stanton, C. Zhang, and J. E. Bowers, “Heterogeneous silicon photonic integrated circuits,” J. Lightwave Technol., vol. 34, no. 1, pp. 20–35, January 2016. [Online]. Available: http://jlt.osa.org/abstract.cfm?URI=jlt-34-1-20

[6] Z. Zhou, B. Yin and J. Michel, "On-chip light sources for silicon photonics", Light: Science & Applications, vol. 4, e358, November 2015. [Online]

[7] G. Roelkens, L. Liu, J. Brouckaert, J. Van Campenhout, F. Van Laere, D. Van Thourhout and R. Baets, "Wafer Bonding and Heterogeneous Integration: III-V/Silicon Photonics", Proc. 14th ECIO 2008, pp.87-90.

[8] D. Liang, A. W. Fang, H. Park, T. E. Reynolds, K. Warner, D. C. Oakley, and

J. E. Bowers, “Low-Temperature, Strong SiO 2-SiO 2 Covalent Wafer Bonding for III–V Compound Semiconductors-to-Silicon Photonic Integrated Circuits,” J. Electron. Mater., vol.37, no.10, pp. 1552–1559, January 2008.

[9] S. Keyvaninia, M. Muneeb, S. Stanković, P. J. Van Veldhoven, D. Van Thourhout, and G. Roelkens, “Ultra-thin DVS-BCB adhesive bonding of III-V wafers, dies and multiple dies to a patterned silicon-on-insulator substrate,” Opt. Mater. Express, vol.3, no.1, pp.35–46, January 2013.

[10] P.Rojo-Romeo,J.VanCampenhout,F.Mandorlo,C.Seassal,X.Letratre, P. Regreny, D. Van Thourhout, R. Baets, L. Di Cioccio, and J. Fedeli, “Integration of an electrically driven InGaAsP based microdisk laser with a silicon based passive photonic circuit,” presented at the Lasers and Electro-Optics Conf., Baltimore, MD, USA, 2007, Paper CWN1.

[11] J. Van Campenhout, P. Rojo-Romeo, P. Regreny, C. Seassal, D. Van Thourhout, S. Verstuyft, L. Di Cioccio, J.-M. Fedeli, C. Lagahe, R. Baets, "Electrically pumped InP-based microdisk lasers integrated with a nanophotonic silicon-on-insulator waveguide circuit", Opt. Expr., vol. 15, no. 11, pp. 6744-6749, May 2007.

[12] S. R. Jain, Y. Tang, H.-W. Chen, M. N. Sysak, J. E. Bowers, "Integrated hybrid silicon transmitter", J. Lightw. Technol., vol. 30, no. 1, pp. 1-8, January 2012.

[13] M. Lamponi, S. Keyvaninia, C. Jany, F. Poingt, F. Lelarge, G. de Valicourt, G. Roelkens, D. Van Thourhout, S. Messaoudene, J.-M. Fedeli and G.H. Duan,"Low-threshold heterogeneously integrated InP/SOI laser with a double adiabatic taper coupler" ,IEEE Photonics Technol. Lett., vol. 24, no. 1, pp. 76–78, January 2012.

[14] B. Song, P. Contu, C. Stagarescu, S. Pinna, P. Abolghasem, S. Ristic, N. Bickel, J. Bowker, A. Behfar, and J. Klamkin, "3D integrated hybrid silicon laser," in 2015 European Conference on Optical Communication (ECOC) (IEEE, 2015), Vol. 2015–Novem, pp. 1–3.

[15] Y. Fan, J. P. Epping, R. M. Oldenbeuving, C. G. H. Roeloffzen, M. Hoekman, R. Dekker, R. G. Heideman, P. J. M. Van der Slot and K.-J. Boller, " Optically integrated InP-Si 3 N 4 hybrid laser ", IEEE Photon. J., vol. 8, no. 6, December

2016.

[16] H. Guan, A. Novack, T. Galfsky, Y. Ma, S. Fatholo						loumi, A. Horth, T. N. Huynh, J. Roman, R. Shi, M. Caverley, Y. Liu, T. Baehr-Jones, K. Bergman, and M. Hochberg, “Widely-tunable, narrow-linewidth iiiv/ silicon hybrid external-cavity laser for coherent communication,” Opt. Express, vol. 26, no. 7, pp. 7920–7933, April 2018.

[17] J.-H. Lee, I. Shubin, J. Yao, J. Bickford, Y. Luo, S. Lin, S. S. Djordjevic, H. D. Thacker, J. E. Cunningham, K. Raj, X. Zheng, and A. V. Krishnamoorthy, “High power and widely tunable Si hybrid external-cavity laser for power efficient Si photonics WDM links,” Opt. Express, vol. 22, no. 7, pp. 7678–7685, April 2014.

[18] N. Kobayashi, K. Sato, M. Namiwaka, K. Yamamoto, S. Watanabe, T. Kita, H. Yamada, and H. Yamazaki, “Silicon photonic hybrid ringfilter external cavity wavelength tunable lasers,” Journal of Lightwave Technology, vol. 33, no. 6, pp. 1241–1246, March 2015.

[19] J. Liu, X. Sun, D. Pan, X. Wang, L. C. Kimerling, T. L. Koch, and J. Michel, “Tensile-strained, n-type Ge as a gain medium for monolithic laser integration on Si,” Opt. Express, vol. 15, no. 18, pp. 11272–11277, September 2007.

[20] G. He and H. Atwater, "Interband transition in Sn_xGe_{1-x} alloys," Phys. Rev. Lett., vol. 79, no. 10, pp. 1937-1940, September 1997

[21] J. Michel, J. Liu, and L. C. Kimerling, "High performance Ge on Si photodetectors," Nature Photonics 4 , 527 534

[22] R. E. Camacho-Aguilera, Y. Cai, N. Patel, J. T. Bessette, M. Romagnoli, L. C. Kimerling and J. Michel, "An electrically pumped germanium laser," Opt. Express, vol. 20, no. 10, pp. 11316-11320, May 2012

[23] B. Dutt, D. S. Sukhdeo, D. Nam, B. M. Vulovic, Z. Yuan and K. C. Saraswat, "Roadmap to an Efficient Germanium-on-Silicon Laser: Strain vs. n-Type Doping," IEEE Photonics Journal, vol. 4, no. 5, October 2012.

[24] F. Olsson, M. Xie, S. Lourdudoss, I. Prieto and P. A. Postigo, "Epitaxial lateral overgrowth of InP on Si from nano-openings: theoretical and experimental

indication for defect filtering throughout the grown layer," Journal of Applied Physics, vol. 104, no.9, 093112-093112-6, December 2008

[25] A. Liu, C. Zhang, J. Norman, A. Snyder, D. Lubyshev, J. Fastenau, A. Liu, A. Gossard and J. Bowers, "High performance continuous wave 1.3 μm quantum dot lasers on silicon," Applied Physics Letters, vol. 104, no. 4, 041104-041104-4, January 2014

[26] T. Wang, H. Liu, A. Lee, F. Pozzi and A. Seeds, "1.3-mm InAs/GaAs quantum-dot lasers monolithically grown on Si substrates," Optics Express, vol. 19, no. 12, pp. 11381–11386, 2011

[27] P. Muñoz, G. Micó, L. A. Bru, D. Pastor, D. Pérez, J. D. Doménech, J. Fernández, R. Baños, B. Gargallo, R. Alemany, A. M. Sánchez, J. M. Cirera, R. Mas and C. Domínguez, "Silicon nitride photonic integration platforms for visible near-infrared and mid-infrared applications", Sensors, vol. 17, no. 9, pp. 1-25, 2017.

[28] W. Bogaerts, P. De Heyn, T. Van Vaerenbergh, K. De Vos, S. K. Selvaraja, T. Claes, P. Dumon, P. Bienstman, D. Van Thourhout and R. Baets, "Silicon microring resonators," Laser & Photonics Reviews 6, no. 1, pp. 47-73, 2012

[29] S. K. Selvaraja, P. De Heyn, G. Winroth, P. Ong, G. Lepage, C. Cailler, A. Rigny, K. K. Bourdelle, W. Bogaerts, D. VanThourhout, J. Van Campenhout and P. Absil, "Highly uniform and low-loss passive silicon photonics devices using a 300 mm CMOS platform," In Proceedings of the Optical Fiber Communication Conference, OSA, Washington, DC, USA, 9–13 March 2014

[30] B. Frey, D. Leviton, and T. Madison, “Temperature-dependent refractive index of silicon and germanium,” Proc. SPIE 6273, 62732J (2006).

[31] K. Wörhoff, R. G. Heideman, A. Leinse, and M. Hoekman, “Triplex: A versatile dielectric photonic platform,” Adv. Opt. Technol., vol. 4, no. 2, pp. 189–207, April 2015.

[32] A. W. Elshaari, I. E. Zadeh, K. D. Jöns and V. Zwiller, "Thermo-optic characterization of silicon nitride resonators for cryogenic photonic circuits," IEEE Photon. J., vol. 8, no. 3, 1–9 (2016).

[33] D. H. Geuzebroek, A. Driessen, "Ring-Resonator-Based Wavelength Filters" in Wavelength Filters for Fiber Optics (Springer Series in Optical Sciences 123), Germany, Berlin:Springer-Verlag, pp. 341-379, 2006, ch. 8.

[34] J. Heebner, R. Grover, and T. Ibrahim, Optical Microresonators: Theory, Fabrication and Applications, 1st edn., Springer Series in Optical Sciences (Springer, London, 2008).

[35] H. Jayatilleka, R. Boeck, K. Murray, J. Flueckiger, L. Chrostowski, N. A. F. Jaeger and S. Shekhar, "Automatic wavelength tuning of series-coupled Vernier racetrack resonators on SOI", Proc. Opt. Fiber Commun. Conf., 2016.

[36] T. Komljenovic, L. Liang, R. Chao, J. Hulme, S. Srinivasan, M. Davenport and J. E. Bowers, "Widely-tunable ring-resonator semiconductor lasers", Appl. Sci., vol. 7, no. 7, pp. 1-21, 2017.

[37] L. Columbo, J. Bovington, S. Romero-Garcia, D. Siriani and M. Gioannini, "Efficient and optical feedback tolerant hybrid laser design for silicon photonics applications," IEEE Journal of Selected Topics in Quantum Electronics, vol. 26, issue: 2, October 2019.

[38] S. C. L.A. Coldren, Semiconductor and Photonic Integrated Circuits. Wiley, 1995.

[39] D. Dimitropoulos, D. R. Solli, R. Claps and O. Boyraz, "Noise Figure of Silicon Raman Amplifiers," Journal of Lightwave Technology, vol. 26, no. 7, pp. 847-852, May 2008

[40] Y. Guo, W. Zhang, N. Lv, Q. Zhou, Y. Huang, and J. Peng, “The impact of nonlinear losses in the silicon micro-ring cavities on cw pumping correlated photon pair generation,” Opt. Express 22, 2620–2631 (2014).

[41] M. Soltani, Novel integrated silicon nanophotonic structures using ultra-high Q resonator, Ph.D. dissertation, Georgia Institute of Technology, 2009